YANNICK DENGLER, BSC. MSC.
Mat. No. 12210267

Non-Perturbative Signatures of Strongly-Interacting Dark Matter

PHD THESIS

Doctoral thesis to achieve the university degree of
Doctor of Natural Sciences (Dr.rer.nat.; equivalent to PhD)

University of Graz
Institute of Physics

Supervisor: Univ.-Prof. Dipl.-Phys. Dr.rer.nat. Axel MAAS
2nd Examiner: Prof. Dr. Saša PRELOVŠEK KOMELJ

Graz, October 2025

Abstract

The existence of dark matter is one of the gravest and most challenging enigmas in modern physics, which is otherwise well described by the Standard Model of particle physics. Despite strong evidence for this invisible matter, which accounts for five times more mass than all the particles of the Standard Model, we have not yet been able to observe it directly. This has led to the postulation of numerous theories that seek to describe its very nature. Often, these deal not only with the puzzle of dark matter, but also with other inconsistencies in the Standard Model. In light of the small-scale structure problems that pose a challenge to standard cosmology, scenarios involving self-interacting dark matter gained popularity. One particular dark matter model that concurrently explains how today's relic abundance emerged is strongly-interacting massive particles. This scenario is based on ultraviolet completions making use of non-Abelian gauge theories and therefore relies on the application of non-perturbative methods. To this end, we utilize lattice gauge theory, which offers the methodological mainstay for the determination of non-perturbative signatures. We consider two specific realizations of strongly-interacting massive particles in which fundamental quarks are charged under local gauge symmetries described by the groups G_2 and $Sp(4)$. In the first case, we investigate their influence on neutron stars and confirm that stable mixed stars can form with significantly different macroscopic parameters such as mass, radius, and tidal deformability. In the second case, we supplement the existing spectroscopy data with scattering calculations using the Lüscher formalism and obtain sound descriptions of resonance parameters and the cross section at low energies. This work provides necessary validation of these theories through non-perturbative calculations.

Kurzfassung

Die Existenz dunkler Materie ist eines der schwerwiegendsten und anspruchsvollsten Rätsel der modernen Physik, die ansonsten außerordentlich gut durch das Standardmodell der Teilchenphysik beschrieben wird. Trotz starker Hinweise auf diese unsichtbare Materie, die fünfmal mehr Masse ausmacht als alle Teilchen des Standardmodells, konnten wir sie bisher noch nicht direkt beobachten. Dies hat zur Postulierung zahlreicher Theorien geführt, die versuchen, ihre Natur zu beschreiben. Oft befassen sich diese nicht nur mit dem Rätsel der dunklen Materie, sondern auch mit anderen Unstimmigkeiten im Standardmodell. Angesichts der Probleme auf kleinen Skalen, die eine Herausforderung für die Standardkosmologie darstellen, gewannen Szenarien mit selbstwechselwirkender dunkler Materie an Popularität. Ein spezifisches Modell der dunklen Materie, das gleichzeitig erklärt, wie die heutige Reliktabundanz entstanden ist, sind stark wechselwirkende massive Teilchen. Dieses Szenario basiert auf ultravioletten Vervollständigungen unter Verwendung nicht-abelscher Eichtheorien und stützt sich daher auf die Verwendung nicht-perturbativer Methoden. Daher verwenden wir Gitter-Eichtheorie, die den methodischen Grundpfeiler für die Bestimmung nicht-perturbativer Signaturen bietet. Wir betrachten zwei spezifische Realisierungen stark wechselwirkender massiver Teilchen, in denen fundamentale Quarks unter lokalen Eichsymmetrien geladen sind, die durch die Gruppen G_2 und $Sp(4)$ beschrieben werden. Im ersten Fall untersuchen wir ihren den Einfluss auf Neutronensterne und stellen fest, dass auch diese Art von dunkler Materie in stabilen gemischten Sternen untergebracht werden kann und einen erheblichen Einfluss auf makroskopische Parameter wie Masse, Radius und Gezeitenverformbarkeit haben kann. Im zweiten Fall ergänzen wir die bestehenden Spektroskopiedaten durch Streuungsberechnungen unter Verwendung des Lüscher-Formalismus und erhalten fundierte Beschreibungen der Reonanzparameter und des Wirkungsquerschnitt bei niedrigen Energien. Diese Arbeit bietet die zwingend notwendige Validierung dieser Theorien durch nicht-perturbative Berechnungen.

First of all, I would like to thank my advisor Axel Maas for his excellent support and dedication and for always taking the time to discuss questions in great detail. I would further like to thank my second examiner, Saša Prelovšek, with whom I have already exchanged ideas during my doctoral studies.

I would like to thank all my collaborators over the past few years. First and foremost, Fabian Zierler, who very much helped me get started in lattice field theory and symplectic groups. I would like to thank Suchita Kulkarni for the great discussions on the phenomenology of dark matter. I would also like to express my gratitude for the opportunity to conduct research stays in Edinburgh, Ljubljana, and Swansea, especially with Maxwell Hansen, Athari Alotaibi, Luka Leskovec, Maurizio Piai, and Biagio Lucini.

A big thank you goes out to the friends I made in Mozartgasse. The three and a half years would not have been so memorable without you. Thank you, Eduardo Ferreira, Joshua Lockyer, Fabian Zierler, Elizabeth Dobson, Enno Carstensen, Georg Wieland, Seán Mee, Raúl D. Torres, Bernd Riederer, especially for providing this Latex template, Nicole Oberth, Felix Halbwedl, Joachim Pomper, Fabian Veider, Michael Mandl and Sofie Martins.

Zu guter Letzt möchte ich mich von ganzem Herzen bei meinen Freunden und meiner Familie für ihre stetige Unterstützung, ihre Ermutigung und ihren Glauben an mich bedanken. Ihr habt mich in jeder Phase dieser Arbeit begleitet und mich aufgefangen, wenn es schwierig wurde. Ohne euch wäre diese Arbeit in dieser Form nicht möglich gewesen.

This work was supported by the Austrian Science Fund research teams grant STRONG-DM (FG1). I acknowledge travel support from the City of Graz and the Doctoral School of Physics at the University of Graz. Many of the data presented in this thesis were obtained on supercomputers. Numerical simulations were performed on the Vienna Scientific Cluster (VSC4), Graz Scientific Cluster (GSC1) at the University of Graz, the DiRAC Data Intensive service (CSD3) at the University of Cambridge, the DiRAC Data Intensive service (DIaL3) at the University of Leicester, and the DiRAC Extreme Scaling service (Tursa) at the University of Edinburgh, managed respectively by the University of Cambridge University Information Services, the University of Leicester Research Computing Service and by EPCC on behalf of the STFC DiRAC HPC Facility (www.dirac.ac.uk) and on the Swansea SUNBIRD cluster (part of the Supercomputing Wales project). The Swansea SUNBIRD system is part funded by the European Regional Development Fund (ERDF) via Welsh Government. During the writing process, I used AI-based tools, including OpenAIs ChatGPT and DeepL Translator, to assist with phrasing, translation between English and German, and code syntax suggestions. All ideas, interpretations, and final formulations are my own.

Contents

Chapter 1

Introduction

For centuries, humanity has been asking the question that particle physicists attempt to answer every day. What are the most fundamental building blocks of the universe? Throughout history, our understanding of what those are has changed several times, from atoms to protons and neutrons, all the way to quarks and leptons. Modern particle physics describes the world in elementary particles that are considered to be point-like and indivisible. They form the Standard Model of particle physics, which describes all known matter and its interactions. It contains twelve fermions arranged into three families, each consisting of two quarks, a lepton, and a neutrino. Their different charges determine how they interact with exchange bosons that mediate the fundamental forces. There are photons that mediate electromagnetism, the W- and Z-bosons that mediate the weak nuclear force, and the gluons that mediate the strong nuclear force. In addition, there is the Higgs boson, which provides mass to the other particles of the Standard Model via the Brout-Englert-Higgs effect.

The Standard Model is tremendously successful in the description of the world on the smallest scales, but it is not a complete theory of nature. Crucially, the standard model does not accommodate the fourth known force, gravity, which is best described by general relativity. This and other inconsistencies are commonly summarized by the term *beyond the Standard Model* (BSM) physics. Perchance, the greatest of these is the existence of dark matter.

1.1 Dark Matter

There are a series of observations that cannot be explained within the framework of the Standard Model and point to an unknown type of matter. This is summarized in the term *dark matter* first coined by Fritz Zwicky in 1935 [1] to describe additional gravitationally acting non-illuminated mass. Throughout the twentieth century, evidence for dark matter solidified, the most prominent being *rotation curves* [2, 3]. If the mass distribution of an astronomical object is known, the laws of gravity determine the velocity at which satellites orbit these objects. Observation, however, shows that throughout the universe satellites orbit massive objects like galaxies much faster than expected. The enclosed mass in a gravitationally bound system can also be inferred from the virial theorem and evidence solidified on scales ranging from the smallest galaxies to galaxy clusters through improved measurements using, for example, stellar number counts, X-ray emission of hot interstellar gas and gravitational lensing [4, 5]. A straightforward explanation for these observations is the existence of additional matter that cannot be directly observed with telescopes. We will not present a full list of evidence and refer to reviews for details [4, 6–8]

In addition to this evidence, dark matter also plays an important role in the formation of the structures that we observe today [7] and of the *cosmic microwave background* (CMB) [9–11]. Modern cosmological models describe the evolution of the universe with three ingredients, the cosmological constant Λ (*dark energy*), collisionless *cold dark matter* (CDM) and the particles of the Standard Model. This is the ΛCDM model which is very successful in describing the evolution of the universe and dynamics on large scales corresponding to distances $> 1\,\mathrm{Mpc}$. Recent results of the *Dark Energy Spectroscopic Instrument* [12–14] using *baryon acoustic oscillation* measurements to investigate the expansion history and the large-scale structure of the universe are consistent with the ΛCDM model. However, the parameters for dark energy are in 2.3σ tension with those determined from the CMB [9, 11]. This tension is alleviated by allowing for a dynamical time-evolving equation of state for dark energy, but nevertheless it presents a challenge for the ΛCDM model.

An alternative to the particle dark matter picture is a modification of the laws of gravity like $f(R)$ *gravity* or *modified Newtonian dynamics* [15, 16]. The particle nature of dark matter was strongly reinforced by the observation of the *Bullet Cluster*, a colliding galaxy cluster system [17]. The distribution of illuminated matter was inferred from X-ray observation, and the gravitational acting matter was inferred using gravitational lensing. It was found that most gravitational mass traversed the cluster more or less unhindered, whereas the illuminated mass formed a hot gas. This is difficult to explain by a modification of gravity, which underpins the dark matter hypothesis. Additionally, the observation of merging clusters provides constraints on the self-interaction of dark matter [17, 18]. The solution to the dark matter puzzle, however, might very well a combination of different approaches.

A dark matter particle must fulfill a set of properties. It has to be massive, stable [19], non-relativistic, and may interact only to a minor extent, if at all, with particles of the Standard Model [4]. These constraints are incompatible with any of the particles in the Standard Model, and as a result, dark matter models beyond the Standard Model were postulated the most famous being weakly interacting massive particles (WIMPs), axions, sterile neutrinos, and primordial black holes [20]. Many models not only address the dark matter problem but are connected to a wider range of BSM theories.

1.1.1 Observation Efforts

Despite the overwhelming evidence for its existence, the fundamental nature of dark matter remains unknown, necessitating a broad and complementary program of experimental searches across different detection strategies. While the mass of a dark matter particle can be constrained fairly well within a particular model, the model-independent bounds range from $10^{-22}\,\mathrm{eV}$ to 5 solar masses [4].[1]

The search for dark matter can be divided into different efforts. *Direct detection* experiments [8, 21–25] aim to observe elastic or inelastic scattering of galactic dark matter with atomic nuclei or electrons in some detector material. Depending on the detector material, the constraints on the cross section are strongest for a specific dark matter mass. This is on the one hand because the local density of dark matter is fixed, and assuming a heavy dark matter particle, the rate of dark matter particles hitting the experiment is lower. If dark matter, on the other hand, were light, the recoil on the detector material would be smaller, and the experiment might not be able to detect the event. For certain dark matter masses, direct detection experiments are able to constrain the dark matter-nucleon cross section to be lower than $10^{-47}\mathrm{cm}^2$ [4, 26–28].

Dark matter can also be searched for in particle accelerators [4, 29–33]. Events are scanned for large amounts of missing energy, which could indicate a potential dark matter particle escaping the detector unhindered. These searches are usually based on an interaction of the dark matter candidate with the Standard Model Higgs or Z-boson or mediators that are introduced in BSM theories. So far, no signal for dark matter has been observed in any collider experiment.

A third kind of effort is *indirect detections* which refers to the search for Stan-

---

[1] The solar mass is the mass of the sun denoted as $M_\odot$.

dard Model annihilation or decay products from astrophysical scattering of dark matter, especially gamma rays, neutrinos, and antimatter particles. While there are notable gamma-ray excesses, they usually have an astrophysical explanation consistent with the Standard Model [4, 34–36].

Lastly, we mention the endeavor of identifying dark matter through the observation of astronomical probes such as neutron stars. It is inevitable that dark matter accumulates in neutron stars or other compact objects to some extent. Conclusions can be drawn if the additional dark matter has a measurable influence on the macroscopic properties of the star that cannot be explained within the scope of the Standard Model. We investigate this possibility for one specific dark matter model in Chapter 2.

1.1.2 Self-Interacting Dark Matter

To date, all observations are still compatible with dark matter being completely non-interacting and the CDM hypothesis is very successful at describing large-scale structures. But in recent years the possibility of dark matter being self-interacting gained more attention [37]. A major reason for that are the so-called *small-scale structure problems* [38, 39].

Cusp vs. core problem: Simulations of collisionless CDM predict that the dark matter density distribution at low radii rises steeply, which is referred to as a *cuspy* shape. However, observation of rotation curves of these objects indicates a *cored* shape where the dark matter density is constant at small distances from the center. The consideration of baryonic feedback in galaxy formation can provide a solution to the cusp-vs-core problem [4]. Alternatively simulations of halo shapes including a self-interaction among dark matter particles also result in the observed halo shape.

Diversity problem: Given only collisionless dark matter, halos should be specified by a single parameter, as all other halo parameters are strongly correlated. Yet the parameters of the observed rotation curves, given by the peak circular velocity and the circular velocity at a set distance from the center, show a large diversity. This indicates the existence of additional parameters that specify the halo shape which could be introduced by self-interacting dark matter [40, 41].

Too big to fail problem: This problem describes the lack of stellar objects in massive galaxy subhalos with large central masses of roughly $10^{10}\ M_\odot$. The number of massive subhalos in CDM simulations matches the observed number but they fail to form stellar objects, and with that dwarf galaxies. On the other hand, classical dwarf galaxies exist in much smaller subhalos of the Milky Way.

This mismatch is called the too big too fail problem, as the massive subhalos in the Milky Way should be too big to fail in forming galaxies.

Missing satallites problem: Cosmological simulations of Milky Way-sized dark matter halos predict hundreds or thousands of subhalos with masses large enough for galaxy formation. Yet, less than about 100 satellite galaxies at masses down to about 300 $M_{\odot}$ have been found in the Milky Way and similar galaxies. One possibility is that galaxy formation becomes less efficient for low halo masses. With recent progress in both observation and theoretical modeling, there is very limited evidence for a missing satellite problem [4, 37, 40].

All of these problems are addressed by self-interacting dark matter [42]. The strongest limits for the self-interaction cross section are $\sigma/m < 0.13\,\mathrm{cm}^2/g$ [18, 43–45], albeit with potentially large systematic errors. Additionally, recent work on simulations of dark matter on small scales also granted access to the velocity-weighted cross section [46–48], which we will introduce in Section 3.1.3.

1.1.3 Relic Density

It is often assumed that dark matter was created in large quantities and was in thermal and chemical equilibrium with the Standard Model in the early hot and dense universe. This equilibrium is usually reached by a coupling via a mediator. But if dark matter is subject to any kind of interaction, it is possible and expected that its amount[2] has varied over the history of the universe. This is described by relic density mechanisms which are of major importance for dark matter physics. Certain relic-density mechanisms allow for much larger amounts of dark matter in the early universe that can, for example, be used to describe galaxy formation.

Later, in cosmological time, the universe has expanded and two factors came into play. Firstly, the density decreases and it becomes less likely for particles to interact. Secondly, as the temperature decreases as well, it becomes less likely that heavy particles are created from lighter ones. This is called freeze-out [49] and occurs when the interaction rate drops below the Hubble rate H which parameterizes the expansion of the universe. In most scenarios, it is assumed that nowadays dark matter is frozen out, which means that its abundance will remain at its current value, called the *relic abundance*. The point in time at which the relic abundance of dark matter is reached is known as the *freeze-out time*.

Mathematically, relic density mechanisms are described by the Boltzmann equations. The WIMP scenario is the most popular relic density mechanism. It

---

[2] More specifically the abundance of a certain species which is which is defined to be $Y = n/T^3$ where n is the number density and T is the temperature.

considers a depletion process involving two dark matter particles and two Standard Model particles. In this case, the Boltzmann equation reads

$$\frac{dn}{dt} + 3Hn = -\langle \sigma_{2DM \to 2SM}\, v \rangle (n^2 - n_{\text{eq}}^2), \tag{1.1}$$

where n is the number density of dark matter and n_{eq} is its value at equilibrium. $\langle \sigma_{2DM \to 2SM}\, v \rangle$ is the thermal average of the velocity-weighted depletion cross section. This model yields the relic abundance for TeV dark matter that interacts on the *weak scale*. In light of the increasing popularity of strongly-interacting dark matter, an alternative freeze-out mechanism was proposed making use of a number lowering *cannibalization* process in the dark sector. For example, for a three-to-two process, the Boltzmann equation is

$$\frac{dn}{dt} + 3Hn = -\langle \sigma_{3DM \to 2DM}\, v^2 \rangle (n^2 - n_{\text{eq}}^2), \tag{1.2}$$

This is called the *strongly interacting massive particle* (SIMP) mechanism [50–57], and it proposes dark matter masses below 1 GeV where experimental constraints are relatively loose. These models by construction inherit a sizeable two-to-two process which addresses the small-scale structure problems. In order to reach thermal equilibrium, a mediator to the Standard Model is included which would enable a direct detection in collider experiments. The strong interaction scale required in SIMP models makes strongly-interacting confining QCD[3]-like theories with asymptotic freedom and chiral symmetry breaking an attractive realization. This thesis aims to shed some light on dark matter by investigating its potential non-perturbative signatures.

1.2 Non-Abelian Gauge Theories and QCD

In this section, we will introduce the basics of non-Abelian gauge field theory, which is the underlying theory of the strong and electroweak sectors in the Standard Model. We will introduce the concepts on a more fundamental level in order to include more general theories that may describe BSM physics. The general Lagrangian of gauge field theories in Euclidean metric reads[4]

$$\mathcal{L} = \frac{1}{4}\text{tr}\left[F_{\mu\nu}(x)F_{\mu\nu}(x)\right] + \sum_f \bar{\psi}_f \left(\gamma_\mu D_\mu + m_f\right)\psi_f, \tag{1.3}$$

---

[3] *Quantum chromodynamics*

[4] An overview of the conventions used is provided in Appendix A.

where ψ_f is a set of quark fields with masses m_f, $\bar{\psi} = \psi^\dagger \gamma_4$ their adjoint quark fields, $D_\mu = \partial_\mu + ig\mathcal{A}_\mu(x)$ is the covariant derivative with the gluon coupling strength g and the gauge fields $\mathcal{A}_\mu(x)$, γ_μ are the gamma matrices and $F_{\mu\nu}(x)$ is the gluon field strength tensor.

$$F_{\mu\nu}(x) = \partial_\mu \mathcal{A}_\nu(x) - \partial_\nu \mathcal{A}_\mu(x) + ig[\mathcal{A}_\mu(x), \mathcal{A}_\nu(x)] \tag{1.4}$$

Color indices are suppressed. The gauge fields can be expressed as components of the adjoint generators $\mathcal{A}_\mu(x) = \mathcal{A}^c_\mu(x)T^c$. In non-Abelian theories, the commutator $[\mathcal{A}_\mu(x), \mathcal{A}_\nu(x)] = i\mathcal{A}^a_\mu(x)\mathcal{A}^b_\nu(x) f^{abc}T^c$ does not vanish, resulting in self-interactions of the gluon fields.[5] This is the case for QCD which is described by the non-Abelian gauge group $SU(3)_c$.[6] In general, ψ_f can be a set of quark fields charged in different representations of the gauge group. For QCD, the quark fields are charged in the fundamental representation of $SU(3)_c$. The covariant derivative makes the Lagrangian invariant under local (spacetime dependent) transformations of the gauge group. These are carried out by group elements $U(x)$ that transform the fields in the Lagrangian like

$$\begin{aligned}
\psi(x) &\to U(x)\psi(x), && (1.5)\\
\bar{\psi}(x) &\to \bar{\psi}(x)U^{-1}(x), && (1.6)\\
\mathcal{A}_\mu(x) &\to U(x)\mathcal{A}_\mu(x)U^{-1}(x) + i(\partial_\mu U(x))U(x)^{-1}. && (1.7)
\end{aligned}$$

The partition function and the action in Euclidean metric read

$$\begin{aligned}
Z &= \int \mathcal{D}\left[\mathcal{A}_\mu, \psi, \bar{\psi}\right] e^{-S[\mathcal{A}_\mu, \psi, \bar{\psi}]}, && (1.8)\\
S\left[\mathcal{A}_\mu, \psi, \bar{\psi}\right] &= \int \mathcal{L}(x) dx. && (1.9)
\end{aligned}$$

The path integral over the measure $\mathcal{D}\left[\mathcal{A}_\mu, \psi, \bar{\psi}\right]$ provides the quantization of the theory by integrating over all possible configurations of the quark and gluon fields. In principle, all correlation functions, and thus the entire dynamics of the theory can be derived from the partition function.

---

[5] Here we introduced the structure constants $if^{abc}T^c = [T^a, T^b]$.

[6] In this thesis we will deal with $SU(N)$, $Sp(2N)$ and $SO(N)$ groups corresponding to either local gauge symmetries or global flavor symmetries. We will indicate the gauge groups by the subscript $_c$ with the exception of G_2, which is always a gauge group in this work.

1.2.1 Asymptotic Freedom and Confinement

For a sufficiently small number of fermions, the fundamental degrees of freedom, quarks and gluons, are *asymptotically free*. This can be seen in the β function, which encodes the dependence of the running coupling on the renormalization scale μ as $\beta(g) = \partial g/\partial(\ln \mu)$. For the Lagrangian in Equation (1.3) with massless fermions and no scalar particles, the one-loop β function is given by [58–60]

$$\begin{aligned}\beta(g) &= -\left(\frac{11}{3}C_2(G) - \frac{4}{3}N_f C(r)\right)\frac{g^3}{16\pi^2} + \mathcal{O}(g^5) &\quad (1.10)\\ &= -\left(11 - \frac{2}{3}N_f\right)\frac{g^3}{16\pi^2} + \mathcal{O}(g^5) \quad \text{for } G = SU(3)_c, &\quad (1.11)\end{aligned}$$

where the quadratic Casimir operator in the adjoint is defined via $C_2(G)\delta_{ab} = f^{acd}f^{bcd}$ and $C(R)\delta_{ab} = \mathrm{tr}[T^a(R)T^b(R)]$ is a constant for each representation R. For QCD and the theories considered in this work, the β function is negative for sufficiently small numbers of flavors, implying that the coupling becomes arbitrarily small at large μ or equivalently large momentum transfers. As a result, at large energies, the theory can be treated using perturbation theory, where the Lagrangian is expanded in orders of the coupling g, which is only meaningful at small couplings. There are effects that arise exclusively in non-perturbative treatments, but are subordinate at large energies.

At small energies, the coupling remains strong, meaning that non-perturbative methods are indispensable. An emergent phenomenon backed by lattice calculations is *confinement* which disallows the observation of color charged states in isolation. The illustrative picture is that if you tried to pull apart color-charged objects, their potential energy becomes large enough to create pairs of particles that maintain confinement [61]. As a result, physical states have to be singlets of the color group. Quarks and gluons, by definition, transform nontrivially under transformations of the gauge group, and hence physical states have to be bound states of these objects called *hadrons*. In QCD, these are realized as quark-antiquark states called *mesons*, three-quark states called *baryons*, but also more exotic color singlet states like *tetraquarks*, *pentaquarks*, *glueballs*, or *hybrids* [4, 62–64].

1.2.2 Global Symmetries

Various phenomenologies, such as the particle spectrum of a theory, are connected to global symmetries. The global symmetries of QCD and its breaking patterns are well known. The approximate $SU(2)$ flavor symmetry resulting from the almost degenerate up and down quarks is often called *strong isospin*. Knowledge about the flavor symmetries of the theory is crucial to understanding its physics, also because according to *Noether's theorem*, continuous symmetries result in conserved quantities [65]. Less commonly known is that the flavor symmetry of QCD is the result of the complex nature of the fundamental representation of $SU(3)_c$ and that the symmetries and their breaking patterns change significantly when other representations are chosen. For a fixed number of flavors N_f, three different global symmetries can be realized by choosing fermions charged under complex, real, or pseudo-real representations.[7] In this thesis, we will only consider fundamental representations, but the global symmetries for non-fundamental representations are identical. Exemplary gauge groups with complex, real or pseudo-real fundamental representations are $SU(N)_c$ $(N > 2)$, $SO(N)_c$, and $Sp(2N)_c$[8] respectively.

Let us first consider the case realized in QCD, where the left- and right-handed components of the quark fields each form a multiplet of dimension N_f. The kinetic term of the fermionic part of the Lagrangian reads

$$\mathcal{L}_{f,\text{kin}} = \bar{\psi}\gamma_\mu D_\mu \psi = \psi^\dagger \gamma_4 \gamma_\mu D_\mu \psi, \tag{1.12}$$

where ψ and $\bar{\psi}$ are $2N_f$ vectors.

$$\psi = \begin{pmatrix} \psi_L^i \\ \psi_R^i \end{pmatrix}, \quad i = 1, ..., N_f \tag{1.13}$$

The projection operator projects out different parts of the γ_μ-matrices. In the chiral representation of the γ matrices, we can express the left- and right-handed parts of Equation (1.12) in terms of the Pauli matrices σ_j like

$$\psi^\dagger P_L \gamma_4 \gamma_\mu D_\mu \psi = \psi_L^\dagger \tau_\mu D_\mu \psi_L, \tag{1.14}$$

$$\psi^\dagger P_R \gamma_4 \gamma_\mu D_\mu \psi = \psi_R^\dagger \bar{\tau}_\mu D_\mu \psi_R, \tag{1.15}$$

where we have defined $\tau_\mu = (-i\sigma_j, \mathbb{1})$ and $\bar{\tau}_\mu = (i\sigma_j, \mathbb{1})$ and $\psi_{L/R}$ are two-index Weyl spinors. We can write

$$\mathcal{L}_{f,\text{kin}} = \begin{pmatrix} \psi_L^* \\ \psi_R^* \end{pmatrix}^T \begin{pmatrix} \tau_\mu D_\mu & 0 \\ 0 & \bar{\tau}_\mu D_\mu \end{pmatrix} \begin{pmatrix} \psi_L \\ \psi_R \end{pmatrix}, \tag{1.16}$$

---

[7] There are also theories that work with multiple fermions charged in different representations [66–81].

[8] $SU(2) = Sp(2)$ is the limiting case for small N both $SU(N)$ and $Sp(2N)$ and therefore plays a special role. However, the fundamental representation of $SU(2)_c$ is pseudo-real and therefore it will have the same global symmetries as $Sp(2N)_c$ gauge theories.

where we see that the left- and right-handed components transform differently and therefore the Lagrangian is invariant under $U(N_f) \times U(N_f)$ transformations that act separately on the two chiral components. This symmetry, however, is not realized in nature, as the physical symmetries are those that leave the partition function invariant. Quantum effects break the $U(1)$ axial symmetry, leaving an $SU(N_f) \times SU(N_f) \times U(1)$ [58, 82]. This is the physical symmetry of the kinetic part of the fermionic Lagrangian, sometimes referred to as *chiral symmetry* as it does not mix the two chiral components. Equation (1.3), also contains a fermionic mass term.

$$\mathcal{L}_{f,\text{mass}} = m_f \bar{\psi}\psi \tag{1.17}$$

Due to the absence of a γ_μ that distinguishes between the two chial components, they are no longer independent. As a result, in the presence of quark masses, the symmetry is reduced to $SU(N_f) \times U(1)$. The limit in which the quark masses vanish is often called the *chiral limit* because the chiral symmetry is restored. In nature the up and down quarks are very light and would naively allow for a description with an approximate chiral symmetry. As a consequence, states that differ only by their parity quantum number should be almost degenerate. However, the masses of the scalar and pseudo-scalar mesons differ drastically, pointing to another source for the breaking of the chiral symmetry. This is the chiral condensate $\langle 0|\bar{\Psi}(0)\Psi(0)|0\rangle$ that has the same quantum numbers as the mass term in the Lagrangian and is therefore not invariant under chiral rotations. If it takes a finite value, it will break the chiral symmetry. At large temperatures, the chiral condensate vanishes. Going to low temperatures, the theory undergoes a crossover, giving the chiral condensate a finite value, which *spontaneously breaks* the chiral symmetry. According to Goldstone's theorem, spontaneous breaking of global symmetries results in massless particles called Nambu-Goldstone bosons[9] that live on the coset between the flavor symmetry groups before and after breaking. In QCD, this coset spans an $SU(N_f)$ and hence there are $N_f^2 - 1$ pNGBs. They are realized as the pion triplet in $N_f = 2$ or the meson octet in $N_f = 3$.

1.2.3 Real and Pseudo-real Representations

As already mentioned, the global symmetries and their breaking patterns, and with that the dynamics of the theory, will change when different fermion representation are chosen. We will now consider the two remaining cases of real and preudo-real

---

[9] If they obtain a mass via some other mechanism, like explicit fermion masses, they are referred to as pseudo-Nambu-Goldstone bosons (pNGBs).

representations closely following [83].[10] In these cases, the kinetic term of the fermionic part will mix left- and right-handed components before any symmetry breaking, and the global symmetry will be enlarged, leading to different particle spectra. We will carry out the calculations for the pseudo-real case for $N_f > 1$[11] and give the final expressions for the real case. Written as Equation (1.16), it seems that the Lagrangian is not invariant when the left- and right- handed components are transformed into one another. In the pseudo-real case, however, it turns out that the conjugate field $\tilde{\psi}_R = (\sigma_2 \Sigma)\psi_R^*$ will transform similarly (in the same color representation) as ψ_L. Here, Σ is an antisymmetric matrix acting in color space[12] and σ_2 is the charge conjugation matrix acting on two-index Weyl vectors that can be identified as the second Pauli matrix. We can make use of this by rewriting the right-handed part of Equation (1.16) as

$$\begin{aligned}\mathcal{L}_{f,\mathrm{kin},R} &= \psi_R^\dagger \bar{\tau}_\mu D_\mu \psi_R && (1.18)\\ &= -\psi_R^\dagger \sigma_2 \tau_\mu^T \sigma_2 \Sigma D_\mu^T \Sigma \psi_R, && (1.19)\end{aligned}$$

where we have used $\bar{\tau}_\mu = \sigma_2 \tau_\mu^T \sigma_2$ and $D_\mu = -\Sigma D_\mu^T \Sigma$. The latter relies on the pseudo-reality condition for the generators of the gauge group $T_a = -\Sigma T_a^T \Sigma$. We also drop total derivatives. By transposing the entire term, which we are free to do since it does not carry any open indices, taking into account the anticommutativity of the Grassmann fields, we can write Equation (1.19) in terms of the conjugate field $\tilde{\psi}_R$.

$$\begin{aligned}\mathcal{L}_{f,\mathrm{kin},R} &= \psi_R^T \sigma_2 \Sigma \tau_\mu D_\mu \sigma_2 \Sigma \psi_R^* && (1.20)\\ &= \tilde{\psi}_R^\dagger \tau_\mu D_\mu \tilde{\psi}_R && (1.21)\end{aligned}$$

---

[10] This paper investigates the special cases called *adjoint* and *two-color QCD* as all adjoint representations are real and the fundamental representation of $SU(2)_c$ is pseudo-real. The nomenclature using (pseudo-) real is more general, but the derivation presented here is identical.

[11] The flavor symmetries for $N_f = 1$ in the pseudo-real and real case are different and will not be discussed in this work.

[12] For this thesis, we consider multiple antisymmetric matrices. For $N_f = 2$, these matrices are numerically identical and we refer to the color matrix as Σ and to the flavor matrix as E. For general N_f, we refer to the matrix as F.

Combining this again with the left-handed part gives

$$\mathcal{L}_{f,\mathrm{kin}} = \begin{pmatrix} \psi_L^* \\ \tilde{\psi}_R^* \end{pmatrix}^T \begin{pmatrix} \tau_\mu D_\mu & 0 \\ 0 & \tau_\mu D_\mu \end{pmatrix} \begin{pmatrix} \psi_L \\ \tilde{\psi}_R \end{pmatrix} \tag{1.22}$$

$$= \Psi^\dagger \begin{pmatrix} \tau_\mu D_\mu & 0 \\ 0 & \tau_\mu D_\mu \end{pmatrix} \Psi, \tag{1.23}$$

where we have introduced the $2N_f$ component flavor vector

$$\Psi = \begin{pmatrix} \psi_L \\ \sigma_2 \Sigma \psi_R^* \end{pmatrix} \tag{1.24}$$

$$= \begin{pmatrix} P_L \psi \\ C \Sigma P_L \bar{\psi}^T \end{pmatrix}. \tag{1.25}$$

The second line is written in terms of Dirac spinors, explicitly writing the projection operators. In the real case, we will obtain a similar expression which will result in the same structure but with the four spinor replaced by

$$\Psi = \begin{pmatrix} \psi_L \\ \sigma_2 \psi_R^* \end{pmatrix}, \tag{1.26}$$

only differing by the absence of the color matrix Σ and the fact that the fermions are charged in a real representation. In both cases, for $N_f > 1$, this showcases the manifestation of the global $U(2N_f)$ symmetry which, up to discrete symmetries, is broken to $SU(2N_f)$ by the axial anomaly [83]. Next, like in the complex case, we want to investigate the symmetries of the mass term.

$$\bar{\psi}\psi = \psi_L^\dagger \psi_R + \psi_R^\dagger \psi_L \tag{1.27}$$

$$= \begin{pmatrix} \psi_L^* \\ \psi_R^* \end{pmatrix}^T \begin{pmatrix} 0 & \mathbb{1}_{N_f} \\ \mathbb{1}_{N_f} & 0 \end{pmatrix} \begin{pmatrix} \psi_L \\ \psi_R \end{pmatrix} \tag{1.28}$$

$$= \begin{pmatrix} \psi_L \\ \sigma_2 \Sigma \psi_R^* \end{pmatrix}^T \sigma_2 \Sigma \begin{pmatrix} 0 & \mathbb{1}_{N_f} \\ -\mathbb{1}_{N_f} & 0 \end{pmatrix} \begin{pmatrix} \psi_L \\ \sigma_2 \Sigma \psi_R \end{pmatrix} + \text{h.c.} \tag{1.29}$$

$$= \frac{1}{2} \left[\Psi^T \sigma_2 \Sigma F \Psi - \Psi^\dagger F \sigma_2 \Sigma \Psi^* \right] = \frac{1}{2} \left[\Psi^T \sigma_2 \Sigma F \Psi + \text{h.c.} \right] \tag{1.30}$$

Here, F is the antisymmetric matrix acting in flavor space. In the case of massive fermions, the symmetry of the theory is given by the group elements U of $SU(2N_f)$ that leave the equation above invariant. This is exactly the defining property of the $Sp(2N_f)$ groups, $U^T F U = F$. This shows that in the presence of a mass term, the symmetry is reduced from $SU(2N_f)$ to $Sp(2N_f)$. A similar argument holds for the real case, where the mass term can be written as

$$\bar{\psi}\psi = \frac{m_f}{2}\left(\Psi^T \sigma_2 G \Psi + \text{h.c.}\right). \tag{1.31}$$

The matrix G is a symmetric matrix. The group elements that leave the mass term invariant in the real case fulfill $U^T G U = G$, which is the defining property of $SO(2N_f)$ groups. This means that in the presence of a mass term, gauge theories with N_f fermions in a real representations inherit an $SO(2N_f)$ flavor symmetry. In summary, there are three distinct flavor symmetry breaking patterns resulting from chiral symmetry breaking for different fermion representations.

$$\text{complex:} \qquad SU(N_f) \times SU(N_f) \times U(1) \to SU(N_f) \times U(1) \tag{1.32}$$
$$\text{pseudo-real:} \qquad SU(2N_f) \to Sp(2N_f) \tag{1.33}$$
$$\text{real:} \qquad SU(2N_f) \to SO(2N_f) \tag{1.34}$$

The number of resulting pNGBs is given by the number of broken generators, which is $N_f^2 - 1$ in the complex case, $N_f(2N_f - 1) - 1$ in the pseudo-real case and $N_f(2N_f + 1) - 1$ in the real case. The $U(1)$ in the complex case is related to baryon number conservation. Note how it is absent in the real and pseudo-real cases. This means that these theories do not have an equivalent of the baryon number quantum number and therefore no baryons, which could be protected from decays by its conservation.

1.2.4 Low Energy Description with Chiral Perturbation Theory

A powerful tool in working with non-Abelian gauge theories is *chiral perturbation theory* (ChPT). ChPT describes the theory in terms of the lightest mesons, the pNGBs of the theory, and is expanded in orders of $\mathcal{O}(m_\pi/f_\pi)$ where m_π is the mass of the pNGB and f_π its decay constant. Every higher order of m_π/f_π introduces *low-energy constants* (LECs) that need to be fixed, for example, using lattice field theory. The chiral description is valid for low values of m_π/f_π, which correspond to light pNGBs compared to any other scale of the theory. Furthermore, pure ChPT does not contain other particles and is therefore only valid in the regime where the pNGBs are the dominant degrees of freedom, but it is also possible to include additional states [84]. Once the ChPT Lagrangian is known to the desired order, dynamics can be calculated perturbatively. This makes it a powerful tool, especially at low energies, which are common for dark matter, for example for calculations on the relic density, as it allows for analytic calculations in contrast to the lattice, which requires significant computational resources. In the following, we will introduce the basic concepts of ChPT applied to $Sp(4)_c$ gauge theory with $N_f = 2$ fundamental flavors relevant for our work by writing down the Lagrangian to first order and adding the Wess-Zumino-Witten (WZW) term which will describe the number-lowering cannibalization process and a term for the vector mesons. ChPT can be written as fluctuations in the orientation of the chiral condensate Σ

$$\Sigma = e^{i\pi/f_\pi}\Sigma_0 e^{i\pi^T/f_\pi}, \tag{1.35}$$

which for $N_f = 2$ transforms under the action $U \in SU(4)$ flavor as

$$\Sigma \to U\Sigma U^T. \tag{1.36}$$

There are five pNGBs $\pi_{1,\dots,5}$ that correspond to the broken $SU(4)$ generators that define the coset $SU(4)/Sp(4)$. The generators are defined in Appendix A and we use the basis defined in Equation (A.27). The Goldstone matrix π in Equation (1.35) takes the form

$$\pi = \sum_{n=1}^{5} \pi_n X^n = \frac{1}{2\sqrt{2}} \begin{pmatrix} \pi_3 & \pi_1 - i\pi_2 & 0 & \pi_5 - i\pi_4 \\ \pi_1 + i\pi_2 & -\pi_3 & -\pi_5 + i\pi_4 & 0 \\ 0 & -\pi_5 - i\pi_4 & \pi_3 & \pi_1 + i\pi_2 \\ \pi_5 + i\pi_4 & 0 & \pi_1 - i\pi_2 & -\pi_3 \end{pmatrix}. \tag{1.37}$$

By demanding reality, Lorentz invariance, chiral symmetry invariance, parity, and charge conjugation symmetry, we can write down the chiral Lagrangian in terms of the chiral condensate.

$$\mathcal{L}_\pi = \frac{f_\pi}{4}\mathrm{tr}\left[\partial_\mu\Sigma\partial^\mu\Sigma^\dagger\right] - \frac{\mu^3}{2}\left(\mathrm{tr}\left[M\Sigma\right] + \mathrm{tr}\left[\Sigma^\dagger M^\dagger\right]\right) + \text{higher orders} \tag{1.38}$$

Here, μ has the dimension of mass and is related to the chiral condensate as $\langle \bar{u}u + \bar{d}d\rangle = \mu^3\Sigma_0$. This Lagrangian can be expanded by adding terms of higher order. Identifying the vacuum alignment as $\Sigma_0 = E$ [85], we can express the Lagrangian in terms of a kinetic and a mass term which gives rise to interactions of even numbers of pNGBs.

$$\mathcal{L}_{\pi,\text{kin}} = \frac{1}{2}\sum_{n=1}^{5}\partial_\mu\pi_n\partial^\mu\pi_n - \frac{1}{12f_\pi^2}\sum_{k,n=1}^{5}\left(\pi_k\pi_k\partial_\mu\pi_n\partial^\mu\pi_n - \pi_k\partial_\mu\pi_n\partial^\mu\pi_n\right) + \mathcal{O}\left(\frac{\pi^6}{f_\pi^4}\right) \tag{1.39}$$

$$\mathcal{L}_{\pi,\text{mass}} = -\frac{m_\pi^2}{2}\sum_{n=1}^{5}\pi_n^2 + \frac{m_\pi^2}{48f_\pi^2}\left(\sum_{n=1}^{5}\pi_n^2\right)^2 + \mathcal{O}\left(\frac{\pi^6}{f_\pi^4}\right) \tag{1.40}$$

A five-point interaction can be added that will describe the number-lowering canibalization process by the WZW action [86, 87]. The corresponding Lagrangian is

$$\begin{aligned}\mathcal{L}_{\text{WZW}} = \frac{2N_c}{10\sqrt{2}\pi^2 f_\pi^5}\epsilon^{\mu\nu\rho\sigma}\big(&\pi_1\partial_\mu\pi_2\partial_\nu\pi_3\partial_\rho\pi_4\partial_\sigma\pi_5 - \pi_2\partial_\mu\pi_1\partial_\nu\pi_3\partial_\rho\pi_4\partial_\sigma\pi_5\\ &+\pi_3\partial_\mu\pi_1\partial_\nu\pi_2\partial_\rho\pi_4\partial_\sigma\pi_5 - \pi_4\partial_\mu\pi_1\partial_\nu\pi_2\partial_\rho\pi_3\partial_\sigma\pi_5\\ &+\pi_5\partial_\mu\pi_1\partial_\nu\pi_2\partial_\rho\pi_3\partial_\sigma\pi_4\big),\end{aligned} \tag{1.41}$$

where N_c is the number of colors. Note that up to this point, the Lagrangian does not involve any LECs and the only parameters to fix are the mass and decay constant of the pions. Finally, we may introduce vector particles, for example, through the concept of *hidden local symmetry* [85, 88, 89]. This introduces a kinetic term and a mass term for both vector mesons and axial-vector mesons, as well as an interaction with the pNGBs via $\mathcal{L}_{\rho\pi\pi}$ that includes $g_{\rho\pi\pi}$ which is the phenomenological coupling of a three-point vertex involving two pNGBs and a vector meson. The framework of hidden local symmetry ensures that the axial-vector mesons are heavier than the vector mesons. In this work, we will neglect the heavier axialvectors given their higher mass. The value of $g_{\rho\pi\pi}$ is sometimes estimated by the *Kawarabayashi-Suzuki-Riazuddin-Fayyazuddin* (KSRF) relation [90, 91] to $2g_{\rho\pi\pi} \approx m_\rho^2/f_\pi^2$, but we will see that this is not a good description for our data in $Sp(4)$. We will obtain the value of $g_{\rho\pi\pi}$ non-perturbatively in Section 3.4.2. The WZW term also receives contributions from vector mesons, which we will not consider in this work [85]. The final first-order chiral Lagrangian relevant for our theory is then

$$\mathcal{L}_{\text{ChPT}} = \mathcal{L}_{\pi,\text{mass}} + \mathcal{L}_{\pi,\text{kin}} + \mathcal{L}_{\rho,\text{mass}} + \mathcal{L}_{\rho,\text{kin}} + \mathcal{L}_{\rho\pi\pi} + \mathcal{L}_{\text{WZW}}, \tag{1.42}$$

and depends on m_π, f_π, m_ρ, and $g_{\rho\pi\pi}$, which we will determine using lattice field theory and N_c given by the gauge group.

1.2.5 Minimal SIMP Theories

As explained in Section 1.2.3, the use of fundamental fermions in real or pseudo-real representations of the gauge group enlarges the flavor symmetry compared to the complex case. As a result, the larger meson multiplets enable new processes. SIMP theories rely on a number-lowering cannibalization process that, disregarding a two-to-one process or three-to-one process which would involve a sizable 4-point vertex, is minimally realized by a three-to-two process. Theories with a WZW term always inherit such a process among pNGBs [51], also referred to *dark pions* in this context. We will refer to theories with two fundamental pseudo-real fermions as a *minimal ralization* of SIMPs, as they contain exactly five dark pions, all of which participate in the cannibalization process. In addition, the theory has also gained significant interest in other BSM models such as *composite Higgs* or *partial top compositeness* [81, 92–97], and other dark matter dark matter models [98–104]. Theories with two real fermions contain 9 dark pions, making the theory more intricate. In the complex case, the WZW term is only realized at $N_f \geq 3$.

The relic-density mechanism of SIMP [50–52] theories has been investigated in effective descriptions before by solving the Boltzmann equations. It was shown that they can provide the dark matter relic density, as well as the self-interaction cross section necessary to address the small-scale structure problems. However, as SIMP theories are motivated by *ultraviolet* (UV) complete confining gauge theories, which require a complete non-perturbative treatment, in order to capture all dynamics, it is important to employ non-perturbative methods like lattice field theory that will scrutinize the LECs needed in effective descriptions. In this work we will investigate non-perturbative signatures of SIMP dark matter candidate theories in the real and pseudo-real case.

In Chapter 2, a neutron star admixed with dark matter described by the G_2 gauge theory with $N_f = 1$ fundamental fermions is investigated. Although this theory itself does not inherit the necessary cannibalization process, it does so at $N_f = 2$ and is used as a proxy to investigate SIMP-like theories. The lattice calculations have been performed in previous work and are only utilized here. Therefore, we refrain from a detailed description of the flavor symmetry and the techniques used and refer to [105, 106].

In Section 3.4, we investigate a second candidate theory, which is $Sp(4)_c$ gauge theory with two fundamental fermions, the minimal realization of SIMP. $SU(2)_c$ generates the same flavor symmetry, but firstly, it has already been studied in great detail [102, 107–118], and secondly, doubling the number of colors might change the dynamics of the theory drastically. The aim of this work is to calculate quantities to compare with astrophysical data in order to falsify whether $Sp(4)_c$ is a viable dark matter candidate and to provide estimates of LECs for effective descriptions. Numerous lattice spectroscopy calculations have been performed before. Here, we perform non-perturbative scattering analyses on the lattice using the Lüscher quantization condition in two scattering channels which are both interesting for dark matter phenomenology. The maximal scattering channel is most likely dominant at low energies, which is particularly important for dark matter phenomenology. The other contains the vector mesons and the three-to-two process which motivates this model.

1.3 Lattice Field Theory

Lattice field theory is a numerical tool to calculate non-perturbative phenomena of strongly-interacting theories by sampling gauge configurations. Here, we only introduce the most basic concepts and refer to textbooks for a detailed introduction [119–121]. In a first step, spacetime is Wick rotated so that we work with imaginary time $t \to it$ and with the Euclidean metric $g_{\mu\nu} = \delta_{\mu\nu}$. Consequently, observables calculated from lattice field theory are *a priori* not valid in Minkowski space. In order to obtain physical quantities, one has to ensure that the observables can be translated into Minkowski space. Fortunately, this is the case for observables such as particle spectra considered in this work. In a second step, spacetime is discretized on a four-dimensional hypercubic lattice of size $N_L^3 \times N_T$, where N_L is the number of sites in the spatial direction and N_T is the number of sites in the temporal direction. The physical volume $L^3 \times T = a^4 N_L^3 N_T$ can be calculated from the *lattice constant* which is the distance between two lattice sites n. The gauge fields are described by the *link variables* $U_\mu(n)$ which are defined between neighboring lattice sites. The subscript $_\mu$ denotes the direction of the link $n + \mu = (n_1 + \delta_{\mu 1}, n_2 + \delta_{\mu 2}, n_3 + \delta_{\mu 3}, n_4 + \delta_{\mu 4})$. The link variables are related to the gauge fields by

$$U_\mu(n) = \exp(ia\mathcal{A}_\mu(n)). \tag{1.43}$$

By construction, this introduces two cutoffs. The lattice constant introduces an UV cutoff, and the volume of the lattice introduces an *infrared* cutoff, which means that we are bound to smallest and largest scales that we can resolve.

1.3.1 Importance Sampling

Without any fermions, the expectation value of operators in Euclidean spacetime may be calculated using the path integral

$$\langle O \rangle = \frac{1}{Z} \int \mathcal{D}A_\mu e^{-S_G[U_\mu]} O[U_\mu]. \tag{1.44}$$

In contrast to perturbation theory, where the action is expanded in orders of the gauge coupling g, on the lattice the integral over the gauge fields is approximated by interpreting the exponential $e^{-S_G[A_\mu]}$ as a probability. We can then generate gauge configurations according to the distribution [122]

$$\rho(U_\mu) = \frac{\exp(-S_G[U_\mu])}{\int \mathcal{D}[U_\mu] \exp(-S_G[U_\mu])}. \tag{1.45}$$

The sum

$$\langle O \rangle = \frac{1}{N} \sum_{\{U_\mu\}} O[U_\mu], \tag{1.46}$$

over N configurations approximates the path integral if the set of gauge configurations $\{U_\mu\}$ follows the distribution $\rho(U_\mu)$. In practice, sampling the whole space of possible gauge configurations is unfeasible, and one has to rely on statistical analyses. The probability interpretation is valid as long as ρ is real and positive definite, which is an issue in QCD and other gauge theories if you want to calculate, for example, observables at finite baryonic densities. This is the root cause of the infamous *sign problem.* In Chapter 2 we will make use of the absence of the sign problem in G_2 gauge theory by using finite density calculations to describe dark matter in neutron stars. In the current form, we do not account for any fermionic degrees of freedom. We can include dynamical fermions by adding an *effective fermion action* S_F^{eff} to the gauge action.

$$S'[U_\mu] = S_G[U_\mu] + S_F^{\text{eff}}[U_\mu] \tag{1.47}$$

The effective fermion action can be realized by different fermion discretizations. Various formulations exist, designed to balance large computational costs with drawbacks like lattice artifacts or lost symmetries. We refer to textbooks for a detailed introduction [119–121]. The results of lattice field theory include systematic uncertainties, which must be carefully estimated and controlled. The use of a finite hypercubic lattice introduces *finite-volume effects* and *discretization artifacts.* The physics of the continuum theory is recovered in the limit of an infinite lattice with infinitely small lattice spacing.

$$L \to \infty \tag{1.48}$$
$$T \to \infty \tag{1.49}$$
$$a \to 0 \tag{1.50}$$

There are methods to extrapolate to both the infinite volume and continuous spacetime. The physical volume of the lattice is not known before a lattice calculation. Only after the scale has been set, for example by identifying a state with a physical particle and its mass, is the lattice constant, and thus the volume defined in physical units. This is not always possible for BSM theories, as the masses of the particles in the spectrum are at most constraint. On the other hand, it means that a whole system of theories at different scales is explored. In this case. It is usually most practical to work with dimensionless ratios of quantities.

The input parameters of lattice the calculations performed in this work are the number of spatial and temporal lattice sites, as well as the unphysical inverse bare gauge coupling $\beta = \frac{2N_c}{g^2}$ and fermion masses m_f. Due to asymptotic freedom, the continuum theory is recovered in the limit $\beta \to \infty$. Different discretizations can be examined by keeping the number of lattice sites fixed and simultaneously increasing the value of β. The mass of the bare fermions can then be adjusted to obtain a theory with similar dynamics. These combinations of input parameters are referred to as *line of constant physics*, which can be defined, for example, by the mass ratio of two particles in the theory. In this way, the behavior of the theory for finer lattices can be examined, and an extrapolation to the continuum can be performed. Once a is smaller than the relevant hadronic scales, discretization artifacts should become negligible.

For theories with chiral symmetry breaking, the leading finite-volume effects can be estimated. For example, the mass of the pNGB m_π^∞ can be extrapolated by fitting the finite-volume energies $E_\pi(L)$ [95, 123].

$$E_\pi(L) = m_\pi^\infty \left(1 + A(m_\pi^\infty L)^{-3/2} \exp(-m_\pi^\infty L)\right) \tag{1.51}$$

This form is motivated by chiral lattice perturbation theory in which A is not a free parameter. Following [95], we treat it as free and fit the energy levels to A and m_π^∞. Similar expressions can be derived for the decay constants and other mesons. The quantity $m_\pi L$ is often used to estimate the relevance of finite-volume effects. In Chapter 3, we will employ the so-called *Lüscher formalism* which relates finite-volume effects to infinite-volume scattering parameters, but even in this framework, exponential finite-volume effects have to be negligible.

In this work, we discretize the Euclidean action using the standard Wilson plaquette action and two mass-degenerate unimproved Wilson fermions [124]. The gauge configurations are generated using the Hybrid Monte Carlo algorithm [125]. The generation of gauge ensembles and the measurements of observables were performed using the HiRep code [110, 126], which was extended to symplectic gauge groups. We will introduce lattice techniques specific to this work in Section 3.3.

Chapter 2

SIMP Dark Matter in Neutron Stars

Given the lack of a direct detection of dark matter, it is more necessary than ever to exploit all thinkable avenues to learn about the true nature of dark matter. We have found no evidence that dark matter is subject to any interactions besides gravity at all, but the small-scale structure problems motivate the investigation of self-interacting dark matter models. While dark matter self-interactions might be elusive at ordinary scales, they might become very relevant under extreme conditions. One of the most extreme conditions in the universe can be found in neutron stars which are the most compact objects in the universe apart from black holes. Given the large amount of dark matter, it will necessarily accumulate in neutron stars. There has been work on estimating the possible amount of dark matter neutron stars, and it might not exceed $\sim 1\%$ [127–129] but nonetheless it is worthwhile to investigate whether dark matter can have a measurable impact on the macroscopic parameters of neutron stars. There has been an exhaustive list of works covering the topic of dark matter in neutron stars forming *mixed stars* [128–163], however, none of them considers strongly-interacting dark matter calculated non-perturbatively [164]. In the introduction, we have motivated the class of SIMP models and the need for non-perturbative methods. In this chapter, we examine the effects of one specific SIMP candidate as a proxy theory.

The main reason why there are no lattice calculations on neutron star properties is the sign problem which is present in QCD and does not allow for the calculations of correlation functions at finite baryonic chemical potentials. But this is not present in all gauge theories, like G_2 or $Sp(4)_c$, for example. $Sp(4)_c$ does not naively inherit any fermionic bound states without which there is no Fermi pressure counteracting the gravitational pull, which is a great advantage for constructing stable compact objects. G_2 gauge theory forms fermionic bound states already at one fermionic flavor. Although the single-flavor theory does not include a three-to-two cannibalization process, it does so for two flavors. In this work, we will use lattice calculations at finite densities in G_2 gauge theory to estimate the potential signatures of SIMP models on neutron stars.

The main characteristics of neutron stars can be captured in their macroscopic parameters such as mass and radius. Recent developments in gravitational wave detection grant access to another parameter, the *tidal deformability*, which can be extracted from neutron star merger events. The first detection of a merger of neutron stars with gravitational waves was *GW170817* in 2017 which was detected by LIGO [165]. In 2019, they have observed the event *GW190814* [166], which most likely also originated from the merger of two neutron stars as well, but no electromagnetic counterpart was found. Additionally, two events of neutron star-black hole mergers were detected in 2020 [167]. The number of observations of neutron star mergers is expected to increase when next generation gravitational wave detectors like the *Laser Interferometer Space Antenna* [168] or the *Einstein telescope* [169] start operating.

The most common tool in neutron star physics is the Tolmann-Oppenheimer-Volkoff (TOV) equations. Their integration yields the macroscopic observables of neutron stars given an equation of state which is obtained from the microphysical dynamics. The tidal deformability can be calculated simultaneously in the same framework. The TOV equations can be extended to accommodate two fluids, assuming that the non-gravitational interaction between the two is negligible. The gravitational interactions are then conveyed by a common metric function.

The ingredient for these calculations are the equations of state of ordinary QCD matter and dark matter, which capture all microscopic dynamics required. In this work, we will use an equation of state from finite-density lattice calculations in G_2 gauge theory to describe dark matter. We complement this by the use of equations of states for ordinary matter in a model-agnostic way that is able to meet the observational constraints. In Section 2.1, we will introduce the equations of state used, in Section 2.2, we will introduce the theoretical framework used to calculate the mass, radius, and tidal deformability, and show results and comparisons with observation in Section 2.3.

2.1 Equations of State

The TOV equations require the equation of state in the form $\varepsilon(p)$ where ε is the energy density and p is the pressure. Together with the number density n and the chemical potential μ they must satisfy $n\mu = p + \varepsilon$ for thermodynamic consistency. In this section, we describe the main characteristics of the equations of state employed and present our interpolation method.

2.1.1 G_2 QCD

G_2 QCD is a QCD-like theory in which the fermions are charged under the non-Abelian group G_2 [170, 171]. Like QCD, it is a confining and asymptotically free theory. A special feature of G_2 QCD is that chiral symmetry breaking already occurs in the one-flavor theory and dark baryons can be built with any number of dark quarks. This is because the fundamental representation of G_2 is 7-dimensional and occurs in the tensor product $\mathbf{7} \otimes \mathbf{7}$,[1] and hence the addition of a fundamental fermion to any state built from fundamental fermions can in turn form a color singlet [83, 106, 170]. Further, the sign problem at finite baryon chemical potential is absent in this theory. We consider G_2 QCD with $N_f = 1$ fundamental flavor [105, 106] that has already been shown to support a compact object similar to a neutron star [172]. A detailed discussion of the spectrum and vacuum properties can be found in [105, 106, 171].

Our fermionic dark matter candidate is the three dark-quark state and we set the scale by fixing its mass to the mass of the dark matter particle. The equation of state has been obtained for two sets of lattice parameters which result in different spectra. The lightest particle in the theory is the pseudo-scalar dark pion, which is unstable to decays to the Standard Model via messengers. The dark matter candidate is the lightest fermionic particle which has a mass of four times the mass of the dark pion in the light ensemble and three times the mass of the dark pion in the heavy ensemble. This is not an input to the lattice calculations, but a result thereof. We can investigate various physical scenarios by identifying the mass of the dark matter candidate with different values compared to the mass of the neutron.

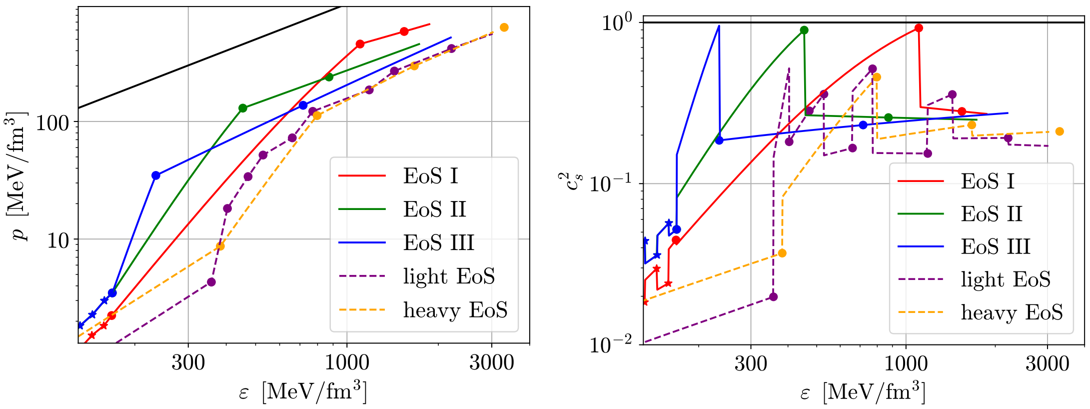

Figure 1: The equations of state (left) and the resulting speed of sound (right) [106, 173] used in this work. Here, the dark matter candidate mass is chosen to be the mass of the neutron for comparison. The end of the lines indicate the maximum value for the pressure for the respective equation of state used in this work. The black line indicates $\varepsilon = p$ and $c_s^2 = 1$ respectively. For the ordinary matter equation of state, the stars denote the results from NChPT while the dots show the endpoints of the piecewise polytropes. For the dark matter equation of state, points denote lattice data.

2.1.2 Ordinary Matter

For ordinary matter, we work with the equations of state of [173]. This work uses *piecewise polytropes*, to interpolate between a low-density regime described by *nuclear chiral perturbation theory* (NChPT) [174] and a high-density regime described by perturbative QCD (pQCD) [175]. pQCD is valid at densities much higher than those found in neutron stars, but nevertheless, the equation of state describing neutron stars should ultimately also describe the pQCD regime.

For this study, we used 3 limiting equations of state labeled EoS I, II, and III from [173]. Equations of state are often labeled as *soft* or *stiff*. In stiff equations of state, the pressure increases rapidly with increasing density, resulting in a high speed of sound. The resulting neutron stars are more resistant to compression, leading to larger masses, radii, and tidal deformabilities, whereas the opposite is true for soft equations of state. EoS I is the softest of the three, barely reaching the two solar mass limits. EoS II yields a maximal mass. EoS III is the stiffest and while it might be too stiff to describe an ordinary neutron star, we still include it in our analysis as the addition of dark matter to a neutron star can result in

---

[1] We will denote irreducible representations in this work by boldface numbers indicating their dimensionality.

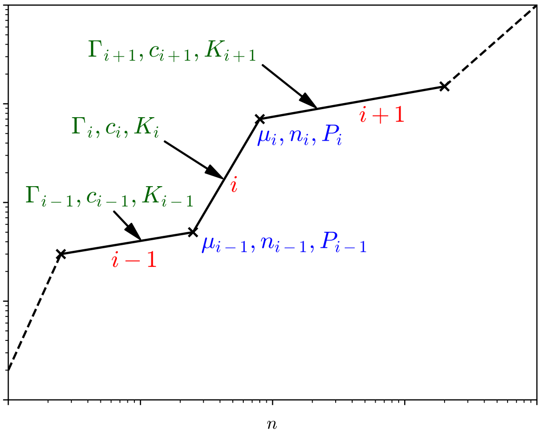

Figure 2: An illustration of the interpolating method used for all equations of state in this work. The ith polytrop is valid from n_{i-1} to n_i. The parameters of the next polytrope are obtained interatively from low to high pressures.

smaller masses and radii. Therefore, it might be possible to meet observational constraints when considering mixed neutron stars. We will employ central pressures larger than the ones stated in [173] as the addition of dark matter can allow for stable solutions at larger central pressures [176, 177]. Figure 1 shows the different equations of state and the speed of sound for ordinary and dark matter along with the equation of state. The speed of sound is allowed to be discontinuous.

We extend the equations of state below the NChPT data points in [173] by interpolating from zero using a polytrope with adiabatic index $\Gamma = 5/3$. This corresponds to a free Fermi gas and coincides with the equation of state $n \propto (\mu^2 - m_n^2)^{3/2}$ for low densities where m_n is the mass of the neutron. The same applies to the equation of state of dark matter with the mass replaced with the mass of the dark matter candidate. We do not include an equation of state for the crust, which should not affect the results for the mass but could influence the radius.

2.1.3 Interpolation using Polytropes

In order to use the lattice results in the TOV equations we have to convert them to pressure p and energy density ε. In order to ensure thermodynamic consistency $n\mu = p + \varepsilon$, we use the framework of piecewise polytropes to interpolate between data points. The polytropic equation of state is defined as [173, 178]

$$p = Kn^{\Gamma}, \tag{2.1}$$

where n is the number density and Γ is called the adiabatic index. The energy density is fixed by

$$d\left(\frac{\varepsilon}{n}\right) = -p\; d\left(\frac{1}{n}\right), \tag{2.2}$$

$$\varepsilon = cn + \frac{K}{(\Gamma - 1)} n^{\Gamma}, \tag{2.3}$$

where in the second line an integration has been performed, introducing an integration constant c. From $n\mu = p + \varepsilon$ follows for the chemical potential.

$$\mu = c + \frac{\Gamma}{\Gamma - 1} K n^{\Gamma - 1}. \tag{2.4}$$

This formalism is used to interpolate between data points, see Figure 2 for an illustration. The ith polytrope, valid from n_{i-1} to n_i, depends on the parameters c_i, K_i and Γ_i. In the following, we will denote the functions depending on the number density and the ith parameters as $p_i(n)$, $\varepsilon_i(n)$ and $\mu_i(n)$, and the values of these functions at n_i as p_i, ε_i, μ_i.

We set $c_0 = m_C$ for the first polytrope, as $\mu = m_C$ holds at low density. The other assumption is that $\Gamma_0 = 5/3$, which describes a free Fermi gas. This parameterization coincides with $n = c(\mu^2 - m_C^2)^{3/2}$ at low densities. Demanding continuity, one can use the following formulas to find the parameters of the next piece of the polytrope,

$$\begin{aligned}
\mu_{i+1} - \mu_i &= \mu_{i+1}(n_{i+1}) - \mu_1(n_i) && (2.5)\\
&= c_{i+1} + K_{i+1}\frac{\Gamma_{i+1}}{\Gamma_{i+1} - 1} n_{i+1}^{\Gamma_{i+1}-1} - c_{i+1} - K_{i+1}\frac{\Gamma_{i+1}}{\Gamma_{i+1} - 1} n_i^{\Gamma_{i+1}-1} && (2.6)\\
&= K_{i+1}\frac{\Gamma_{i+1}}{\Gamma_{i+1} - 1}(n_{i+1}^{\Gamma_{i+1}-1} - n_i^{\Gamma_{i+1}-1}) && (2.7)\\
&= K_i n_i^{\Gamma_i - \Gamma_{i+1}} \frac{\Gamma_{i+1}}{\Gamma_{i+1} - 1}(n_{i+1}^{\Gamma_{i+1}-1} - n_i^{\Gamma_{i+1}-1}), && (2.8)
\end{aligned}$$

where in the last line we have eliminated the yet unknown K_{i+1} by demanding continuity in the pressure $p_i(n_i) = p_{i+1}(n_i)$. The following expression can be solved by a zero search algorithm to find Γ_{i+1}

$$\Gamma_{i+1} K_i n_i^{\Gamma_i - \Gamma_{i+1}} = \frac{\mu_{i+1} - \mu_i}{n_{i+1}^{\Gamma_{i+1}} - n_i^{\Gamma_{i+1}}}(\Gamma_{i+1} - 1). \tag{2.9}$$

K_{i+1} and c_{i+1} are then obtained from continuity in pressure and chemical potential, respectively. We will also need the pressure at the start of the next polytrope for the next iteration, which is given by the polytropic equation.

$$K_{i+1} = n_i^{-\Gamma_{i+1}} P_i \tag{2.10}$$

$$c_{i+1} = \mu_{i+1} - \frac{K_{i+1} n_{i+1}^{\Gamma_{i+1}-1} \Gamma_{i+1}}{\Gamma_{i+1} - 1} \tag{2.11}$$

$$P_{i+1} = K_{i+1} n_{i+1}^{\Gamma_{i+1}} \tag{2.12}$$

For the first polytrope, K_0 has to be calculated once from the first data point of μ and n via

$$K_0 = (\mu_0 - c_0) \frac{\Gamma_0 - 1}{\Gamma_0} n_0^{1-\Gamma_0}. \tag{2.13}$$

Finally, the speed of sound is given by

$$c_{s,i}^2 = \frac{dp}{d\varepsilon} = \frac{dp}{dn} \left(\frac{d\varepsilon}{dn} \right)^{-1} = \frac{\Gamma_i p}{p + \varepsilon}. \tag{2.14}$$

2.2 TOV Equations and Tidal Deformability

In this section, we describe the framework used to build a mixed state from the two-fluid TOV equations given an equation of state and how stable solutions can be identified. Afterwards, we will describe how the tidal deformability can be determined in the same framework.

2.2.1 Two-fluid TOV Equations

The TOV equations are a system of coupled differential equations that describe the pressure gradient dp/dr and the mass gradient dm/dr derived from the conservation of the energy stress tensor accounting for the effects of general relativity, assuming a static, spherically symmetric object in hydrostatic equilibrium. The set of two-fluid TOV equations can be obtained by linking the two fluids with a common metric function. This construction neglects direct interactions between the two fluids. The following set of equations are the two-fluid TOV equations written in dimensionless form,[2] [137, 179, 180]

$$\frac{dp_O}{dr} = -(p_O + \varepsilon_O)\frac{d\nu}{dr}, \tag{2.15}$$

$$\frac{dm_O}{dr} = 4\pi r^2 \varepsilon_O, \tag{2.16}$$

$$\frac{dp_D}{dr} = -(p_D + \varepsilon_D)\frac{d\nu}{dr}, \tag{2.17}$$

$$\frac{dm_D}{dr} = 4\pi r^2 \varepsilon_D, \tag{2.18}$$

where the subscript O refers to the fluid of ordinary matter[3] while D stands for dark matter. ε is the energy density. We rescale all dimensionful quantities in units of the mass of the dark matter candidate m_C. In the following, lowercase m and r will refer to the mass and radius during the integration while capital letters M and R refer to neutron star properties. Finally, the metric function $d\nu/dr$ is defined for both fluids as

$$\frac{d\nu}{dr} = \frac{(m_O + m_D) + 4\pi r^3(p_O + p_D)}{r\,(r - 2(m_O + m_D))}. \tag{2.19}$$

The coupled two-fluid TOV equations can be solved using the equations of state of the two fluids. By iterating over the potentially non-identical central pressures, the properties of the neutron star are obtained for each combination of central pressures ($p_{0,O}$ and $p_{0,D}$) by integrating the equations until the pressure vanishes. The radius at which the pressure of ordinary (dark) matter drops to zero within numerical precision is labeled R_O (R_D). We define the maximum radius as $R_{\max} = \max(R_O, R_D)$. M_O/M_D are the integrated masses of the two fluids, respectively, and $M_{\text{tot}} = M_O + M_D$. The solutions can result in a neutron star with a dark core ($R_O > R_D$) or a dark halo ($R_O < R_D$), which potentially also affects the gravitational wave signal of a merger of two neutron stars [145].

Dimensional analysis shows that the mass and radius scale with the constituent mass m_{const} as $1/m_{const}^2$. Given an equation of state that can be trivially scaled by the mass of its constituents m_{const}, as is the case with our dark matter equation of state, halving the mass of the constituents would result in a star with four times the mass and four times the radius. To some extent, this scaling argument is still present in the two-fluid case. A lighter dark matter candidate mass will result in a stronger impact of dark matter on the star. In the limiting cases

---

[2] We generally use natural units in which $\hbar = c = G = 1$.

[3] Sometimes this is also called baryonic matter. We decide to use ordinary (O) as our dark matter is also baryonic.

where $m_C \gg m_n$ or $m_C \ll m_n$, where m_n is the mass of the neutron, this scaling argument is perfectly recovered and heavy dark matter candidate will not alter the properties of neutron stars at all whereas light dark matter candidates will result in a compact object dominated by dark matter that can eventually not be interpreted as a neutron star anymore.

2.2.2 Stability

Not every solution of the TOV equations yields a stable neutron star. Small perturbations in the metric field must settle back to the original solution. By solving a Sturm-Liouville problem one can identify the stable solutions by demanding the following criterion [134, 156, 158]

$$\begin{pmatrix} \delta N_O \\ \delta N_D \end{pmatrix} = \begin{pmatrix} \partial N_O/\partial \varepsilon_{c,O} & \partial N_O/\partial \varepsilon_{c,D} \\ \partial N_D/\partial \varepsilon_{c,O} & \partial N_D/\partial \varepsilon_{c,D} \end{pmatrix} \begin{pmatrix} \delta \varepsilon_{c,O} \\ \delta \varepsilon_{c,D} \end{pmatrix} = 0, \tag{2.20}$$

where $N_{O/D}$ is the total number of ordinary and dark particles and $\varepsilon_{c,O/D}$ is the energy density of ordinary and dark matter in the center of the star. This problem can be translated into demanding that both eigenvalues of the equation in Equation (2.20) must be positive. The number of particles can be calculated simultaneously to the TOV equations via

$$dN = 4\pi \left(1 - \frac{2m}{r}\right)^{-1/2} n r^2 dr. \tag{2.21}$$

For polytropes, the number density n is given by

$$n = \left(\frac{p}{K}\right)^{1/\Gamma}. \tag{2.22}$$

We denote the central pressure at which the star becomes unstable for ordinary and dark matter by $p_{\mathrm{crit},O/D}$, respectively.

2.2.3 Tidal Deformability

When two compact objects orbit each other, they get deformed by the gravitational tidal field of one another. The tidal deformability λ is a quantity that describes the proportionality between the external tidal field E_{ij} and the induced quadrupole deformation Q_{ij} [181].

$$Q_{ij} = -\lambda E_{ij} \tag{2.23}$$

We will work with the dimensionless version of the tidal deformability that is connected to the dimensional tidal deformability λ and the dimensionless second Love number k_2 via

$$\Lambda = \frac{\lambda}{M_{\text{tot}}^5} = \frac{2}{3}\frac{k_2}{C^5}. \tag{2.24}$$

Here, we have introduced the compactness $C = M_{\text{tot}}/R_{\text{max}}$ calculated with the total mass M_{tot} and the maximum radius R_{max}. Calculating the tidal deformability from Equation (2.23) requires the second Love number, which can be calculated from the neutron star compactness as [181, 182]

$$\begin{aligned} k_2 = &\frac{8C^5}{5}\left(1-2C\right)^2\left[2+2C(y-1)-y\right] \times \\ &\{2C\left[6-3y+3C(5y-8)\right]+ \\ &4C^3\left[13-11y+C(3y-2)+2C^2(1+y)\right]+ \\ &3\left(1-2C\right)^2\left[2-y+2C(y-1)\right]\ln(1-2C)\big\}^{-1}. \end{aligned} \tag{2.25}$$

The auxiliary parameter y can be integrated simultaneously with the TOV equations by [183]

$$r\frac{dy(r)}{dr} + y(r)^2 + y(r)F(r) + r^2 Q(r) = 0, \tag{2.26}$$

where

$$F(r) = \frac{r - 4\pi r^3((\varepsilon_O + \epsilon_D) - (p_B + p_D))}{r - 2m}, \tag{2.27}$$

and

$$\begin{aligned} Q(r) = &\frac{4\pi r\left(5(\varepsilon_O+\varepsilon_D)+9(p_O+p_D)+\frac{\varepsilon_O+p_O}{c_{s,O}^2}+\frac{\varepsilon_D+p_D}{c_{s,D}^2}-\frac{6}{4\pi r^2}\right)}{r-2m} \\ &-4\left[\frac{m+4\pi r^3(p_O+p_D)}{r^2(1-\frac{2m}{r})}\right]^2, \end{aligned} \tag{2.28}$$

with $m = m_O + m_D$ and $c_{s,O/D}^2 = dp_{O/D}/d\varepsilon_{O/D}$ is the speed of sound [156]. The starting condition for y in the center of the star is $y(r=0) = 2$. In contrast to black holes, neutron stars have a non-vanishing tidal deformability. As a result, the gravitational wave signal of a neutron star binary differs from the one produced by a black hole merger by a potentially time-dependent phase in the late stages of the merger. In leading order in the tidal deformabilities of the two neutron stars, this phase can be determined by the parameter $\tilde{\Lambda}$ as [184]

$$\tilde{\Lambda} = \frac{16}{13} \frac{(M_1 + 12M_2)M_1^4\Lambda_1 + (M_2 + 12M_1)M_2^4\Lambda_2}{(M_1 + M_2)^5}, \tag{2.29}$$

where Λ_1 and Λ_2 are the tidal deformabilities and M_1 and M_2 are the total masses of the two neutron stars. Thus, deviations of this quantity compared to a neutron star made of ordinary matter provide information about the influence of a dark matter component on the gravitational wave signal of two compact stellar objects. The applicability of gravitational wave analysis beyond black-hole mergers to more complex and exotic systems such as the mergers of mixed stars studied here is not yet thoroughly understood [185–188]. An indication of dark matter in neutron stars would be the occurrence of a secondary peak in the gravitational wave signal.

2.3 Results

The results of this chapter have been published in [164] and we will discuss the findings for a slightly different set of parameters. We have investigated three different ordinary matter equations of state that represent limiting cases together with the dark matter equation of state of one flavor G_2 QCD at different quark masses labeled light and heavy. They correspond to the candidate for dark matter having a mass of four times and three times the mass of the dark pion, respectively. We employ different masses of the dark matter candidate of $m_C = \{0.5, 1, 2, 4\}$ GeV. In general, the effect of the addition of dark matter is similar to previous work on mixed neutron stars. We expect maximal mixing effects when the scales of the two systems are comparable, which is the case when $m_C = 1\,\mathrm{GeV} \approx m_n$. The effects of the light and heavy dark matter equations of state are very similar, while the different masses of dark matter have a major impact, which can be traced back to the overall scaling argument. In Figure 3, we show the range of central pressures of ordinary and dark matter employed. We showcase our results using the dark matter equation of state from the light ensemble and use EoS II for ordinary matter. The results for the remaining equations of state can be found in Appendix C. Only solutions that meet the stability criterion of Equation (2.20) are shown. Gray points have a dark matter mass fraction of $M_D/M_O > 10\%$, which we do not consider to be neutron stars at all. The color indicates the mass fraction, and the orange points specifically show solutions with $M_D/M_O < 1\%$. By that choice, we want to ensure that these objects can actually be identified as neutron stars. These solutions do not spread widely and largely follow the result

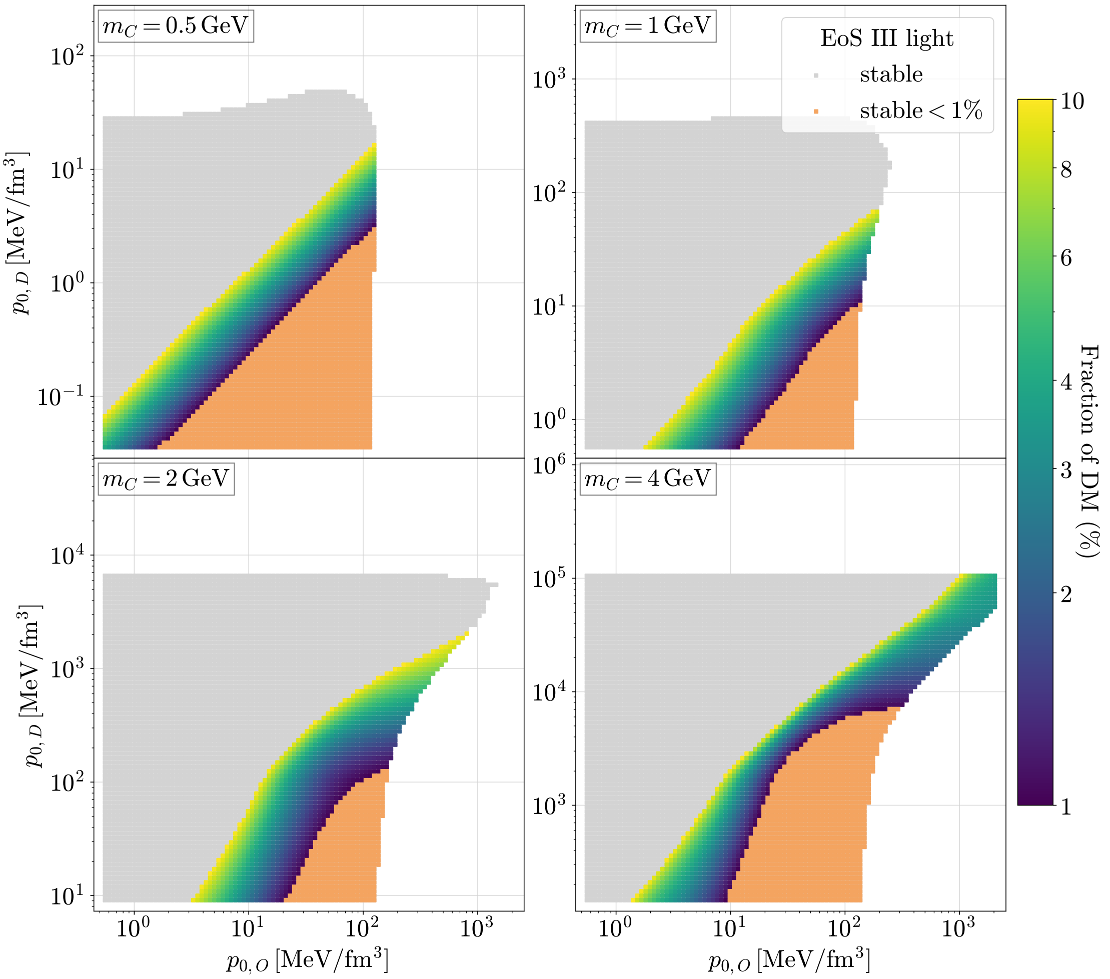

Figure 3: The investigated set of central pressures of ordinary matter $p_{0,O}$ and dark matter $p_{0,D}$. We showcase our results using the dark matter equation of state from the light ensemble and use EoS II for ordinary matter. The gray area indicates stable solutions with $M_\mathrm{D}/M_\mathrm{O} > 10\%$. The color scale indicates the mass fraction $M_\mathrm{D}/M_\mathrm{O}$ of the resulting star limited to 10% and orange points specifically show stars with $< 1\%$. We use the same color-scheme for all following plots of this chapter. The four panels show results for four different masses of the dark matter candidate $m_C = \{0.5,\, 1,\, 2,\, 4\}\,\mathrm{GeV}$. We see that the addition of dark matter can result in stable solutions at central pressures larger than $p_{\mathrm{crit},O/D}$.

of a pure neutron star.

The addition of dark matter to neutron stars leads to additional pressure, resulting in a larger pressure gradient for both fluids. One consequence is that the equation of state is traversed more quickly, shifting the critical central pressure to larger values. The critical pressure in the case of pure ordinary matter coincides

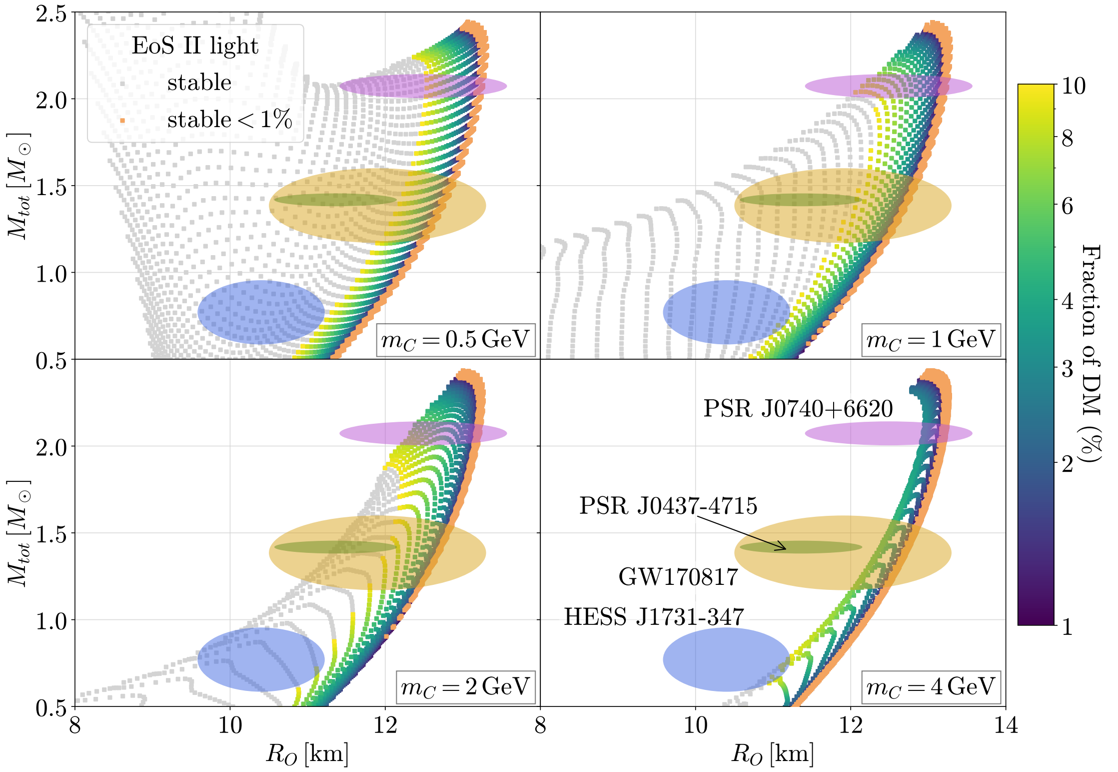

Figure 4: The mass-radius relations between and the total observable mass $M_O + M_D$ in $M_\odot$ and the observable ordinary matter radius R_O in km for the same equations of state and masses m_C. We use the same color-coding as in Figure 3. The ellipses show results for the mass and radius of various neutron stars, which were determined using different techniques [184, 189–191].

with the right edge at low dark matter pressures in Figure 3 best seen in the case of $m_C = 0.5\,\mathrm{GeV}$. Going to $m_C = 4$ GeV shows additional stable solutions at pressures greater than $p_{\mathrm{crit},O}$. Equivalently, the upper edge at low ordinary-matter central pressures at $m_C = 4\,\mathrm{GeV}$ shows the critical pressure of the pure dark star. Note that this pressure scales as $\sim m_C^4$. Again, we see that central pressures larger than $p_{\mathrm{crit},D}$, especially in the case of $m_C = 0.5\,\mathrm{GeV}$, yield stable solutions. These cases are basically dark stars with admixed Standard Model matter. We can see that this occurs even if the dark matter fraction is restricted to $< 1\%$, which is particularly interesting because it grants access to new regimes of equations of state that could potentially have interesting phenomenology.

In Figure 4, we show a set of mass-radius relations from the two-fluid TOV equation in the same color-coding and for the same equations of state as before. For comparison, we include representative results [192] on the mass and radius of the *strangely light neutron star* HESS J1731-347 [189], the heavy pulsar PSR J0740+6620 [190], the pulsar PSR J0437-4715 [191] and the first neutron star merger detected with gravitational waves GW170817 [184] as ellipses. We plot here the total mass against the radius of ordinary matter. This is because ordinary radius measurements rely on electromagnetic radiation and a potential dark matter halo is invisible to telescopes.

For low dark matter candidate masses, dark matter forms a halo. At low central pressures, this halo is large, but its mass contributes little to the total mass. However, the additional pressure still leads to a greater pressure gradient, which in turn results in a smaller neutron star core. Since the core is the densest part of the neutron star, this results in a lower total mass, which we can see in the mass-radius relation for $m_C = 0.5$ and $1\,\mathrm{GeV}$, where the additional dark matter consistently lowers the mass and radius at large central pressures. For the restriction to 1% dark matter, the effect is on the percentage level, but for larger dark matter fractions, the radius may decrease by up to $1\,\mathrm{km}$ and the mass by up to $0.2\,M_\odot$. Even though the two fluids do not interact directly, the radius of ordinary matter is sensitive to the addition of dark matter. For large dark matter candidate masses, the dark matter forms a dark core. In this case, an increase in the central pressure of the dark matter leads to a larger total mass up to a critical point, beyond which the additional pressure reduces the size of both cores and thus reduces the total mass. We can see this in the mass-radius relation for $m_C = 2$ and $4\,\mathrm{GeV}$, where the addition of dark matter increases the total mass at first, but decreases it after a critical point. For $m_C = 4\,\mathrm{Gev}$, the mixed stars closely mimic the pure ordinary matter solution.

Not shown here is that the two-fluid TOV equations for light dark matter masses can also result in massive dark matter-dominated objects. Although these do not resemble neutron stars, they could provide an explanation for non-standard objects. An astrophysical observation of exotic compact objects also in gravitational wave experiments would motivate a more comprehensive analysis of these objects. Whether or not the results are consistent with the data depends mainly on the ordinary matter equation of state employed (see Appendix C), and the current data are not sensitive enough to distinguish between neutron stars and mixed stars.

Gravitational wave detection is more promising for the identification of mixed stars, especially because dark cores and halos can provide a supplementary peak in the data. This has been shown in simulations of binary neutron star events [129]. Our data cannot provide the dynamical information required for this investigation,

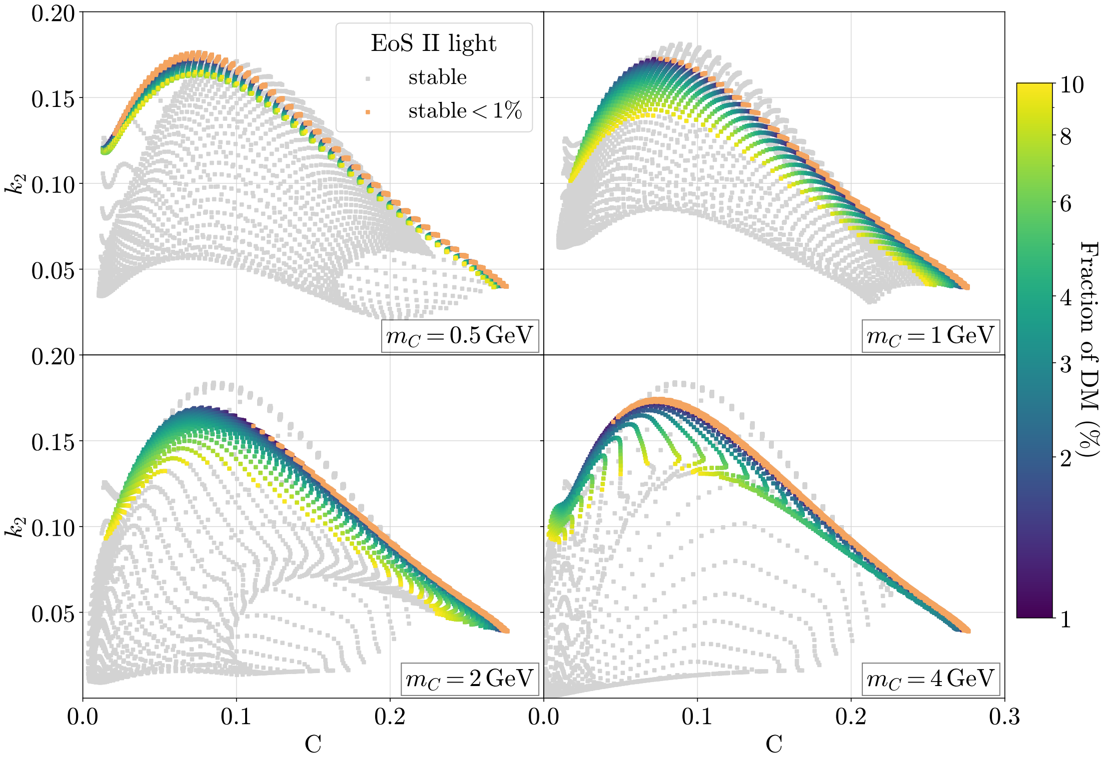

Figure 5: The second Love number k_2 plotted against the compactness obtained with the outermost radius $C = M_{\mathrm{tot}}/R_{\mathrm{max}}$ for the same equations of state and masses m_C. We use the same color-coding as in Figure 3.

but we can investigate the effect of dark matter on the tidal deformability, which is shown in Figure 5. We show the second Love number k_2, which is related to the tidal deformability by Equation (2.24) against the compactness $C = M_{\mathrm{tot}}/R_{\mathrm{max}}$, which depends on the outermost radius of the mixed star. For this reason, a direct comparison with the results for pure neutron stars is only valid if the two radii are similar. We see that the addition of dark matter lowers both k_2 and the compactness. The effect is strongest in the case of $m_C = 1\,\mathrm{GeV}$. For up to 10% dark matter k_2 can decrease by up to 0.05. Employing larger dark matter fractions shown in the gray points can result in objects with compactnesses ~ 0.2 at values of $k_2 \approx 0.03$, which is much smaller than ordinary neutron stars. However, these objects had to be classified as exotic objects that do not resemble neutron stars.

In summary, the addition of dark matter even when kept at 1% can have sizable effects on the macroscopic parameters of the neutron star, such as mass, radius, and tidal deformability. Of particular interest is the possibility of using higher central pressures in the ordinary matter equation of state. The effects described above are fairly standard for various dark matter equations of state and we do not see any effects that can be traced back to the non-perturbative nature of the dark matter equation employed. Nevertheless, this study confirms that SIMP-like dark matter can also lead to mixed stars. Similarly to different works, we find a variety of solutions when the dark matter mass fraction is allowed to take large values. These objects do not resemble neutron stars but could explain a hypothetical exotic star.

Chapter 3

Scattering of Dark Pions in Sp(4) Gauge Theory

SIMP models are attractive alternative dark matter candidates, but given their UV-completeness, a proper description of their dynamics relies on non-perturbative methods. Lattice field theory is an excellent tool for investigating non-perturbative effects and in the best case to also support perturbative calculations by providing the necessary LECs. In addition to the particle spectrum, scattering properties are important for the phenomenology of SIMP models. This chapter discusses how to obtain scattering properties from the lattice. We investigated two different scattering channels that both have strong phenomenological motivation. We start with an introduction to general scattering theory in Section 3.1 followed by an introduction to the flavor symmetry in Section 3.2. Afterwards, in Section 3.3 we discuss the techniques used to arrive at the results presented in Section 3.4. Finally, we give an overview of the necessary steps to investigate the model-motivating three-to-two scattering in Section 3.5.

3.1 Scattering Theory

Experimental results related to scattering are often given as cross sections, which describe processes from ingoing states $|i\rangle$ to outgoing states $\langle f|$. We will consider a process like $P_1 + P_2 \to X \to P_1' + P_2'$, where X could be any intermediate state that will be fully described by the so-called S-*matrix.* The cross section is often interpreted as a probability, but it has units of area which can be understood as an effective two-dimensional size of the states, where if the two areas overlap, the scattering process will occur. We can infer this by considering the probability of a scattering process.

$$P = \frac{|\langle f|i\rangle|^2}{\langle f|f\rangle\langle i|i\rangle} \tag{3.1}$$

We get the rate $\dot{P}$ by dividing by the time in which the process happens ΔT. If we consider a flux of ingoing particles $\Phi = nv$ in z-direction, we can define the cross section as

$$\sigma = \frac{\dot{P}}{\Phi} = \frac{P}{Tnv}, \tag{3.2}$$

where $n = 1/(A\Delta z)$ and $v = \Delta z/\Delta T$ are the number density and velocity of the incoming particles. A is the area in the x- and y- direction that gives rise to the units of the cross section.

3.1.1 Partial-wave Cross Section

In particle physics, due to the angular dependence of the processes, we are usually interested in the differential cross section which is related to the total cross section via

$$\sigma_{\text{tot}} = \int \frac{d\sigma}{d\Omega} d\Omega, \tag{3.3}$$

where $d\Omega = \sin\theta\, d\theta\, d\phi$ is the solid angle element. One powerful tool in scattering is the expansion in partial waves. The underlying scattering functions are decomposed into partial waves, in which all angular dependence is captured in different moments of the angular momentum l. Once this is done, the formalism, for example, to obtain the cross section simplifies dramatically. The differential cross section is related to the scattering matrix $\mathcal{M}$ by

$$\frac{d\sigma}{d\Omega} = \frac{1}{64\pi^2 s}|\mathcal{M}|^2, \tag{3.4}$$

which in turn is related to the scattering amplitude f_l via

$$\mathcal{M} = 32\pi \sum_{l}^{\infty} (2l+1) f_l(s) P_l(\cos\theta), \tag{3.5}$$

where P_l are the Legendre polynomials and $s = 4(p^2 + m^2)$ is the center-of-mass energy of two scattering particles with equal mass and back-to-back momentum p. At this point, we also introduce the S-matrix, as well as the transition matrix

t_l and the phase shift δ_l.

$$S_l = e^{2i\,\delta_l} = 1 + 2i\,t_l \tag{3.6}$$

$$t_l = e^{i\delta_l}\sin\delta_l = (\cot(\delta_l) - i)^{-1} \tag{3.7}$$

$$f_l = \frac{\sqrt{s}}{2p}t_l \tag{3.8}$$

The S-matrix describes all properties of the intermediate state X. The transition matrix and phase shift are directly related to this quantity, and a description with either of these quantities is equally valid. Because Legendre polynomials of different orders are orthogonal, different partial waves do not mix, and we can define the total cross section in terms of the phase shift as

$$\begin{aligned}\sigma_{\text{tot}} &= \frac{4}{s}\int |(2l+1)f_l(s)P_l(\cos\theta)|^2 d\Omega,\\ &= \frac{1}{p^2}\int |(2l+1)t_l(s)P_l(\cos\theta)|^2 d\Omega,\\ &= \frac{1}{p^2}\int_0^{2\pi} d\phi \int_{-1}^{1}\sum_l\sum_{l'}(2l+1)(2l'+1)e^{i\delta_l}e^{-i\delta_{l'}}\sin(\delta_l)\sin(\delta_{l'})P_l(x)P_{l'}(x)dx,\\ &= \frac{4\pi}{p^2}\sum_l(2l+1)\sin^2(\delta_l),\end{aligned} \tag{3.9}$$

where in the second step we have used orthogonality relation of the Legendre polynomials,

$$\int_{-1}^{1} P_l(x)P_{l'}(x)dx = \frac{2}{2l+1}\delta_{ll'}, \tag{3.10}$$

which prevents the mixing of different partial waves via the Kronecker delta. Now we may define the partial-wave cross section σ_l.

$$\sigma_l = (2l+1)\frac{4\pi}{p^2}\sin^2(\delta_l) \tag{3.11}$$

$$\sigma_{\text{tot}} = \sum_l \sigma_l \tag{3.12}$$

3.1.2 Scattering Parameterizations

The intermediate state X may be a scattering state, a resonance, or a bound state. In order to understand the effect of these objects, we have to understand the analytic structure of the partial-wave amplitude. The partial-wave amplitude f_l is a function that may have cuts and poles. For $s \geq 4m^2$, two-particle states can be produced, and unitarity requires an imaginary part. Due to the hermitian analyticity of the partial-wave amplitude $f_l(s^*) = f_l^*(s)$, this induces a cut along the real axis. As a consequence, the function becomes multivalued on different Riemann sheets which are connected by the real axis below threshold. Bound states are poles of the function with real values of $s < 4m^2$ that lie on the first sheet called *physical*. Resonances lie above the elastic threshold in the complex plane on the second *unphysical* sheet. Their location in the complex plane determines their physical properties. The real part can be identified with the *resonance position* while the imaginary part can be related to the *resonance width*.

The different natures of the intermediate state X can be described by different parameterizations for the phase shift. By fitting the data to a corresponding function, additional observables such as the *scattering length* or resonance parameters can be extracted. Universally, *effective range expansion* (ERE) describes the behavior of the phase shift close to the elastic threshold. The phase shift in the vicinity of a resonance can be described by a *Breit-Wigner* shape. Depending on the physics of the ensembles employed, we fit the phase shift data with the respective function. For an arbitrary partial wave l, ERE is an expansion in order of p^2 given by

$$p^{2l+1}\cot(\delta_l) = -\frac{1}{a_l^{2l+1}} + \frac{p^2}{2r_l^{2l-1}} + \mathcal{O}(p^4), \tag{3.13}$$

where a_l is the scattering length and r_l is the *effective range*. We may use $\sin(\arctan(x)) = x\left(x^2+1\right)^{-1/2}$ to convert these two parameters to a cross section that holds for small momenta.

$$\sigma_{\mathrm{ERE},l} = \frac{4\pi(2l+1)p^{4l}}{\left(\frac{1}{2}p^2 r_l^{1-2l} - a_l^{-2l-1}\right)^2 + p^{4l+2}} \tag{3.14}$$

We will use this ERE for scattering in s- and p-wave $(l = 0, 1)$. In these two cases and up to order $\mathcal{O}(p^2)$ the cross section will simplify to

$$\sigma_0 = \frac{4\pi}{\left(\frac{p^2 r_0}{2} - \frac{1}{a_0}\right)^2 + p^2} \overset{p\to 0}{=} 4\pi a_0 \tag{3.15}$$

$$\sigma_1 = \frac{12\pi p^4}{\left(\frac{p^2}{2r} - \frac{1}{a^3}\right)^2 + p^6} \overset{p\to 0}{=} 0. \tag{3.16}$$

In the limit of $p \to 0$ and with a finite scattering length, the cross section in any partial wave with $l \geq 1$ will vanish. ChPT also predicts scattering properties based on flavor symmetry. Although in general these predictions will involve LECs, some are independent of those which includes the scattering length in the maximal two-pion scattering channel. In [193] you can find these predictions as a function of the value of m_π/f_π, which can be used to estimate how far away from the chiral limit you are. In general, ChPT will work better the closer you are to the chiral limit and considers pion scattering only which is well motivated close to the chiral limit. Farther away from the chiral limit, one also has to consider the other mesons in the theory like the vector meson. Lattice calculations are generally numerically cheaper farther away from the chiral limit. In our simulations, we work in a regime where the vector meson is relevant.

In [193], the ERE is not performed on the phase shift but instead on the scattering amplitude. Both quantities can be expanded in orders of p^2, but the expansions must be adequately related to each other. We are only interested in the scattering length for which this relation is straightforward, but the definitions above do not coincide with [193]. We will work with the convention in which the s-wave cross section at threshold will be $\sigma = 4\pi a_0^2$. For the 14-dimensional channel, the ChPT prediction reads

$$a_0^{\mathbf{14}} = \frac{1}{16\pi}\left(\frac{m_\pi}{f_\pi}\right)^2. \tag{3.17}$$

In the ten-dimensional channel, we expect a resonance. For that reason, we describe the phase shift data using a Breit-Wigner form [194]. The phase shift can be expressed in terms of the *resonance position* m_R and the *resonance width* $\Gamma(s)$ as

$$\cot(\delta_l) = \frac{m_R^2 - s}{\sqrt{s}\,\Gamma(s)}, \tag{3.18}$$

$\Gamma(s)$ can further be related to the coupling $g_{\rho\pi\pi}$ introduced in Section 1.2.4

$$\Gamma(s) = \frac{g_{\rho\pi\pi}^2}{6\pi}\frac{p^3}{s}. \tag{3.19}$$

The Breit-Wigner form can be modified with *Blatt-Weisskopf barrier factors* which introduce the *radius of the centrifugal barrier* r_0 as a third fitting parameter.

$$\Gamma(s) = \frac{g_{\rho\pi\pi}^2}{6\pi}\frac{p^3}{s}\frac{1+(p_R r_0)^2}{1+(p r_0)^2} \tag{3.20}$$

Here, $p_R = \sqrt{m_R^2 - 4m_\pi^2}/2$ is the scattering momentum at the resonance position.

3.1.3 Velocity-weighted Cross Section

In dark matter phenomenology, the low-energy cross section which is dominated by the scattering length is of particular interest. Recently, the *velocity-weighted cross section* has been investigated by fitting dark matter halo shapes [46]. This quantity is not measurements directly, but is based on the results of simulations that rely on assumptions about the dynamics of matter on galactic scales. Nevertheless, it is interesting to examine this quantity in our theory, especially since it can be calculated directly from the lattice data. This illustrates a direct comparison between fully non-perturbative lattice results and astronomical observations. The velocity-weighted cross section is defined as

$$\langle \sigma v \rangle = \int_0^{v_{esc}} v\,\sigma(v)\,f(v,\langle v \rangle)\,dv, \tag{3.21}$$

$$f(v) = \frac{32v^2}{\pi^2 \langle v \rangle^3} \exp\left(-\frac{4v^2}{\pi \langle v \rangle^2}\right). \tag{3.22}$$

Here, $v = \sqrt{(s-4m_\pi^2)/(s-3m_\pi^2)}$ is the relative velocity in units of c between two dark matter particles which we describe by a Maxwell-Boltzmann distribution $f(v)$ with mean relative velocity $\langle v \rangle$. The distribution of the relative velocity follows directly from the assumption that the dark matter velocity follows a Maxwell-Boltzmann distribution. v_{esc} is the escape velocity that we assume to be much larger than $\langle v \rangle$. $\langle \sigma v \rangle$ is Boltzmann-suppressed at larger relative velocities. Therefore, it is dominated by the low-energy behavior of the cross section. $\sigma(v)$ is the total cross section, which includes all partial waves but higher partial waves are suppressed at low energies.

3.2 Sp(4) Flavor Symmetry

The defining feature of this work is the pseudo-real nature of the fundamental representation of $Sp(4)_c$. In Section 1.2.3, we saw that after chiral symmetry breaking, the theory is described by an $Sp(2N_f)$ flavor symmetry. In this section, we deepen our understanding of flavor symmetry in the case $N_f = 2$ using a familiar picture in which we obtain the equivalent of the meson octet in QCD. We will work with states in different flavor multiplets which are defined by *irreducible representations* (irreps). Group transformations act on a vector space through a representation. A representation is said to be irreducible if the vector space it acts on does not contain any proper subspaces left invariant under the action of all group elements through the representation. Combinations of flavor multiplets in general project into different irreps given by the decomposition of the tensor products of the respective irreps. Therefore we will consider all tensor products of the irreps of $Sp(4)$ relevant to this work, from which we obtain the possible combinations of quarks that constitute the particle and scattering states. We will work with flavor quantum numbers which are strictly speaking given by the label of the irrep and the weights of the states therein. However, we will also mention emergent quantities such as strangeness or charge.

3.2.1 Flavor Quantum Numbers and the Tenfold Way

Similar to isospin in $SU(2)$ or strangeness and charge in $SU(3)$, $Sp(4)$ has its own flavor quantum numbers. Equivalently to $SU(3)$, $Sp(4)$ is a rank two group and the states within an irrep can therefore be described by a combination of two quantum numbers. In reality $SU(3)$ is only an approximate symmetry, which is the reason why you can assign its quantum numbers a physical meaning.[1] In this work we work with mass-degenerate fermions and the $Sp(4)$ flavor symmetry remains intact. Consequently, it is unnecessary to assign any physical meaning to these quantum numbers, and we will refrain from doing so. Nevertheless, it is helpful to review the flavor states that arise in the theory and how they sometimes resemble and sometimes differ from $SU(3)$.

In the following, we will construct the equivalence of the *eightfold way* in our theory. The eightfold way orders the eight pNGBs from a hypothetical intact $SU(3)$ symmetry. The underlying question is which states can be built in the theory from the perspective of the global flavor symmetry. We will only consider the mesonic part of QCD, as we do not have a counterpart of the baryon decuplet in our theory. The starting point is the flavor multiplet of the fundamental fermions. In $SU(3)$ flavor symmetry, the fundamental representation is complex and 3-dimensional, which means that there are two conjugate charge assignments $\mathbf{3}$ and $\bar{\mathbf{3}}$.[2] To construct a meson state, a fermion and an antifermion must be combined, which translates into the following tensor product.

$$\mathbf{3} \otimes \bar{\mathbf{3}} = \mathbf{1} \oplus \mathbf{8} \tag{3.23}$$

The decomposition into an eight- and a one-dimensional irrep on the right-hand

---

[1] A real $SU(3)$ symmetry would be realized if the masses of the three light quarks would be identical $m_u = m_d = m_s$.

[2] We will name the irreps by their dimensionality, which will be unambiguous for the irreps presented here.

Table 1: The fundamental fermions of $SU(3)$ with their weights, strangeness, charge, and the values of Q_1 and Q_2 used in Figure 6. Antiquarks carry the negatives of these values.

Quark	w_1	w_2	Charge	Strangeness	Q_1	Q_2
u	1	0	1/3	0	1/3	0
d	-1	1	$-2/3$	0	$-2/3$	0
s	0	-1	$-2/3$	-1	$-1/6$	$-\sqrt{3}/2$

Table 2: The fundamental fermions of $Sp(4)$ with their weights and the values of Q_1 and Q_2 used in Figure 6. Ψ_1 is neighboring Ψ_2 and Ψ_4 while being opposite of Ψ_3. Antiquark would carry negative values but this results in the same quadruplet.

Quark	w_1	w_2	Q_1	Q_2
Ψ_1	1	0	1/2	1/2
Ψ_2	-1	1	1/2	-1/2
Ψ_3	1	-1	-1/2	1/2
Ψ_4	-1	0	-1/2	-1/2

side shows us that a quark and an antiquark can form a flavor singlet and a flavor octet. The singlet can be identified as the η', while the meson octet consists of the η, the three pions, and the four kaons. In Table 1, we provide the weights, strangeness, and charge of the $SU(3)$ triplet. We further assign alternative quantities Q_1 and Q_2, which will result in the well-known hexagonal shape of the meson octet. We can perform the tensor product of Equation (3.23) graphically by displacing the weights of the second factor onto each of the weights of the first factor. This is shown in Figure 6. Here, we can identify horizontal lines as lines with constant strangeness. Additionally, the line spanned by the K^- and π^- as well as lines parallel to that indicate constant charge. We can also identify three triplets that span $SU(2)$ subgroups and correspond to the case in which one of the quarks is not degenerate. One of them is the pion triplet which approximates physics well, as the masses of the light quarks are almost degenerate while the strange quark is quite a bit heavier.

In the case of $Sp(4)$, there is no physical meaning in the different weights within an irrep, since the quarks in our theory are degenerate in mass, leaving the symmetry intact. You may introduce a breaking of the symmetry, in which case it would be sensible to assign them a physical meaning, but we will not discuss this possibility in this thesis. Instead, we assign the fundamental quadruplet the two quantities Q_1 and Q_2 – see Table 2. This assignment will result in the most intuitive graphical representation. In Table 2, we can also see that the quadruplet

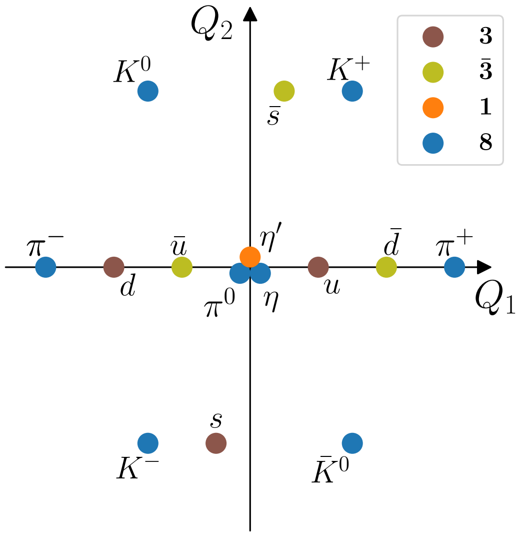

Figure 6: The eightfold way from QCD obtained by assigning the fundamental fermions of $SU(3)$ the quantities Q_1 and Q_2 from Table 1. Brown (yellow) points are the fundamental (anti-)fermions. The orange point is the flavor singlet and the blue points are the meson octet.

is recovered when you take the negative values. This is in contrast to $SU(3)$ where the negatives are the charges of the antiparticles. This means that the fundamental quadruplet contains its own antiparticles and that $Sp(4)$ does not have conjugate charge assignments like $SU(3)$. From here on, we may investigate which meson states can be built from the quark quadruplet. States made of two quarks may live in one of the irreps given by the tensor product

$$\mathbf{4} \otimes \mathbf{4} = \mathbf{1} \oplus \mathbf{5} \oplus \mathbf{10}. \tag{3.24}$$

The first difference from QCD is that there are three irreps occurring in this decomposition. As a result, mesonic multiplets in $Sp(4)$ can live in one of these three irreps, and we will see that the pseudoscalar pions form a quintuplet, while the vector mesons form a decuplet. We can display this tensor product diagrammatically in a similar way to $SU(3)$ to obtain the *tenfold way*. This is shown on the left side of Figure 7. The **1**, the **5**, and the **10** form four copies of the quadruplet around each of its points. Notice how the resulting shapes of the multiplets is the only symmetric way of assembling a singlet, a quintuplet, and a decuplet. Another important difference between $Sp(4)$ and $SU(3)$ is that each of the states in the fundamental multiplet has an *opposite* state. For Ψ_1 this is Ψ_3 and for Ψ_2 this is Ψ_4. The other states are *neighboring* states. In building the quintuplet, the

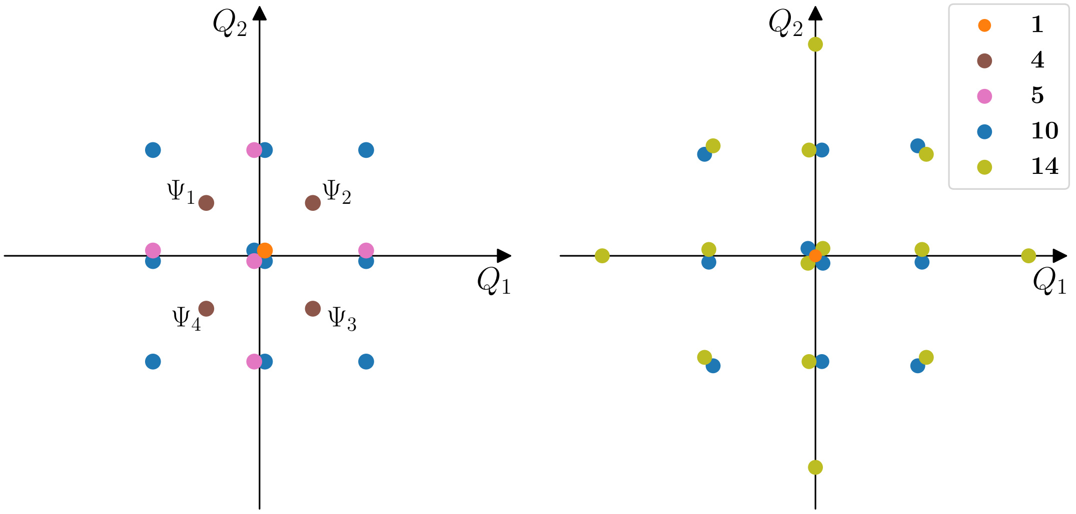

Figure 7: The tenfold way in $Sp(4)$ obtained by assigning the fundamental fermions the quantities Q_1 and Q_2 from Table 2. Left panel: The decomposition of the tensor product from Equation (3.24). Brown points are the fundamental fermions where you can see that there are neighboring and opposing states. Pink points are the quintuplet and blue points the decuplet. Right panel: The decomposition of the tensor product from Equation (3.25). Yellow points are the 14-plet.

four outer states are obtained by combining neighboring states, whereas the center point is built by combining the states opposite to each other. In the construction of the decuplet, the outermost points are obtained by combining the indices with themselves, the points on the axes are again obtained by combining neighboring points, and the two center points are combinations of opposing states.

3.2.2 Scattering States

In the same way that we have decomposed the tensor products of two fundamental representations to find the meson states, we can investigate the decomposition of the tensor products of meson multiplets to find which irreps contain composite states of mesons. Depending on the underlying dynamics, the resulting multiplets might manifest as bound states, resonances, or scattering states. In this theory, just as in QCD, the flavor quantum numbers remain unchanged during scattering processes. For this reason processes can only happen between states states that share the same multiplet. In this work, we are interested in pion scattering and the relevant tensor product is

$$\mathbf{5} \otimes \mathbf{5} = \mathbf{1} \oplus \mathbf{10} \oplus \mathbf{14}. \tag{3.25}$$

We find a 14-plet and again a decuplet and a singlet, which are depicted in the right panel of Figure 7. The outermost points are the maximum weight configurations which are attractive for the construction of operators as they are unique to their irrep, the **14** in this case. Although a one-to-one mapping between the pion scattering channels in $Sp(4)$ and $SU(2)$ is not possible, it can be helpful to make a connection to the pion scattering channels of QCD. Like in QCD, there is a singlet scattering channel, and pions can scatter with the flavor singlet meson in this channel. The largest scattering channel is the 14-dimensional which contains the maximum weight configurations of two pions like $\pi^A\pi^A$ in QCD. By naive counting, most of the pion scattering will occur in this channel, which makes it interesting for dark matter phenomenology. The lattice results for the scattering properties of this channel will be discussed in Section 3.4.1. Last but not least, there is the ten-dimensional channel, which shares the multiplet with the vector mesons. For this reason, the process $\rho \to \pi\pi$ takes place in this channel, making it the equivalent of the *isospin-1* channel in QCD. We present results for $Sp(4)_c$ in Section 3.4.2. All channels have been investigated in two-color QCD [107, 114–117]. The ten-dimensional channel also contains the model-motivating three-to-two process. This can be seen by considering the tensor product of three quintuplets.

$$\begin{aligned}\mathbf{5}\otimes\mathbf{5}\otimes\mathbf{5} &= (\mathbf{1}\oplus\mathbf{10}\oplus\mathbf{14})\otimes\mathbf{5} && (3.26)\\ &= \mathbf{5}\oplus(\mathbf{5}\oplus\mathbf{10}\oplus\mathbf{30})\oplus(\mathbf{5}\oplus\mathbf{30}\oplus\mathbf{35}) && (3.27)\\ &= 3\cdot\mathbf{5}\oplus\mathbf{10}\oplus 2\cdot\mathbf{30}\oplus\mathbf{35} && (3.28)\end{aligned}$$

The second line shows the individual tensor products of $\mathbf{5}\otimes\mathbf{5}$ with the third quintuplet. The ten-dimensional channel is the only one shared by two-pion and three-pion scattering. Significantly, a three-pion state in the ten-dimensional channel can only be constructed by combining a two-pion state in the **10** with a third pion. Although the three-to-two process is likely to have a larger contribution at energies closer to the three-pion threshold, it will be interesting to check whether there is any effect related to this process. A proper analysis of the three-to-two process requires the use of the three-particle quantization condition [195–198] which we will introduce in Section 3.5. Lastly, you can also build a scattering channel in the **10** from a $\rho\pi$ state, as can be seen by decomposing the following tensor product.

$$\mathbf{5}\otimes\mathbf{10} = \mathbf{5}\oplus\mathbf{10}\oplus\mathbf{35} \qquad (3.29)$$

3.2.3 Operator Construction

In order to perform calculations on the lattice, we will need the specific form of the operators. A peculiarity of this theory is that the flavor eigenstates are not eigenstates of *ordinary parity* P. More precisely, the additional pNGBs that arise from the larger flavor symmetry have positive parity, in contrast to the Standard Model pions. We may circumvent this issue by redefining parity transformations P with an additional phase factor [85, 199].

$$D : \psi(\vec{x}, t) \to \pm i P \psi(\vec{x}, t) P^{-1} = \pm i \gamma_4 \psi(-\vec{x}, t) \tag{3.30}$$

The extra phase cancels in all Standard Model-like operators and is also a symmetry of the Lagrangian. All particles in a flavor multiplet share the same D-parity. Therefore, the operators are specified by J^D and their flavor quantum number which is defined by the irrep. In order to construct operators of certain flavor quantum numbers, we start from the fundamental quadruplet, which for $N_f = 2$ and written as Dirac spinors, where the charge conjugation matrix is C, takes the form

$$\Psi = \begin{pmatrix} P_L u \\ P_L d \\ C\Sigma P_L \bar{u}^T \\ C\Sigma P_L \bar{d}^T \end{pmatrix}, \quad \bar{\Psi} = \begin{pmatrix} P_R \bar{u}^T \\ P_R \bar{d}^T \\ C\Sigma P_R u \\ C\Sigma P_R d \end{pmatrix}^T, \tag{3.31}$$

where we have introduced two flavors, u and d, analogous to QCD. Let us first consider the case of building hadrons from two quarks. In general, the construction of operators works by connecting the color, Dirac, and flavor indices in a specific way. Physical states have to be color singlets that can be built using the color matrix Σ. The connection of flavor indices is done with matrices acting in flavor space which entail the projection into the desired irrep dictated by the $Sp(4)$ flavor symmetry. Finally, J^D is given by the gamma structure Γ that connects the Dirac indices. For example, $\Gamma = \mathbb{1}$ gives a scalar with $J^D = 0^+$, $\Gamma = \gamma_5$ gives us a pseudo-scalar with $J^D = 0^-$, and $\Gamma = \gamma_i$ gives us a vector with $J^D = 1^-$. Whether a multiplet with certain J^D is realized in the theory depends on whether you can build an operator with the respective gamma structure given the contraction of flavor indices that result in this multiplet. The construction of states that transform under a specific J^D is not as straightforward as in QCD, because we need to construct bilinears from the more sophisticated flavor quadruplet Ψ. In order to build a scalar operator, for example, we have to obtain the bilinear $\bar{\psi}\psi$. For this, we have to include the charge conjugation matrix C, as well as the antisymmetric flavor matrix E. The following shows how to construct a scalar and a pseudo-scalar bilinear [200].

$$\text{scalar } (0^+) \qquad O_S = \bar{\psi}\psi = \frac{1}{2}\left(\Psi^{\mathrm{T}} C \Sigma E \Psi + \text{h.c.}\right) \tag{3.32}$$

$$\text{pseudoscalar } (0^-) \qquad O_P = \bar{\psi}\gamma_5\psi = -\frac{1}{2}\left(\Psi^{T} C \Sigma E \Psi - \text{h.c.}\right) \tag{3.33}$$

This equation encodes the connection of flavor indices that results in a flavor singlet, which is just given by tracing the flavor indices of the quadruplets with the antisymmetric matrix E. Note how the first expression coincides with Equation (1.30) for $N_f = 2$. We can express the scalar and pseudo-scalar singlet operators as [85, 115]

$$O_\sigma^{\mathbf{1}} = \frac{1}{\sqrt{2}}\left[\bar{u}u + \bar{d}d\right], \tag{3.34}$$

$$O_\eta^{\mathbf{1}} = \frac{1}{\sqrt{2}}\left[\bar{u}\gamma_5 u + \bar{d}\gamma_5 d\right]. \tag{3.35}$$

From Equation (3.24) we know that two fundamental fermions can further result in a quintuplet and a decuplet. The decuplet is constructed by symmetrizing the indices. There are $1 + 2 + 3 + 4 = 10$ ways to connect the indices symmetrically and we can use the generators of $Sp(4)$ in the fundamental representation to write a meson decuplet as

$$V_i = 2\bar{\Psi} S_a \Gamma \Psi. \tag{3.36}$$

Here, S_a are the ten generators of $Sp(4)$. In this section, we work with the basis defined Equation (A.35). For $\Gamma = \gamma_5$, the term vanishes as we get the expression $P_R P_L = 0$. Therefore, there is no pseudo-scalar quintuplet in the theory. Identifying $\Gamma = \gamma_\mu$, we obtain the operators for the vector decuplet. We use the basis given in Equation (A.35), which results in bilinears that resemble the charge eigenstates in QCD. A possible vector operator is

$$O_\rho^{\mathbf{10}} = \bar{d}\gamma_\mu u. \tag{3.37}$$

In addition, a decuplet is also realized for a *tensor* state ($J^D = 1^-$) by $\Gamma = \gamma_4\gamma_i$ or a *axial-tensor* by $\Gamma = \gamma_5\gamma_4\gamma_i$ [95]. The quintuplet is built by the remaining contractions of the indices which is obtained by antisymmetrizing but subtracting the trace that was used for the singlet operators [201]. We can write this in terms of the broken $SU(4)$ generators X_i that parameterize the coset $SU(4)/Sp(4)$ from chiral symmetry breaking.

$$\Pi_i = \frac{1}{2}\left[\Psi^T C \Sigma \Gamma X_i E \Psi + \text{h.c.}\right] \tag{3.38}$$

The pseudo-scalar pions with $J^D = 0^-$ are the pNGBs of chiral symmetry breaking and therefore transform in the five-dimensional irrep. We obtain them by choosing $\Gamma = \gamma_5$. As they are the central objects of this thesis and the dark matter candidate, we give the expressions explicitly in terms of quark bilinears [115]

$$\pi^A = \bar{u}\gamma_5 d, \tag{3.39}$$
$$\pi^B = \bar{d}\gamma_5 u, \tag{3.40}$$
$$\pi^C = \frac{1}{\sqrt{2}}\left[\bar{u}\gamma_5 u - \bar{d}\gamma_5 d\right], \tag{3.41}$$
$$\pi^D = \bar{u} C \Sigma \gamma_5 \bar{d}^T, \tag{3.42}$$
$$\pi^E = u^T C \Sigma \gamma_5 d. \tag{3.43}$$

We see that the first three bilinears are equivalent to the $\pi^\pm$ and π^0 bilinears of QCD but we have two additional *diquark* operators that form color singlets in this theory. A scalar, tensor and axialtensor operator can also be built in the five-dimensional irrep [95]. For the construction of pion scattering operators, we can make use of the isomorphism between $Sp(4)$ and $SO(5)$ [202]. We can treat the pion quintuplet as the fundamental multiplet of $SO(5)$ and build the scattering operators from the tensor products of $SO(5)$ which are identical to $Sp(4)$. Since we are now dealing with $SO(5)$, we no longer need to use the antisymmetric matrix E [201]. In the tensor product $\mathbf{5} \otimes \mathbf{5} = \mathbf{1} \oplus \mathbf{10} \oplus \mathbf{14}$, the singlet is again obtained by tracing the indices of the pion quintuplet, the decuplet is given by the antisymmetric and the 14-plet by the symmetric combination. We provide a representative operator for each irrep here, which is sufficient since the $Sp(4)$ flavor symmetry is intact [115, 203]

$$O^{\mathbf{1}}_{\pi\pi} = \frac{1}{\sqrt{5}}\left[\pi^A\pi^B + \pi^B\pi^A - \pi^C\pi^C + \pi^D\pi^E + \pi^E\pi^D\right] \tag{3.44}$$
$$O^{\mathbf{10}}_{\pi\pi} = \frac{1}{\sqrt{2}}\left[\pi^A\pi^B - \pi^B\pi^A\right] \tag{3.45}$$
$$O^{\mathbf{14}}_{\pi\pi} = \pi^A\pi^A \tag{3.46}$$

We provide additional operators relevant for the ten-dimensional channel in Appendix B.

3.3 Lattice Techniques

In this chapter, we introduce the lattice techniques that are specific to our analysis. We obtain energy levels on the lattice by fitting exponential decays of correlation functions which we will introduce in Section 3.3.1 where we also introduce the *variational analysis*. We will introduce the analytic expressions of the correlation functions that are obtained by Wick contractions in Section 3.3.2 and show how to invert them using sources in Section 3.3.3. We discuss the discrete symmetries on the lattice in Section 3.3.4. The Lüscher formalism and the equations for the phase shift used in this work are introduced in Section 3.3.5. Lastly, we will discuss the statistical error analysis driven by the underlying gauge configurations and systematic errors in Section 3.3.6.

3.3.1 Spectroscopy

The determination of energy levels on the lattice is referred to as *spectroscopy*. We refer to [119–121] for a textbook introduction. It is the main technique employed in this work as it is the input for the determination of the mass spectrum as well as the scattering properties. The first step for a spectroscopy calculation is to define the quantum number channel of interest. In our theory this is fully specified by the quantum numbers J^D as well as flavor quantum numbers. As mentioned before, the $Sp(4)$ symmetry is intact in our theory and therefore the irrep label is sufficient to quantify the flavor quantum number channel. In the elastic region and in the continuum, the energy levels are infinitely close. On the lattice these energy levels are realized in a discrete spectrum. The energy levels of an operator O are extracted from correlation functions, which are the expectation values of a state created at a time t and annihilated at a time t'.

$$\begin{aligned} C(t'-t) &= \langle O(t')\bar{O}(t)\rangle && (3.47)\\ &= \sum_k \langle 0|O|k\rangle\langle k|O^\dagger|0\rangle e^{-|t'-t|E_k} && (3.48)\\ &= Ae^{-|t'-t|E_0}(1+\mathcal{O}(e^{-|t'-t|\Delta E})) && (3.49)\end{aligned}$$

Here, we have inserted a complete set of states in the first step. As a result, at large Euclidean time separations, only the leading exponential decay corresponding to the energy of the ground state E_0 dominates the correlation function. Excited-state contamination is exponentially suppressed with $|t'-t|\Delta E$. In the following, we will refer to $|t'-t|$ as t. Finite momenta are added to the correlation function by Fourier transforming the operator.

$$C(t,\vec{p}) = \frac{1}{L^3}\sum_{\vec{x},\vec{y}} e^{-i(\vec{x}-\vec{y})\vec{p}}\langle O(\vec{x},t)\bar{O}(\vec{y},0)\rangle \tag{3.50}$$

$$= Ae^{-tE(\vec{p})} + (1+\mathcal{O}(e^{-t\Delta E})) \tag{3.51}$$

On the lattice, the momentum can only take discretized values given by $\vec{p} = \frac{2\pi}{L}\vec{d},\ \vec{d}\in\mathbb{Z}^3$. In the continuum, the rest mass is obtained by the dispersion relation.

$$E(\vec{p}) = \sqrt{m^2+|\vec{p}|^2} \tag{3.52}$$

There is a dispersion relation that accounts for the periodicity, which reads

$$\cosh(aE(\vec{p})) = \cosh(am) + \sum_{k=1}^{3}(1-\cos(ap_k)), \tag{3.53}$$

and approaches the continuum dispersion relation for vanishing lattice spacing $a\to 0$. In practice, this can be ensured by only considering values for energy levels that are below a certain value $E < E_{max}$, where E_{max} could be chosen as 1 or $\pi/2$. Due to the periodicity of the lattice, the mesons propagate forward and backward in time, which means that the correlation function in the limit of large Euclidean times is the sum of two exponentials with different signs in n_t.

$$C(t) = Ae^{-tE_0} \pm Ae^{-(T-t)E_0} = \begin{cases} A'\cosh(\frac{T}{2}-t)E_0) \\ A'\sinh(\frac{T}{2}-t)E_0) \end{cases} \tag{3.54}$$

The relative sign and with that the form of a cosh or a sinh function depend on the parity of the operator employed. In the second equality, we have moved common prefactors into the definition of A'. In practice, correlation functions are often noisy and the exponential decay is not easily identifiable. Therefore, we need to specify the fit limits carefully by choosing the region where the exponential decay of the ground state dominates. In a log-plot, the correlation function will be straight in this region. The more practical quantity to look at is the *effective mass*.

$$m_{\text{eff}}(t) = \ln\frac{C(t)}{C(t+a)} \tag{3.55}$$

This quantity forms a plateau once the lowest exponential decay dominates at $m_{\text{eff}} = E_0$. In the case of a cosh form, the effective mass can also be defined as

$$m_{\text{eff}}(t) = -\frac{2}{2t-T}\text{arcosh}\frac{C(t)}{C(T/2)}. \tag{3.56}$$

This version of the effective mass relies on small errors at $T/2$. In practice, there is a constant error contribution to the correlator, which makes the data points around $T/2$ very noisy. The fitting region should be chosen such that it only captures the ground state exponential decay and does not pick up too much noise from the center region. There is also the possibility to use a sum of exponentials as a fit function. In this work, we use the *corrfitter* package [204] to reliably extract the energy levels. It uses a Bayesian approach to fit multiple exponential decays.

Depending on the correlation function, there are several phenomena, such as the *around the world* propagation in two hadron correlators [205], that can result in a constant in the correlation function. This constant can be removed by redefining the correlation function as

$$C'(t) = C(t+1) - C(t) \;\; \textit{or} \tag{3.57}$$

$$C''(t) = C(t+1) - C(t-1). \tag{3.58}$$

Note that this is equivalent to a numerical derivative which changes the form from a cosh to a sinh and vice versa. We generally employ this technique. The above framework can be used to determine energies from correlation functions. To compare our results with the ChPT predictions, we further determine the pion decay constant from a $\gamma_4\gamma_5$ operator. The unrenormalized decay constant f_π^0 is defined by the corresponding matrix element

$$\lim_{t\to\infty} C_{\mathcal{O}_{\gamma_4\gamma_5}}(t) = \frac{1}{2m_\pi}|\langle 0|\mathcal{O}_{\gamma_4\gamma_5}|\text{PS}\rangle|^2 \left(e^{-m_\pi t} + e^{-m_\pi(T-t)}\right) \tag{3.59}$$

$$= \frac{\left(f_\pi^0\right)^2 m_\pi}{2}\left(e^{-m_\pi t} + e^{-m_\pi(T-t)}\right). \tag{3.60}$$

We obtain the renormalized pion decay constant via $f_\pi = Z_A f_\pi^0$ by estimating the renormalization constant Z_A using leading-order lattice perturbation theory [85, 92, 206]. This will only affect the ChPT comparison and has no impact on our lattice results.

The simple fitting of a single correlation function is a standard procedure for extracting the lowest energy level. In practice, however, it is often necessary to also calculate higher-lying energy levels. A vital tool for the extraction of excited states is the *variational analysis.* Each correlation function contains contributions from all states that share the same quantum numbers. Variational analysis disentangles the overlaps of the operators and produces a cleaner signal. Instead of just calculating individual correlation functions, we can build the cross-correlation matrix.

$$C_{ij}(t) = \left\langle O_i(t)\bar{O}_j(0)\right\rangle \tag{3.61}$$

The eigenvalues of this matrix encode the energy levels and behave like

$$\lambda^{(k)}(t) \propto e^{-E_k t}(1 + \mathcal{O}(e^{-\Delta E t})). \tag{3.62}$$

In the literature, the generalized eigenvalue problem (GEVP) is often used to extract the eigenvalues. In this work, however, it turned out that solving the ordinary eigenvalue problem is sufficient. The resulting eigenvectors encode the overlap of the different operators with the extracted state. This can in principle be used to construct operators with better overlap. In the work presented here, the largest operator basis we work with consists of three operators, hence this information is not of great importance.

3.3.2 Wick Contractions

So far, we have only looked at the functional form of the final correlation function. In this chapter, we will derive the analytic expressions that follow from *Wick contractions* in terms of quark propagators, which can be evaluated on the gauge ensembles. In general, the meson operators in our theory consist of quark fields. In Equation (3.47), we calculate the expectation value of the annihilation operator and the creation operator of a state. For the operators used in this work, these terms contain quark sources $\bar{q}$ and sinks q which can be used to define the quark propagator as the inverse of the Dirac matrix[3] of a species q is defined as

$$S_q(x|y)^{ab}_{\alpha\beta} = q(x)^a_\alpha \bar{q}^b_\beta(y). \tag{3.63}$$

It is instructive to perform the Wick contraction in a simple example like the pion correlator. The π^B operator with suppressed color and Dirac indices is defined as

$$\pi^B = \bar{d}(x)\gamma_5 u(y). \tag{3.64}$$

---

[3] In the equations, we will denote the quark propagator as $S = D^{-1}$.

This operator carries $J^D = 0^-$ as the quark fields are contracted with a γ_5. x and y are discretized spacetime indices. The quark fields further carry spin-, and color indices. Because of confinement, this operator has to be local such that $\vec{x} = \vec{y}$.[4] The correlation function is

$$\begin{aligned}
C_{\pi^B} &= -\langle \bar{d}(x)^a_\alpha (\gamma_5)_{\alpha\beta} u(x)^a_\beta \bar{u}(y)^b_\gamma (\gamma_5)_{\gamma\delta} d(y)^b_\delta \rangle_f && (3.65)\\
&= -(\gamma_5)_{\alpha\beta}(\gamma_5)_{\gamma\delta} \langle \bar{d}(x)^a_\alpha d(y)^b_\delta \rangle_d \langle u(x)^a_\beta \bar{u}(y)^b_\gamma \rangle_u && (3.66)\\
&= \mathrm{tr}[S_d(y|x)\gamma_5 S_u(x|y)\gamma_5] && (3.67)\\
&= \mathrm{tr}[S_d^\dagger(x|y) S_u(x|y)], && (3.68)
\end{aligned}$$

$\langle\rangle_f$ is the fermionic expectation value that factorizes with respect to the different flavors $f = u, d$. Keep in mind that quark fields are Grassmann valued and therefore anticommute. In the second step, we have applied Wick's theorem to connect all quark lines. In this simple case, there is only one way to contract the quark source and sink of the two species. In multi-hadron operators, all quark sources and sinks of the same species have to be contracted, and the number of terms that result from the Wick contraction scales factorially with the number of quarks. In the last step, we have used the γ_5-hermiticity $\gamma_5 S \gamma_5 = S^\dagger$ of the propagator to show that both propagators are the same object. Note that because we are only considering mass-degenerate quarks, the propagators of the different quark flavors will be numerically identical. On top of the three pion operators that can be expressed as Standard Model bilinears, we have two diquark operators given by Equations (3.42) and (3.43). Performing the Wick contractions for the diquark bilinear will yield

$$C_{\pi^E} = \mathrm{tr}[S_u^T(x|y)\Gamma(\Sigma C)S_d^\dagger(x|y)\Gamma^\dagger(\Sigma C)]. \tag{3.69}$$

Due to the $Sp(4)$ flavor symmetry, we know that the expression must be identical to Equation (3.68). We can use the following relation to eliminate the transposition [118].

$$(C\Sigma)^{-1} S_q^T(y|x)(C\Sigma) = S_q(x|y) \tag{3.70}$$

By inserting this into Equation (3.69), you will obtain the same correlation function as for the *standard* π^B bilinear. All operators in the theory that you can build entirely from the standard bilinears, without ever introducing the diquark operators, *live* on the $SU(2)$ subset and the correlation functions will be identical to the two flavor QCD expressions. This applies to all operators used in this work.

---

[4] You may use non-local operators which will result in *smeared* operators.

However, if you want to investigate singlet channel scattering, for example, the expression above must be used, and the correlation functions will generally be different. The result of the Wick contractions can be represented diagrammatically by connecting spacetime points with arrows that indicate the quark propagators. We can express Equation (3.68) as the following diagram.

$$C_{\pi^B} = \tag{3.71}$$

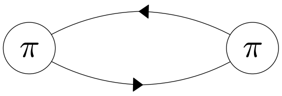

Circles on the left are separated in time from the circles on the right. We also indicate γ_5 as π in the circle. For other γ structures, we may use different symbols, such as ρ for γ_μ. We will show one more example for the Wick contractions of the simplest scattering operator, which is the maximal scattering channel. We indicate it by the dimensionality of the representation in $Sp(4)$ with the superscript **14**.

$$
\begin{aligned}
(\pi\pi)^{\mathbf{14}}(x_1,x_2) =& \pi^A(x_1)\pi^A(x_2) && (3.72)\\
C^{\mathbf{14}}_{(\pi\pi,\pi\pi)}(x_1,y_1;x_2,y_2) =& \langle \pi^A(x_1)\pi^A(x_2)\pi^B(y_1)\pi^B(y_2)\rangle_f && (3.73)\\
=& 2\,\mathrm{tr}[S_d(x_1|y_1)\gamma_5 S_u(y_1|x_1)\gamma_5]\mathrm{tr}[S_d(x_2|y_2)\gamma_5 S_u(y_2|x_x)\gamma_5]\\
& -2\,\mathrm{tr}[S_d(x_1|y_1)\gamma_5 S_u(y_1|x_2)\gamma_5 S_d(x_2|y_2)\gamma_5 S_u(y_2|x_1)\gamma_5]\\
=& 2D - 2C
\end{aligned}
$$

In this case, there are four spacetime points, which means that there are four possible time slices. Ultimately, only the temporal separation between the creation and destruction operators enters the correlation function, and we place two pions on the same time slice. In the last step, we have given the two contractions the name D for *direct* and C for *cross* given their diagrams.

$$C^{\mathbf{14}}_{\pi\pi,\pi\pi} = 2$$

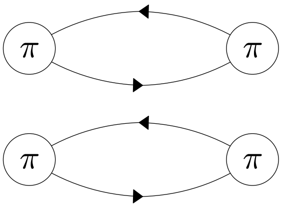

$$-\,2 \tag{3.74}$$

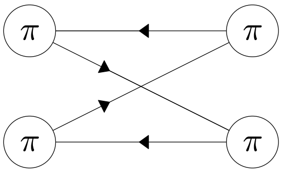

We will present results on the 14-dimensional channel in Section 3.4.1. We also performed a scattering analysis in the ten-dimensional channel where the Wick contractions result in different diagrams. We will employ a ρ operator and a two-pion operator and perform the variational analysis, which means that we also need the off-diagonal entries of the cross-correlation matrix from Equation (3.61).

In this case, the two-pion operator vanishes when both momenta are zero. In the diagrams, we indicate the momenta given to a sink or source by $\vec{p}$, $\vec{q}$, and $\vec{P}_{\text{tot}} = \vec{p} + \vec{q}$. A momentum $\vec{p}$ is added by performing a Fourier transformation at spatial lattice sites with the factor $e^{i\vec{p}\vec{x}}$. Note that momenta at the source receive a factor $e^{-i\vec{p}\vec{x}}$. The ρ correlation function reads

$$C^{\mathbf{10}}_{\rho,\rho} =$$

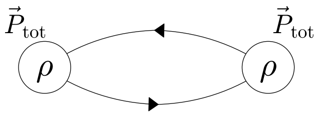

, (3.75)

where ρ may stand for γ_μ or $\gamma_4\gamma_\mu$. The two pion diagrams are

$$C^{\mathbf{10}}_{\pi\pi,\pi\pi} = D_1 - D_2 + R_1 + R_2 - R_3 - R_4$$

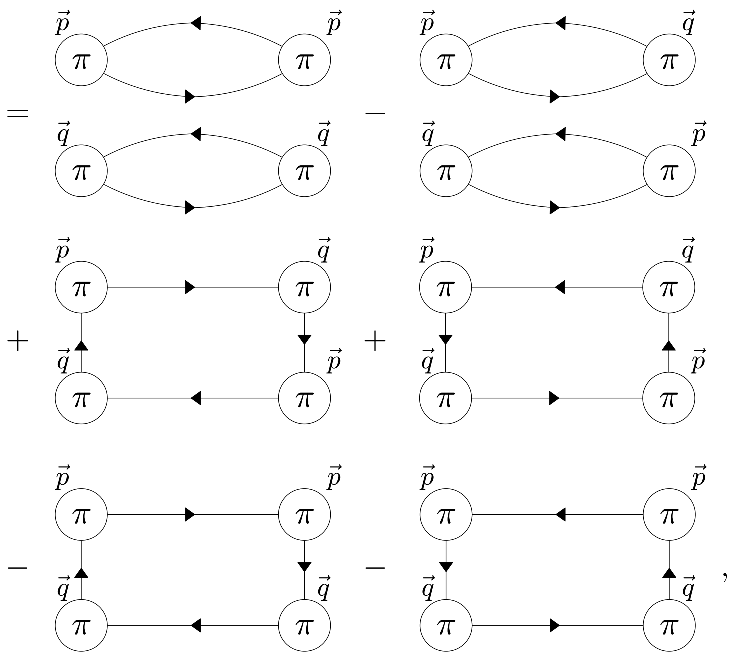

(3.76)

where R_i is for *rectangle*. Because the cross-correlation matrix has to be Hermitian, the cross-diagrams are complex conjugated to each other. They read

$$C^{\mathbf{10}}_{\rho,\pi\pi} = -C^{\mathbf{10}*}_{\pi\pi,\rho} = T_1 - T_2 \tag{3.77}$$

(3.78)

$=$

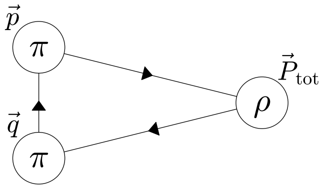

$-$

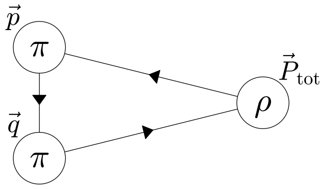

, (3.79)

where T_i is for *triangle*. Although not used in this work, we also give the Wick contractions necessary for singlet-channel scattering. They are obtained from the operator given in Equation (3.44)

$$C^{\mathbf{1}}_{\pi\pi,\pi\pi} = 2D + 3C - 10R + 5V \tag{3.80}$$

$= 2$

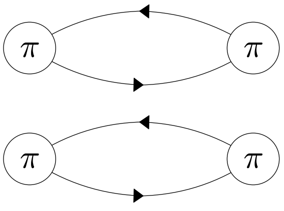

$+ 3$

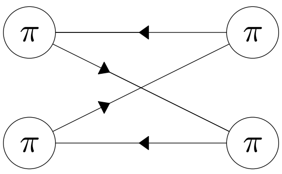

(3.81)

-10

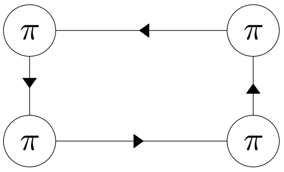

$+ 5$

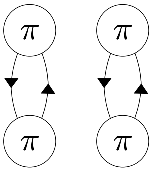

,

where V is for *vacuum*.

3.3.3 Inverting the Dirac Operator

The Dirac operator is a matrix of size $(N_T \times N_L^3 \times 4 \times 4)^2$. Inverting it traditionally is not feasible. However, there are techniques that allows for the efficient inversion of the Dirac operator. In the simple example of a single-pion correlator, the correlation function reads

$$C(t) = \sum_{\vec{x},\vec{y}} \mathrm{tr}[S_q^\dagger(\vec{x},t|\vec{y},0) S_q(\vec{x},t|\vec{y},0)] \tag{3.82}$$

We may now drop the sum over $\vec{y}$ which is equivalent to inserting $\delta(\vec{y}, \vec{z}_0)$.

$$C_{z_0}(t) = \sum_{\vec{x}} \mathrm{tr}[S_q^\dagger(\vec{x}, t|\vec{z}_0, 0) S_q(\vec{x}, t|\vec{z}_0, 0)] \tag{3.83}$$

$$= \sum_{\vec{x},\vec{y}} \mathrm{tr}[S_q^\dagger(\vec{x}, t|\vec{y}, 0)\delta(\vec{y}, \vec{z}_0) S(\vec{x}, t|\vec{y}, 0)] \tag{3.84}$$

$\delta(\vec{y}, \vec{z}_0)$ can be used to define the *point source.*

$$\delta(\vec{x}, \vec{z}_0) = \langle \eta(\vec{x}) | \eta(\vec{z}_0) \rangle \tag{3.85}$$

$$|\eta(\vec{z}_0)\rangle = \sum_{\alpha,a} |\eta_{\alpha,a}(\vec{z}_0)\rangle \tag{3.86}$$

This reduces the calculation of the correlation function to $N_T \times N_c \times 4$ inversions using point sources. Instead of directly inverting the Dirac operator, we can consider its effect on the source $|\phi\rangle = D^{-1}|\eta\rangle$. We can rewrite this as a set of a system of equations involving the Dirac matrix operator $D|\phi\rangle = |\eta\rangle$ that can be solved using, for example, a variant of the *conjugate gradient* method. The point source only probes a single spacetime point, which is insufficient for an effective extraction of a signal from more complicated correlation functions. It has been shown [207] that the use of *stochastic sources* can greatly improve the quality of the correlator. The use of stochastic sources approximates the full propagator and perfectly recovers it in the limit of an infinite number of sources. They obey

$$\delta_{\alpha\beta}\delta^{ab}\delta(x, y) = \frac{1}{N_{\mathrm{src}}} \sum_i |\eta_i\rangle\langle\eta_i|. \tag{3.87}$$

In this work, we employ complex $\mathbb{Z}_2 \times \mathbb{Z}_2$ noise, which means that each element of the source is chosen by a random value from the set $\left\{\frac{i+1}{\sqrt{2}}, \frac{i-1}{\sqrt{2}}, \frac{-i+1}{\sqrt{2}}, \frac{-i-1}{\sqrt{2}}\right\}$. We further employ spin-dilution, where the stochastic source is split up into the sum

$$|\eta^i\rangle = \sum_{\alpha=1}^{4} \delta_{\alpha\beta} |\eta^i_\beta\rangle, \tag{3.88}$$

such that the source of all but one spin index vanishes. This provides another computational advantage. The correlation function is obtained as the average over multiple stochastic sources. In some cases in our calculation, we only employ a single stochastic source, but keep in mind that this still includes different stochastic sources for every configuration. Having decided on a type of source, we can sequentially invert the Dirac operator by taking the result of one inversion as the source for the next. We will illustrate this using a general box diagram with two arbitrary incoming and outgoing momenta, as often found in $\pi\pi$ scattering calculations. A general box diagram is given by

$$C_{4\mathrm{q}} = \sum_{\substack{\vec{x}_1,\vec{x}_2\\ \vec{y}_1,\vec{y}_2}} e^{i\vec{p}(\vec{x}_1-\vec{y}_1)} e^{i\vec{q}(\vec{x}_2-\vec{y}_2)} \mathrm{tr}\left[S(x_1|y_1)\Gamma S(y_1|y_2)\Gamma S(y_2|x_2)\Gamma S(x_2|x_1)\Gamma\right], \tag{3.89}$$

where we have omitted the color and Dirac indices and Γ could be an arbitrary gamma structure but for the sake of simplicity we use here $\Gamma = \gamma_5$, allowing us to use the γ_5-hermiticity of the propagator. The spacetime coordinates x_1 and x_2 are located at the time slice where the state is generated, while y_1 and y_2 are located at the sink. The subscripts 1 and 2 label the two mesons and indicate which momentum they are connected to. Here, we only consider the case where the sink momenta are identical to the source momenta, but the formalism can be extended to more general cases. We can now insert a set of sources as a unit matrix as given in Equation (3.87) like

$$\begin{aligned}
C_{4\mathrm{q}} = (t) = &\sum_{\substack{\vec{x}_1,\vec{x}_2\\ \vec{y}_1,\vec{y}_2,\vec{z}}} e^{i\vec{p}(\vec{y}_1-\vec{x}_1)} e^{i\vec{q}(\vec{y}_2-\vec{x}_2)} \mathrm{tr}[S(x_1|y_1)\gamma_5 S(y_1|y_2)|\eta(y_2)\rangle \\
&\qquad\qquad \langle\eta(z)|\gamma_5 S(z|x_2)\gamma_5 S(x_2|x_1)\gamma_5] \qquad (3.90)\\
= &\sum_{\substack{\vec{x}_1,\vec{x}_2\\ \vec{y}_1,\vec{y}_2,\vec{z}}} e^{i\vec{p}(\vec{y}_1-\vec{x}_1)} e^{i\vec{q}(\vec{y}_2-\vec{x}_2)} \mathrm{tr}[S(x_1|y_1)\gamma_5 S(y_1|y_2)|\eta(y_2)\rangle \\
&\qquad\qquad \langle\eta(z)|S^\dagger(z|x_2)\gamma_5 S^\dagger(x_2|x_1)] \qquad (3.91)\\
= &\sum_{\substack{\vec{x}_1,\vec{x}_2\\ \vec{y}_1,\vec{z}}} e^{i\vec{p}(\vec{y}_1-\vec{x}_1)} e^{-i\vec{q}\vec{x}_2} \mathrm{tr}[S(x_1|y_1)\gamma_5 Q_\eta(\vec{y}_1,t_s|\vec{q},t_s) \\
&\qquad\qquad Q_\eta^\dagger(\vec{x}_2,t_0|\vec{0},t_s)\gamma_5 S^\dagger(x_2|x_1)] \qquad (3.92)\\
= &\sum_{\vec{x}_1} e^{-i\vec{p}\vec{x}_1} \mathrm{tr}[W_\eta(\vec{x}_1,t|\vec{p},t_s|\vec{q},t_s) W_\eta^\dagger(\vec{x}_1,t|\vec{q},t_0|\vec{0},t_s)], \qquad (3.93)
\end{aligned}$$

where t_0 and t_s are the source and sink time, respectively, and $t = |t_0 - t_s|$. We define the sequential sources as [208]

$$Q_\eta(\vec{y},t_2|\vec{q},t_3) = \sum_{\vec{z}} e^{i\vec{q}\vec{z}} S(\vec{y},t_2|\vec{z},t_3)|\eta(\vec{z},t_3)\rangle \tag{3.94}$$

$$W_\eta(\vec{x},t_1|\vec{p},t_2|\vec{q},t_3) = \sum_{\vec{y}} e^{i\vec{y}\vec{p}} S(\vec{x},t_1|\vec{y},t_2)\gamma_5 Q_\eta(\vec{y},t_2|\vec{q},t_3). \tag{3.95}$$

Note that W is a sequential source that uses the sequential source Q as its source vector. We can express all the box diagrams of the ten-dimensional $\pi\pi$ correlator from Equation (3.76) in this way. The direct diagrams are

$$D_1 = \sum_{\vec{x}} e^{-i(\vec{p}\vec{x}+\vec{q}\vec{y})} \mathrm{tr}\left[Q^\dagger_\eta(\vec{x},t|\vec{0},t_s)Q_\eta(\vec{x},t|\vec{p},t_s)\right] \mathrm{tr}\left[Q^\dagger_\xi(\vec{y},t|\vec{0},t_s)Q_\xi(\vec{y},t|\vec{q},t_s)\right], \tag{3.96}$$

$$D_2 = \sum_{\vec{x}} e^{-i(\vec{p}\vec{x}+\vec{p}\vec{y})} \mathrm{tr}\left[Q^\dagger_\eta(\vec{x},t|\vec{0},t_s)Q_\eta(\vec{x},t|\vec{q},t_s)\right] \mathrm{tr}\left[Q^\dagger_\xi(\vec{y},t|\vec{0},t_s)Q_\xi(\vec{y},t|\vec{q},t_s)\right]. \tag{3.97}$$

The rectangular diagrams are

$$R_1 = \sum_{\vec{x}} e^{-i\vec{p}\vec{x}} \mathrm{tr}\left[W_\eta(\vec{x},t|\vec{p},t_s|\vec{0},t_s)W^\dagger_\eta(\vec{x},t|\vec{q},t_0|-\vec{q},t_s)\right], \tag{3.98}$$

$$R_2 = \sum_{\vec{x}} e^{-i\vec{p}\vec{x}} \mathrm{tr}\left[W_\eta(\vec{x},t|-\vec{q},t_0|\vec{0},t_s)W^\dagger_\eta(\vec{x},t|-\vec{q},t_s|-\vec{p},t_s)\right], \tag{3.99}$$

$$R_3 = \sum_{\vec{x}} e^{-i\vec{p}\vec{x}} \mathrm{tr}\left[W_\eta(\vec{x},t|\vec{p},t_s|\vec{0},t_s)W^\dagger_\eta(\vec{x},t|\vec{q},t_0|-\vec{q},t_s)\right], \tag{3.100}$$

$$R_4 = \sum_{\vec{x}} e^{-i\vec{p}\vec{x}} \mathrm{tr}\left[W_\eta(\vec{x},t|-\vec{q},t_0|\vec{0},t_s)W^\dagger_\eta(\vec{x},t|-\vec{p},t_s|-\vec{q},t_s)\right], \tag{3.101}$$

and the triangular diagrams for the cross-correlations are

$$T_1 = \sum_{\vec{x}} e^{-i\vec{p}\vec{x}} \mathrm{tr}\left[W^\dagger_\eta(\vec{x},t|-\vec{p},t_s|\vec{0},t_s)(\gamma_5\gamma_i)Q_\eta(\vec{x},t|\vec{0},t_s)\right], \tag{3.102}$$

$$T_2 = \sum_{\vec{x}} e^{-i\vec{p}\vec{x}} \mathrm{tr}\left[Q^\dagger_\eta(\vec{x},t|\vec{0},t_s)(\gamma_5\gamma_i)W_\eta(\vec{x},t|\vec{p},t_s|\vec{0},t_s)\right]. \tag{3.103}$$

Numerically, we find $D_2 \ll D_1$, $R_1 = R_2$, $R_3 = R_4$, and $T_1 = -T_2$. Furthermore, all the D and R diagrams are real, while the T diagrams are purely imaginary within statistics.

3.3.4 Discrete Symmetries on the Lattice

An important symmetry that is broken on the lattice is the rotational symmetry. In the continuum, we can describe the freedom to express our formulas in a rotated coordinate system by an $O(3)$ symmetry. On the lattice, only a subset of discrete rotations describe a symmetry of the Lagrangian. Understanding the discrete symmetries on the lattice will enable us to achieve the desired results despite this challenge.

The discrete symmetry that describes a cubic lattice is given by the rotations that leave the endpoints of a cube invariant. This symmetry is given by the octahedral group O. In general, the lattice is also left invariant by inversions which are included by adding a minus sign to the same rotations. The resulting symmetry is denoted as O_h. For fermionic observables, whose wave functions are antisymmetric, the symmetry on the lattice is given by the double cover of O_h denoted by the superscript ^{2}. This is the equivalent of using the double cover of $O(3)$, i.e., $SU(2)$, in the continuum.

As we shall see in the following, there are practical reasons and physical constraints that make it interesting to look at subgroups of O_h – the so-called little groups (LGs). Especially for scattering, it is crucial to employ operators at non-vanishing momentum. In that case, the lattice frame will no longer be equivalent to the center-of-mass frame. Boosting to the center-of-mass frame will deform the lattice sites from a cube to a parallelepiped, depending on the total momentum employed. Let us consider for a moment the scenario in which we employ two particles of unequal masses. In this case, the inversion is no longer part of the symmetry of the lattice. A consequence of this is that contributions from even and odd partial waves will mix, which is not the case for equal masses. Working with the smaller symmetry group in the case of unequal masses simplifies many expressions, and we are free to do so since the case of equal masses is merely a generalization that makes no difference in cases such as the construction of operators [209].

Table 3: The subgroups (LGs) of O_h that describe the symmetry of the deformed lattice after boosting to the center-of-mass frame [210] with momentum $\vec{d}$.

$\vec{d}$	LG	class	$N_{elements}$
(0,0,0)	O_h	cubic	48
(0,0,a)	D_{4h}	tetragonal	16
(0,a,a)	D_{2h}	orthorhombic	8
(a,a,a)	D_{3d}	trigonal	12
(0,a,b)	C_{2h}	monoclinic	4
(a,a,b)	C_{2h}	monoclinic	4
(a,b,c)	C_i	triclinic	2

Let us now consider the consequences that arise when we employ states with non-vanishing total momentum. In general, there are equivalent classes of total momenta that result in the same LG. These are shown in Table 3. In this work, we only consider the cases shown in the first four rows. Where possible, we define the z-axis as the axis of the largest symmetry. As mentioned above, we may work with a smaller group that does not include the element of inversion. The groups O,

C_{4v}, C_{2v} and C_{3v} result in the LG from Table 3 when combined with the element of inversion.[5]

$$O_h = O \quad \otimes\{-1,1\} \tag{3.104}$$

$$D_{4h} = C_{4v}\otimes\{-1,1\} \tag{3.105}$$

$$D_{3d} = C_{2v}\otimes\{-1,1\} \tag{3.106}$$

$$D_{2h} = C_{3v}\otimes\{-1,1\} \tag{3.107}$$

The LGs also contain irreps which leave a subspace of the deformed lattice invariant. A powerful consequence of applying irreps to scattering on the lattice is that the different irreps disentangle the mixing of partial waves. While each irrep will still contain an infinite number of partial waves, there will be partial waves that are not probed by certain irreps. The irreps employed in this work probe p-wave scattering to lowest order and f-wave to next order. In the literature, the approximation that only the lowest partial wave will contribute, is often used. This approximation is necessary to make the computations feasible as it is not possible to extract an infinite amount of parameters from the data. In QCD, it was shown in lattice studies [211] and experimental data [212] that higher partial waves are highly suppressed. We will neglect contributions from partial waves $l \geq 2$.

Now that we know how rotational symmetry is broken on the lattice, we can work out its consequences. Spectroscopy measurements on the lattice are performed in a specific quantum number channel. In the continuum, this is specified by J^D and the irrep of the flavor symmetry. The broken rotational symmetry splits up the spectrum on one more level which is given by the irrep of the LG. It is possible to project operators onto a specific irrep, such that they only probe a subset of the possible finite-volume energy levels. By choosing the irrep properly, one can disentangle contributions to the phase shift from different partial waves. The variational analysis also has to be performed for each irrep individually. In that sense, one could consider the irrep of the LG an additional quantum number that is present in the finite-volume case. It specifies how an operator transforms under the elements of the LG in the center-of-mass frame. The elements are three-dimensional rotations and inversions which act on three-vectors like momenta but also on the intrinsic polarizations of vector particles. We can project a naive operator in a certain irrep using the projection formula

$$O^{\Gamma}_{cm}(\vec{p},t) = \frac{\dim(\Gamma)}{N_{\text{LG}}}\sum_i \chi_{\Gamma}(S_i)\hat{S}_i O_{cm}(\vec{p},t). \tag{3.108}$$

---

[5] The groups O, D_4, D_2 and D_3 would also fulfill this property.

Here, Γ labels the irrep of the LG, $\dim(\Gamma)$ is its dimension, and $\chi_\Gamma(S_i)$ is the *character* of the group element S_i with respect to the irrep. The operator projection works in the center-of-mass frame, and therefore $\vec{p}$, here, is the back-to-back center-of-mass three-momentum. The character tables of the LGs obtained from finite momenta considered in this work are shown in Tables 4–6.

Table 4: The character table of C_{4v} [209, 213].

irrep	I	$2C_4$	$2IC_2'$	$2IC_2$	C_2
A_1	1	1	1	1	1
A_2	1	1	-1	-1	1
B_1	1	-1	-1	1	1
B_2	1	-1	1	-1	1
E	2	0	0	0	2

Table 5: The character table of C_{2v} [209, 213].

irrep	I	C_2'	IC_2'	IC_2
A_1	1	1	1	1
A_2	1	1	-1	-1
B_1	1	-1	1	-1
B_2	1	-1	-1	1

Table 6: The character table of C_{3v} [209, 213].

irrep	I	$2C_3$	$3IC_2'$
A_1	1	1	1
A_2	1	1	-1
E	2	-1	0

There is an additional label $^\pm$ for the irreps of the LGs with inversions that denote their parity. The operators that we will project onto the irreps are already of definite parity, and we can use the simpler tables from the groups without inversions. Using these tables, we can project the vector meson and two pion operators in the desired irreps. Prior to the projection, these operators are

$$\pi\pi(\vec{p}\,) = \pi(-\vec{p}\,)\pi(\vec{p}\,) = \sum_{\vec{x},\vec{y}} e^{i(\vec{p}\vec{x}+\vec{q}(\vec{x}-\vec{y}))}\pi(\vec{x})\pi(\vec{y}), \tag{3.109}$$

$$\rho(\vec{p}\,) = \begin{pmatrix} \rho_1(\vec{p}\,) \\ \rho_2(\vec{p}\,) \\ \rho_3(\vec{p}\,) \end{pmatrix}, \ \rho_i(\vec{p}\,) = \sum_{\vec{x}} e^{i\vec{p}\vec{x}}\bar{q}(\vec{x})\gamma_i q(\vec{x}), \tag{3.110}$$

Table 7: The operators employed in this work for the analysis of the ten-dimensional channel projected into different irreps Γ using Equation (3.108) [209]. We employ $\pi\pi$ operators only in the A_1 irreps. This case coincides with one pion carrying all momentum while the other one is at rest.

LG	$\vec{d}$	Γ	ρ	$\pi\pi$
O_h	(0,0,0)	T_1	$\rho_x + \rho_y + \rho_z$	-
C_{4v}	(0,0,1)	A_1	ρ_z	$\pi(\vec{d})\pi(0)$
		E	$\rho_x + \rho_y$	-
C_{2v}	(1,1,0)	A_1	$\rho_x + \rho_y$	$\pi(\vec{d})\pi(0)$
		B_1	ρ_z	-
C_{3v}	(1,1,1)	A_1	$\rho_x + \rho_y + \rho_z$	$\pi(\vec{d})\pi(0)$
		E	$2\rho_x - \rho_y - \rho_z$	-

where we omit all but spatial indices and only consider three spatial polarizations of the ρ. Although not relevant here, we will mention that π-operators, due to their pseudo-real nature, will receive a minus sign upon inversion. In the maximal channel, we only consider zero-momentum operators where the irrep is trivial. For the study of the ρ resonance in Section 3.4.2, we employ vector meson and two-pion operators. In the LG O_h we investigate the T_1 irrep, for C_{4v}, A_1 and E, for C_{2v}, A_1 and B_1,[6] and for C_{3v}, again A_1 and E.[7] We supplement these operators with a tensor operator that has a $\gamma_4\gamma_i$ structure. Only in the irreps A_1 we build a non-trivial cross-correlation matrix. This is because the two meson operators in the other irreps require momenta attached to both mesons, which is numerically more costly. This means that in the T_1, E and B_1 irreps, we only employ vector meson operators which are specified by the alignment of the momentum vector with their intrinsic polarization. The projected operators used in this work are shown in Table 7.

3.3.5 Lüscher Formalism

Spectroscopy calculations in lattice field theory result in energy levels in finite-volume. In a large volume, these can be identified as the masses of the investigated states. In this work, we investigate the scattering properties of two-by-two processes. This is possible because the finite-volume energy levels obtain a differ-

---

[6] Note that in this case, the operators from the A_1 and B_2 irrep are equivalent and that there does not exist a vector meson operator in the A_2 irrep. Also note that the specific form of the operators and the labeling of the irreps depends on the definitions.

[7] Note that the E irrep in both cases is two-dimensional giving rise to two linearly independent operators.

ent interpretation, once two particle states are considered. The wave functions of two particles in a finite box have an overlap and will therefore interact. Lüscher first described this feature in the context of relativistic quantum mechanics and derived a relation between the finite-volume energy levels and the infinite-volume phase shift known as the *Lüscher quantization condition* [214–216]. Initially, the quantization condition was derived for two scalar particles in the center-of-mass momentum, where the lattice sites resemble a cubic lattice. Later, it was generalized for different lattice symmetries [210], which are realized when finite relative momenta in the center-of-mass frame are used. This allows for a more detailed investigation of the energy dependence, as operators in different irreps of the LGs generally result in different energy levels. It also allows for a better examination of the partial waves. The formalism has also been extended to the mass non-degenerate case where the loss of the element of inversion in the symmetry group causes even and odd partial waves to mix [208, 217, 218]. Finally, the formalism has been extended to three-particle scattering with the *three-particle quantization condition* [195–198].

The two-particle quantization condition is applicable for finite-volume energy levels between the elastic threshold and the first inelastic threshold given by the next massive stable state in the theory, usually the four-particle threshold. Furthermore, discretization artifacts and exponential finite-volume corrections have to be negligible, and the temporal extent is taken to be infinite. Let us first consider the kinematics of a two-particle system in a finite-volume. On the lattice, momenta can only take discretized values following

$$\vec{p} = \frac{2\pi}{L}\vec{d}, \;\; \vec{d} \in \mathbb{Z}^3. \tag{3.111}$$

Without any interaction, the two-particle energy in the mass-degenerate is given by

$$E^{\vec{P}}_{\text{non-int}} = \sqrt{m^2 + |\vec{p}_1|^2} + \sqrt{m^2 + |\vec{p}_2|^2}, \tag{3.112}$$

where we have defined the total momentum $\vec{P} = \vec{p}_1 + \vec{p}_2$. In the presence of interactions, these energy levels shift. The center-of-mass energy squared is then given by

$$s^{\vec{P}} = \left(E^{\vec{P}}\right)^2 - \vec{P}^2 \tag{3.113}$$

$$= 4\left(m^2 + p^{*2}\right), \tag{3.114}$$

where we have defined the scattering momentum p^* as the back-to-back momentum in the center-of-mass frame in the interacting case. Note that this quantity will, in general, take continuous values. The lattice dispersion relation may be used for Equations (3.112)–(3.114). The scattering formulas will use the dimensionless form of this quantity $q = \frac{pL}{2\pi}$. The quantization condition results in a determinant equation which will take a different form for every LG resulting from the total momentum and irrep.

$$\det\left[\mathcal{M}^{\Gamma}_{lm,l'm'} - \delta_{ll'}\delta_{mm'}\cot\delta_l\right] = 0 \tag{3.115}$$

Here, δ_l is the phase shift of partial wave l and Γ is the irrep of LG. This formula can usually be written as a function for $\cot\delta_l$ depending on

$$w^{\vec{P}}_{lm} = \frac{\mathcal{Z}^{\vec{P}}_{lm}(1;q^2)}{\pi^{3/2}\sqrt{2l+1}\gamma q^{l+1}}, \tag{3.116}$$

where $\gamma = E^{\vec{P}}/\sqrt{s^{\vec{P}}}$ and

$$\mathcal{Z}_{lm}(1;q^2) = \sum_{\vec{r}\in P_d} \frac{\mathcal{Y}_{lm}(\vec{r})}{\left(\vec{r}^2 - q^2\right)^s},\ P_d = \left\{\vec{r}|\vec{r} = \gamma^{-1}\vec{n}\right\},\ \vec{n}\in\mathbb{Z}^3, \tag{3.117}$$

is the *Lüscher Zeta function* with $\mathcal{Y}_{lm}(\vec{r}) = x^l Y_{lm}(\theta,\phi)$ defined with the usual spherical harmonics. Examples of numerical implementations can be found in [217, 219, 220].[8] In the analysis of the 14-dimensional channel where we do not employ any momenta and are interested in the s-save cross section, the phase shift can be calculated as

$$\cot\delta_0 = w_{00}(q^2) = \frac{\mathcal{Z}^{\vec{0}}_{00}(1;q^2)}{\pi^{3/2}q}. \tag{3.118}$$

For the ten-dimensional channel, we employ momenta and investigate different lattice irreps. The p-wave phase shift δ_1 is obtained differently in each of the irreps. The specific phase shift formulas used are given in Table 8.

3.3.6 Statistical and Systematic Errors

When it comes to error estimation, lattice field theory works very much like an experiment. Therefore, results are only meaningful if they are based on a proper error analysis. The generation of gauge configurations in Section 1.3.1 is a statistical procedure. The first step is to check whether the gauge configurations are

---

[8] We thank Luka Leskovec for providing his code that was used for the numerical evaluation of the Zeta function in this work.

Table 8: The $l = 1$ phase shift in different irreps of the LGs expressed in terms of w_{lm} from Equation (3.116) that result from the quantization condition taking the symmetries of the lattice and LGs into account [194, 209, 210].

LG	$\vec{d}$	Γ	$\cot \delta_1$
C_{4v}	(0,0,1)	A_1	$w_{00} + 2w_{20}$
		E	$w_{00} - w_{20}$
C_{2v}	(1,1,0)	A_1	$w_{00} - w_{20} - i\sqrt{6}w_{22}$
		B_1	$w_{00} + 2w_{20}$
C_{3v}	(1,1,1)	A_1	$w_{00} - w_{20} + i\sqrt{6}w_{22}$
		E	$w_{00} + i\sqrt{6}w_{22}$

statistically uncorrelated. In this work, this is done by calculating the *autocorrelation time* of the plaquette. We treat the set of gauge configurations as uncorrelated if the autocorrelation time is $\lesssim 1$. From that point onward every measurement on a gauge configuration can be treated as one iteration of an experiment, and we use statistical resampling methods to propagate the error properly through the in part nonlinear processes like fitting. The most consistent and efficient resampling technique is *delete-1 jackknife* resampling. The set of gauge configurations is resampled by taking the mean of the sample, excluding every data point once. This will result in a new set of equal size. Then we proceed by making any calculation with every entry in that new set to obtain a sample of results. This could, for example, be the extraction of energy levels from a fit to the correlation function. We can investigate the distribution of the values in this set and extract the mean, median and standard deviation. For all quantities obtained with delete-1 jackknife in this work, the mean and median coincide within statistics. Obviously, this new set is highly correlated and the result of the measurement has to be quoted as

$$\theta = \hat{\theta} \pm \sigma_{\hat{\theta}} \tag{3.119}$$

$$\sigma_{\hat{\theta}}^2 = \frac{N-1}{N} \sum_{n=1}^{N} \left(\theta_n - \hat{\theta}\right)^2 , \tag{3.120}$$

where the factor of $N - 1$ accounts for the correlation. $\hat{\theta}$ is the mean value, $\sigma_{\hat{\theta}}$ is the standard deviation and N is the size of the set. This method is very powerful, as long as we only have to work with a single set. If we want to perform calculations that involve multiple lattices like different volumes in the infinite-volume extrapolation or in the Lüscher analysis, we have to resample in a different way. In this work, we resample a given set according to its distribution. We switch from jackknife to this method after the determination of the energy levels. First, we convince ourselves that the set of energy levels follows a Gaussian distribution. Afterwards, we resample that set according to the standard deviation of the set. The advantage is that the error of different ensembles can be propagated straightforwardly. In this new set, the mean is equal to the median and the 1σ error is given by the $\mathrm{erf}(\frac{1}{\sqrt{2}}) \approx 68\%$ of points around that point.

In addition to the statistical analyses, there are also sources of systematic errors in lattice calculations. We do not quote systematic errors in our results but try to be transparent in the procedures leading to the results and discuss potential systematics where necessary. These include finite-volume effects, discretization artifacts, infinite-volume extrapolations, insufficiently large operator bases, the use of an unimproved lattice action, a finite number of stochastic sources, and disregarding higher partial waves. The work that has led to this thesis has been the first lattice scattering analysis in $Sp(4)_c$ gauge theory as a dark matter candidate where experimental data are rare. Given its exploratory nature and the fact that the target precision is usually of the order of magnitude, we deem this to be adequate.

3.4 Results

In this section, we present results for scattering properties in two different flavor channels. Lattice results in $SU(2)_c$ and $SU(3)_c$ can, for example, be found in [107, 114, 194]. Some of the ensembles correspond to different lines of constant physics and can therefore not be compared naively. In a first step, we will look at the energy levels obtained from fitting the exponential decay of correlation functions and their dependence on the spatial volume of the lattice. In spectroscopy calculations, the energy levels in the infinite volume can be identified with masses of particles. For scattering states, energy levels might indicate bound states if their energy is smaller than the elastic threshold. Energies between the elastic and inelastic thresholds correspond to scattering states, which in a finite volume, receive contributions from the phase shift which can be examined using the Lüscher quantization condition. In contrast to spectroscopy calculations, it is useful to investigate smaller lattices, as they have larger finite-volume effects. In Section 3.4.1, we consider the 14-dimensional maximal scattering channel. By a naive counting, most pions are expected to scatter in this channel. We obtain the low-energy s-wave cross section from ERE and compare it with astrophysical constraints. In Section 3.4.2, we employ $J^D = 1^-$ operators in the ten-dimensional channel to investigate the properties of the vector meson in the theory. We consider three

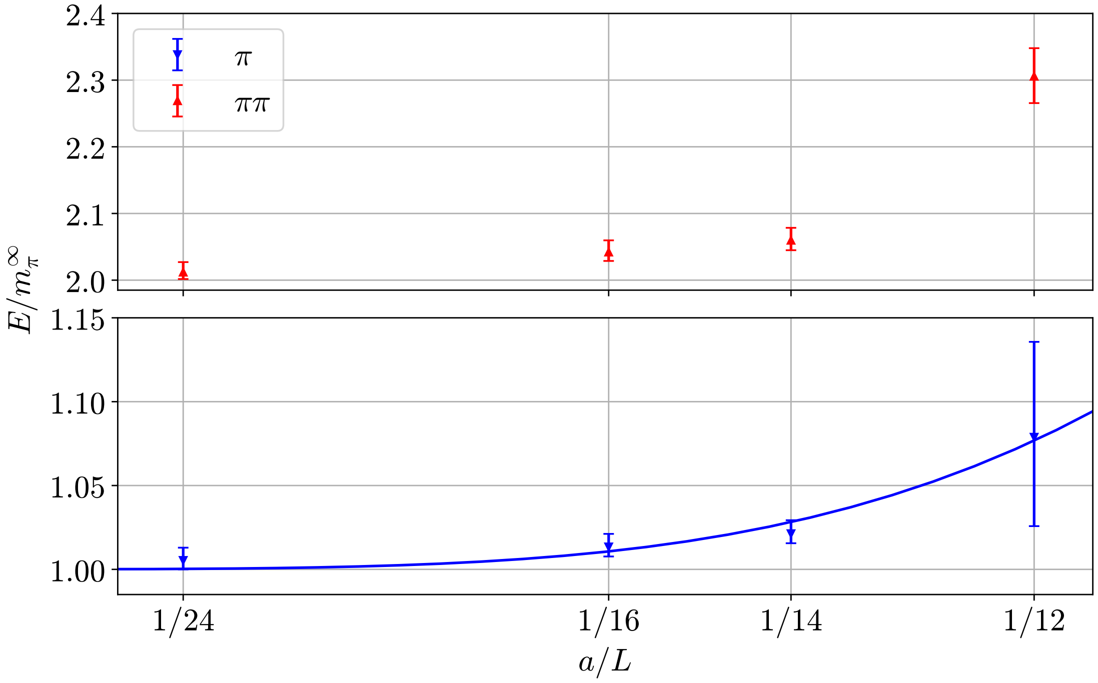

Figure 8: Bottom panel: The extracted pion energy levels plotted against the inverse lattice extent for the ensemble with $\beta = 6.9$ and $am_0 = -0.9$. The line and band indicate the mean and estimated error of the infinite-volume extrapolation using Equation (1.51). The results of the infinite-volume extrapolated pion mass generally agrees with the energy level on the largest lattice within errors. Top panel: The results for the two-pion energy levels. Both y-axes are scaled with m_π^∞ extracted from the fit in the bottom panel.

different cases, which showcase the transition of the energy of the naive ρ-operator going from below $2m_\pi$ to the elastic window. We therefore expect a resonance to emerge. We obtain the low-energy p-wave cross section in the non-resonant case. In the resonance case, we see a stable bound state but also obtain parameters of a resonance. In Section 3.1.3, we show results of the cross section.

3.4.1 Maximal Scattering Channel

The results of this section were published in [221, 222] and we will repeat the main findings here with the ensembles that are more resistant to lattice artifacts. For these ensembles, $N_L > 8$, $m_\pi/m_\pi^\infty < 1.3$, and $aE_{\pi\pi} < 0.95$. They are summarized in Table 12. The ensembles are chosen to be approximately on a line of constant physics defined by the value of m_π/m_ρ that ranges from $0.70 - 0.87$. The two-pion energy levels are obtained from the operator given in Equation (3.46). Figure 8

Table 9: The results of the best fits for the infinite-volume pion mass, the pion decay constant as well as the scattering length and the effective range from first order ERE with Equation (3.13) up to $\mathcal{O}(p^2)$. We observe consistently a positive scattering length which corresponds to a repulsive interaction between the pions. For some ensembles, the error of the effective range is larger than its value but this did not affect the estimation of the scattering length significantly.

β	am_0	$am_\pi^\infty \times 10^4$	af_π	$a_0 m_\pi$	$r_0 m_\pi$
6.9	-0.92	3844^{+19}_{-30}	0.08271(58)	$0.52^{+0.24}_{-0.21}$	$6.9^{+10.4}_{-4.1}$
7.05	-0.835	4373^{+9}_{-9}	0.0795(16)	$0.71^{+0.16}_{-0.26}$	$1.9^{+1.4}_{-0.4}$
7.05	-0.85	3297^{+12}_{-13}	0.0686(12)	$0.56^{+0.14}_{-0.22}$	$4.4^{+7.7}_{-2.1}$
7.2	-0.78	3696^{+4}_{-4}	0.06669(67)	$0.73^{+0.07}_{-0.08}$	$2.2^{+0.3}_{-0.2}$
7.2	-0.794	2837^{+13}_{-14}	0.05792(61)	$0.88^{+0.13}_{-0.14}$	$1.2^{+0.5}_{-0.4}$

shows the energy levels for $\beta = 6.9$ and $am_0 = -0.92$ at different lattice volumes. In the bottom panel, we show the results of fitting the different spatial lattice extents to Equation (1.51) in order to obtain the value for m_π^∞. We see that the single-pion energy level in the largest lattice is usually consistent with the infinite-volume mass extracted from the fit. We consistently observe a positive energy shift $E_{\pi\pi} - 2m_\pi^\infty$ that is larger for smaller lattices just as expected. This is precisely the finite-volume effects that are present due to scattering effects and that can be used to calculate the phase shift with the Lüscher formalism.

We do not employ any finite momentum in this channel, and therefore the energy levels correspond to the center-of-mass energy. The scattering momentum p is obtained by using $E_{cm} = 2\sqrt{m_\pi^{\infty\,2} + p^2}$. The final results are consistent with the use of the lattice dispersion relation from Equation (3.53). We calculate the phase shift using Equation (3.118). As we do neither expect nor see any hints of resonances, and are interested in the non-relativistic scattering properties, we investigate the data in the framework of ERE. Close to threshold, ERE holds universally and dictates that the phase shift can be expanded in orders of p^2. Figure 9 shows that phase shift plotted against the center-of-mass energy squared. The y-axis of the bottom panel is motivated by the left-hand side of Equation (3.13) and ERE to first order appears as a line.[9] All energies are scaled with the mass of the pion. The green line and band show the linear fit to first-order ERE, which was the best fit for all ensembles. The scattering length is the negative inverse y-axis intercept and is consistently positive, relating to a repulsive interaction. The slope of the fit in the bottom panel of Figure 9 is related to the effective range, which is

---

[9] Note, that having the center-of-mass energy squared on the x-axis will still result in a line since $s = 4(m_\pi^2 + p^2)$.

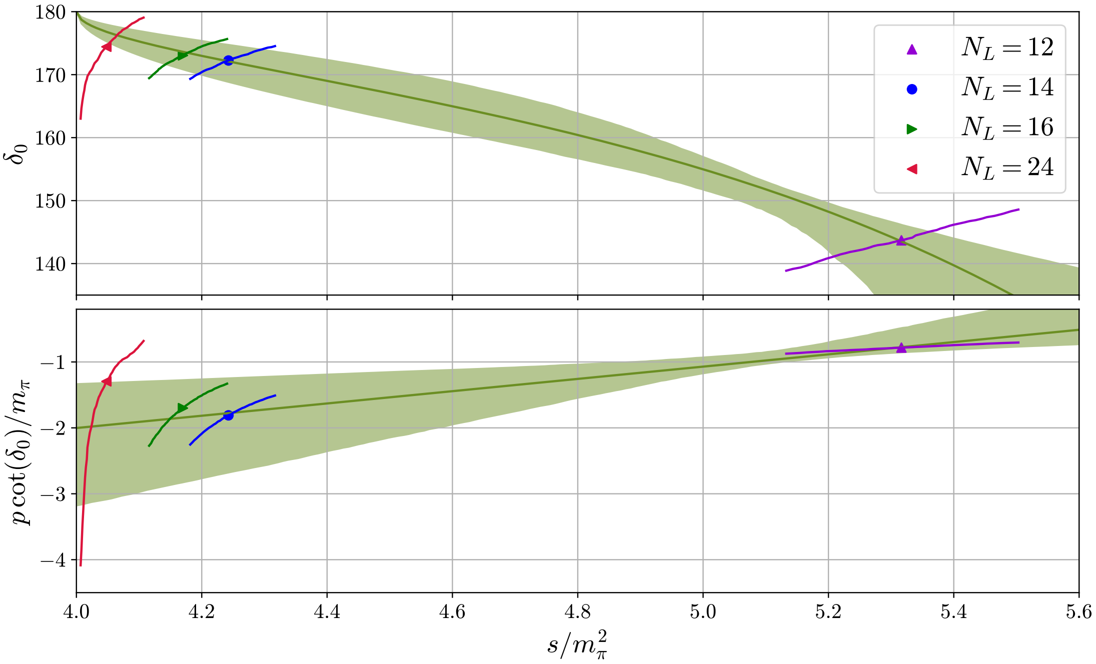

Figure 9: Result of the Lüscher analysis in the 14-dimensional channel for $\beta = 6.9$ and $am_0 = -0.92$. The left-hand side of s-wave ERE from Equation (3.13) plotted against the center-of-mass energy squared is shown in the bottom panel. The top panel shows the s-wave phase shift. The green lines and band show the median and error estimate. The curved error bars indicate, that the two axes are not independent and only values on the curved lines are allowed.

subject to large errors. Given the positive value of the effective range, it seems that the line might intersect the x-axis at larger center-of-mass energies, but since we do not have any data points in that regime and ERE is only valid at low energies, this does not infer a potential resonance. We give the best estimates for the scattering length and effective range together with the extracted infinite-volume pion masses in Table 9. These results give a good indication for the low-energy s-wave cross section which is particularly interesting for dark matter phenomenology. We show the energy levels and phase shift of all ensembles in Table 12.

Finally, we can use the results of the fits to compare our results with the leading-order prediction on the scattering length from ChPT [193] which we introduced in Equation (3.17), which is shown in Figure 10. The lattice data consistently result in a larger scattering length than the prediction from ChPT but are compatible within 1σ, indicating that ChPT can be applied safely in this regime – see also [95, 223]. This statement is not trivial, as the values of m_π^∞/f_π are relatively large. The slight underestimate of the ChPT prediction could be resolved by next-to-leading-

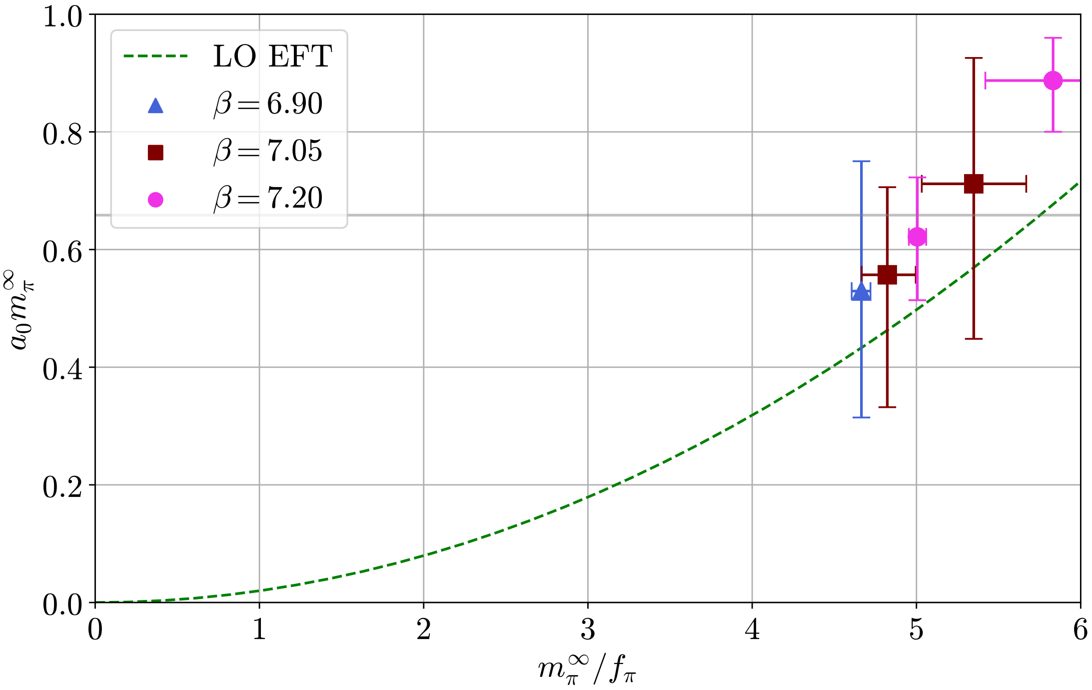

Figure 10: The scattering length obtained from the fits to ERE plotted against the ratio of the mass and the decay constant of the pion. The left side of the plot represents the chiral limit. Different colors and symbols correspond to different values of the inverse coupling β. We observe a consistent positive scattering length across all ensembles which corresponds to a repulsive interaction. The horizontal gray line and band indicate a central value and error for the scattering length estimated using all of our ensembles. The green dashed line shows the leading order prediction from ChPT [193].

order-ChPT calculation, however, this introduces additional LECs. In [224], the results of this work were used together with spectroscopy calculations from [85] to extract the next-to-leading-order LECs of the theory. We can further compare the cross section at threshold given by $4\pi a_0$ with astrophysical data from [18, 43, 47] which we approximate with $\sigma/m_{\text{DM}} < 0.2\,\text{cm}^2/\text{g}$ due to the large uncertainties involved. Choosing a conservative lower bound for the scattering length of $a_0 m_\pi^\infty > 0.43$ results in a constraint for the dark matter candidate mass of $m_{\text{DM}} > 135$ MeV which fits the estimated range for SIMP dark matter based on perturbative considerations well [51].

Table 10: The ensembles used in this work to investigate the ten-dimensional channel together with the number of gauge configurations and the number of stochastic sources used.

β	am_0	N_L	N_T	n_{config}	n_{src}
6.9	-0.92	14	24	550	32
6.9	-0.92	16	32	288	16
6.9	-0.92	20	32	360	16
6.9	-0.92	24	32	499	8
7.05	-0.863	16	36	386	12
7.05	-0.863	20	36	300	8
7.05	-0.863	24	36	344	8
7.05	-0.863	36	36	298	1
7.05	-0.867	16	36	201	16
7.05	-0.867	24	36	251	4
7.05	-0.867	36	36	361	2

Table 11: The naming scheme of the different combinations of β and am_0. The mass of am_π^∞ corresponds to the energy level from the largest lattice which is compatible with the infinite-volume extrapolation. We also give the value for af_π [225].

name	β	am_0	am_π^∞	af_π
non-resonant	6.9	-0.92	0.38634(98)	0.08271(58)
close-to-resonant	6.9	-0.863	0.2059(11)	0.0528(10)
resonant	6.9	-0.867	0.1481(13)	0.04629(64)

3.4.2 Vector Resonance Scattering

In this section, we present the results for the ten-dimensional channel. We have ensembles with three combinations for β and am_0 at different spatial volumes at our disposal, which are summarized in Table 10. In contrast to the last section where the physics of the different ensembles were comparable, we will see that the scattering properties differ drastically between these ensembles. This was already expected from the energy levels of the naive rho operator at rest, which yields values for $m_\rho/m_\pi \approx \{1.4;\ 1.8;\ 2.4\}$ at values of $\beta, am_0 = \{6.9, -0.92; 7.05, -0.863; 7.05, -0.837\}$, which we will label *non-resonant*, *close-to-resonant* and *resonant* respectively. They are summarized with the values for the infinite-volume pion mass and the pion decay constant [225] in Table 11. We will label the infinite volume pion mass which corresponds to the value at the largest lattice as m_π in the following. The non-resonant case has the same values for β and am_0 as one of the ensembles in the last section. Here, the energy of the naive ρ operator at rest

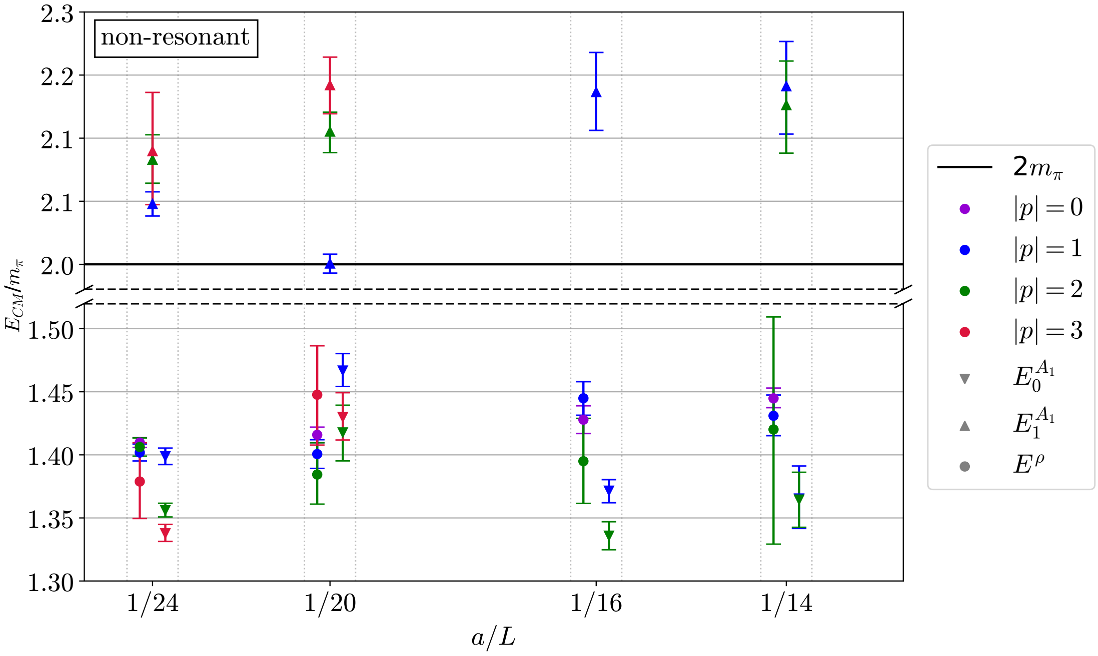

Figure 11: The energy levels in the ten-dimensional channel plotted against the inverse lattice extent in the non-resonant case with $\beta = 6.9$ and $am_0 = -0.92$. We split up the plot in two different energy ranges to improve visibility. The energy levels from the different irreps are slightly shifted in their x-position to guide the eye. Data points within the dotted lines correspond the the same spatial lattice extent. The energy levels from the irreps T_1, E and B_1 that were obtained by only employing a single ρ-operator are shown as circles and slightly shifted to the left. The energy levels from the A_1 irrep where we solve a 3×3 eigenvalue problem are shown as upward facing triangles for the excited state and lower facing triangles that are slightly shifted to the right for the ground state. We indicate the energy levels from operators with different total momentum by color. The two pion threshold is shown as a solid horizontal line.

can be identified with the mass of a stable vector meson. In the resonant case, this is not the case, and a proper Lüscher analysis has to be performed.

In order to investigate the properties of the ρ which carries $J^D = 1^-$ quantum numbers and spans the ten-dimensional irrep, we have to employ operators with the correct quantum numbers. To this end, we employ ρ-operators from Equation (3.37). We build two ρ operators with the gamma structures γ_i and $\gamma_4\gamma_i$. As discussed in Section 3.2.3, the antisymmetric combination of two pions carries the flavor quantum numbers of the ρ. We project the operators in different irreps of the LGs of O_h, which are determined by the total momentum employed. The two-pion operator with one pion carrying the entire momentum and the other at rest

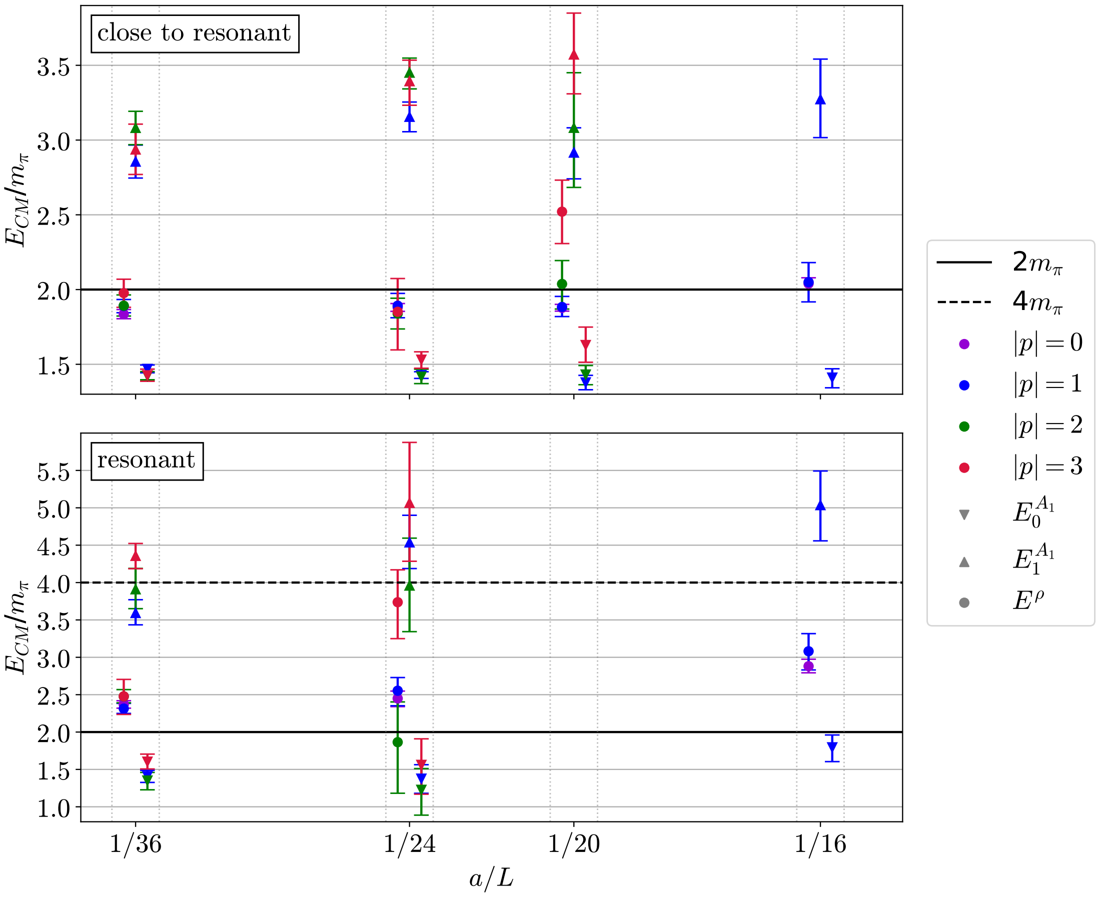

Figure 12: The energy levels in the ten-dimensional channel plotted against the inverse lattice extent with the same labeling as in Figure 11. Top panel: The close-to-resonant case with $\beta = 7.05$ and $am_0 = -0.683$. Bottom panel: The resonant case with $\beta = 7.05$ and $am_0 = -0.867$. The four pion threshold is shown as dashed horizontal line.

projects in the A_1 irrep. In this case, we build a 3×3 cross-correlation matrix and solve the eigenvalue problem introduced in Equation (3.62). In the other irreps, we only consider a single correlation function. This constitutes a systematic error that would be resolved by employing additional operators.

In Figure 11, we show the resulting energy levels plotted against the inverse lattice extent. We indicate the results from different irreps by different symbols and further shift them slightly in their x-position to guide the eye. All energy levels within the dotted lines were obtained from the same spatial lattice extent. In the non-resonant case, we find good agreement of the energy levels from the ρ operators labeled with E^ρ and the ground state of the A_1 irreps. They lie consistently below the two-pion threshold as expected from the naive rho mass estimate. We can identify these states as a stable ρ particle. The energy levels of the first excited state from the solutions of the eigenvalue problem lie slightly above the two-pion threshold and can be identified with two-pion scattering states. We can perform the Lüscher analysis with those energy levels similar to the 14-dimensional case.

The top panel of Figure 12 shows the result of the close-to-resonant ensemble with $\beta = 7.05$ and $am_0 = -0.863$. We see that the energy levels of the ρ operators, especially at the larger lattices, are slightly below or consistent with the two-pion threshold. However, the ground state from the A_1 irrep, drops below the two-pion threshold. Especially at the largest lattice, the errors are small, and this effect is statistically significant. One possible interpretation is that there is bound state present in the channel. In principle, every operator employed here should have an overlap with every state. Thus, at sufficiently large Euclidean times, we should be able to extract the ground state energy also from the ρ correlators. Since we were unable to do so, even at the largest lattice, the ρ-operators must have only small overlap with this ground state. This explanation is highly susceptible to the systematic error of not solving the eigenvalue problem for these irreps, which would allow for a proper analysis of the two states. The first excited states yield energy levels scattered in the elastic window.

This effect is present in the resonant case as well, but in a different form. The ground state energies extracted from the A_1 irrep are again significantly below threshold, albeit with larger errors. Unlike in the close-to-resonant case, the energy levels of the ρ-correlators are now above the two-pion threshold. We interpret these two states as a stable ground state and a resonant state, which will be backed by the results of the Lüscher analysis.

Next, we discuss the result of the Lüscher analysis in the ten-dimensional channel. These are obtained with the formulas for the phase shift in the different irreps given in Table 8. We analyze the non-resonant case using ERE just as in the 14-dimensional channel. We find the best description for the data points using a constant fit. In the close-to-resonant case, we have most of the points below the two-pion threshold where we cannot apply the Lüscher formalism. The only energy levels in the elastic window come from the first excited states and are very noisy. The results for the phase shift at most give a rough estimate for the cross section in this regime, which we do not show here explicitly. In the resonant case, we fit the phase shift resulting from the energy levels of the ρ-correlators to a Breit-Wigner shape and find satisfying agreement.

The Lüscher analysis is highly sensitive to large errors in the energy levels or correspondingly $q = \frac{pL}{2\pi}$, where p is the scattering momentum. It can easily happen

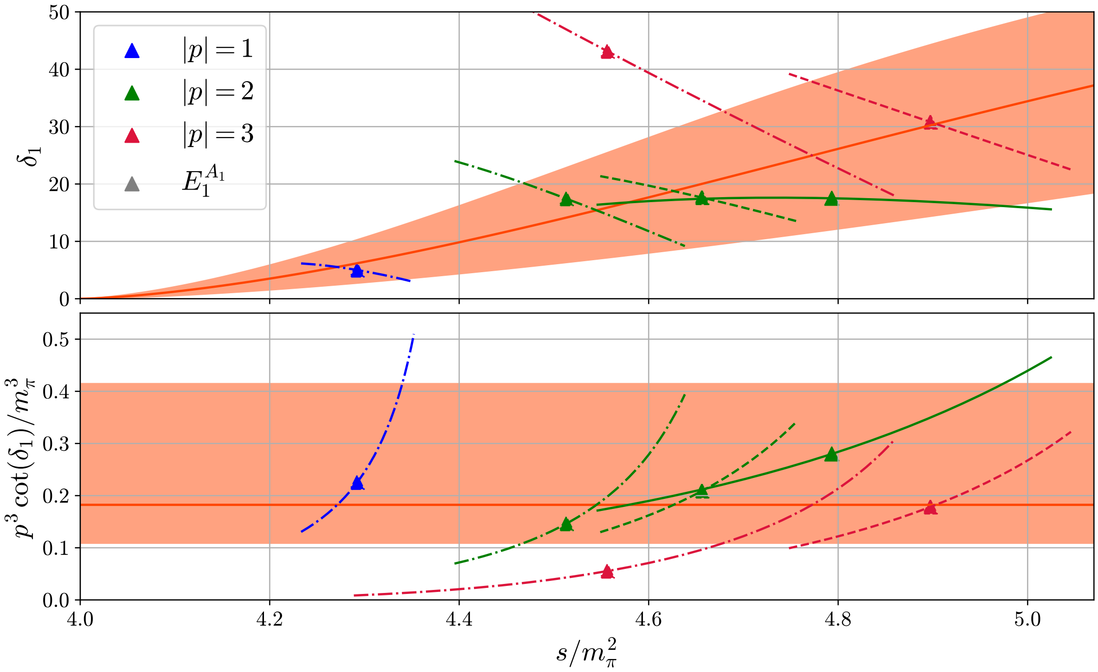

Figure 13: The results of the Lüscher analysis in the non-resonant ensembles. The p-wave phase shift is shown in the top panel. The left-hand side of p-wave ERE from Equation (3.13) is shown in the bottom panel. In both panels, the x-axis is the center-of-mass energy squared scaled with the mass of the pion. All data points are first excited states extracted from the variational analysis of the operators in the A_1 irrep. We indicate different momenta by color. The orange line and band show the median and error estimate of a constant fit to ERE.

that phase shift data points are compatible with all real numbers. We excluded data points with large error bars in the fit. We further exclude data points that are far away from where we expect the description to be valid, like at large energies for ERE or far away the resonance position in Breit-Wigner. In the following figures, we only show the data points that we included in the fits. The energy levels, phase shifts, and whether we include them in the fit are summarized for all ensembles in Appendix D. The upper panel of Figure 13 shows the phase shifts from the non-resonant ensembles. We do not see a hint for a resonance and therefore examine the data points using p-wave ERE given by Equation (3.13) which is shown in the lower panel. We find best agreement with a constant fit using zeroth-order ERE where the only parameter is the scattering length. The mean and error of the fit are shown by the orange line and band. We extract $a_1 m_\pi = -(1.76^{+0.11}_{-0.47})$ at $\chi^2/\text{d.o.f.} = 0.35$. The negative scattering length corresponds to an attractive interaction which could explain the emergence of a bound state when going to a

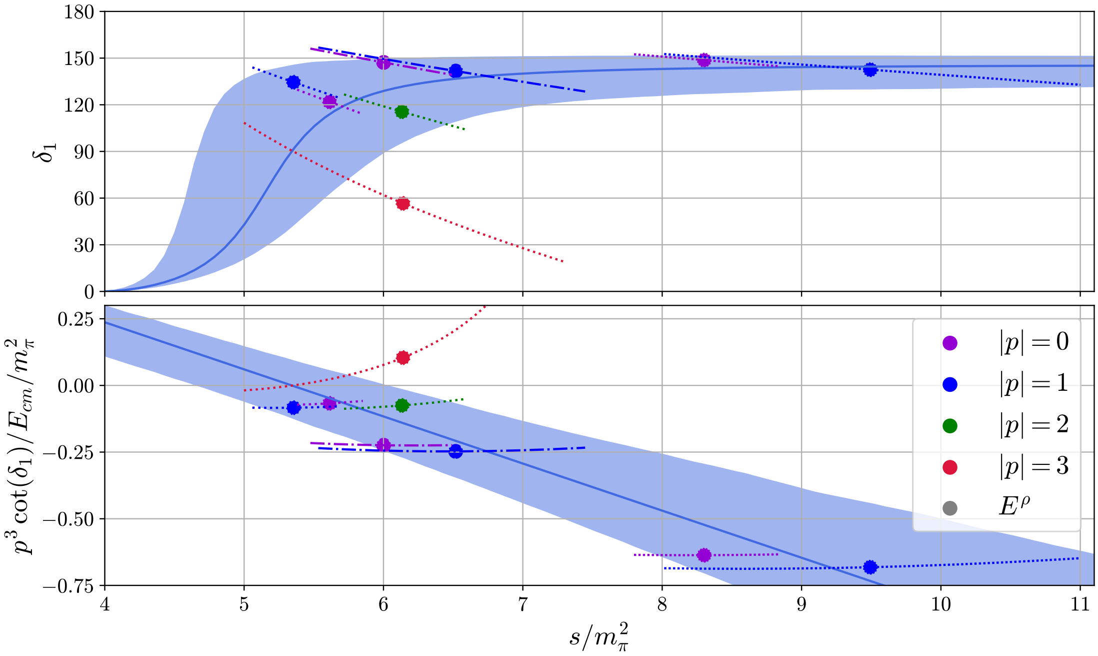

Figure 14: The results of the Lüscher analysis in the resonant ensembles. The p-wave phase shift is shown in the top panel. The y-axis of the bottom panel is motivated by Equation (3.121), as a Brei-Wigner shape results in a straight line in this plot. In both panels, the x-axis is the center-of-mass energy squared scaled with the mass of the pion. All data points are obtained from single ρ-operators in different irreps depending on the momentum employed. We indicate different momenta by color. The blue line and band show the median and error estimate of a fit to Breit-Wigner.

slightly different line of constant physics in the $\beta = 7.05$ cases. The higher order fits yield values for the scattering length that are compatible with the zeroth order fit, but the errors on the effective range or a potential second-order coefficient are larger than their value. It is expected that the higher-order fits do not perform well, as the data do not show any explicit s-dependence. From this we may calculate the partial-wave cross section via Equation (3.14) which we do in Section 3.1.3.

The upper panel of Figure 14 shows the results of the phase shift in the resonant ensemble. As we expect a resonance in this channel, we examine the data with a Breit-Wigner shape. Equation (3.18) can be rewritten as

$$\frac{p^3 \cot \delta_1}{E_{\text{cm}}} = \frac{6\pi}{g_{\rho\pi\pi}^2}(m_\rho^2 - s). \tag{3.121}$$

In this form, the Breit-Wigner shape takes a linear form, which motivates the y-axis of the bottom panel of Figure 14. Shown in the blue line and band is the mean and error of a linear fit to this equation. We have also tested the fit with the addition of a Blatt-Weisskopf [194] barrier factor like in Equation (3.20) but do not see an improvement. The linear fit using Equation (3.121) yields $m_R/m_\pi = 2.31^{+0.18}_{-0.10}$ and $g_{\rho\pi\pi} = 10.3^{+1.6}_{-1.0}$ at $\chi^2/\text{d.o.f.} = 1.5$. The KSRF relation predicts a value for $g_{\rho\pi\pi} \approx 27.3$, which deviates by a factor of 2.6. It should be mentioned that the fit failed when the two data points with the largest center-of-mass energy were excluded. Therefore, these results should be treated with caution. An improved analysis with including the variational analysis in all irreps and with more data points at lower values for the center-of-mass energy would greatly improve the credibility of the quoted values. It could also allow for an investigation of the influences of the three-to-two process, to which our data are not sensitive. In [114] and [194] the same analysis was performed in $SU(2)_c$ and $SU(3)_c$ and they find values of $g_{\rho\pi\pi} = 7.8$ and 5.76, respectively. This suggests that the resonance is broader in $Sp(4)_c$. This statement also has to be taken with a grain of salt, as the spectra of the investigated theories differ drastically and the bare parameters employed might result in different physics.

3.4.3 Cross Section

In dark matter phenomenology, the most interesting quantity is the cross section, especially at low energies, as dark matter is mostly assumed to be relativistic. In the following, we take a look at the cross section resulting from the scattering analyses performed in the two channels. The partial-wave cross section is obtained from the phase shift via Equation (3.12) which we can investigate at different center-of-mass energies given a description of the phase shift. We compare partial-wave cross sections from three representative cases. In Figure 15, we compare the cross sections from first-order s-wave ERE in the 14-dimensional channel, from zeroth-order p-wave ERE in the non-resonant case from the ten-dimensional channel, and from the Breit-Wigner shape in the resonant case, also in the ten-dimensional channel. We used data from $\beta = 6.9$ and $am_0 = -0.92$ in the first two cases and $\beta = 7.05$ and $am_0 = -0.867$ for the resonant case. Keep in mind that ensembles with different values for β and am_0 cannot be compared directly, as they correspond to different lines of constant physics. The line and bands show the median and an estimate of the 1σ error. The range on the x-axis is much larger than what is described by the lattice data. This assumes that the description with, for example, ERE is valid at all scales displayed here. In order to make the results more accessible, we have also fixed the scale by fixing the mass of the dark matter

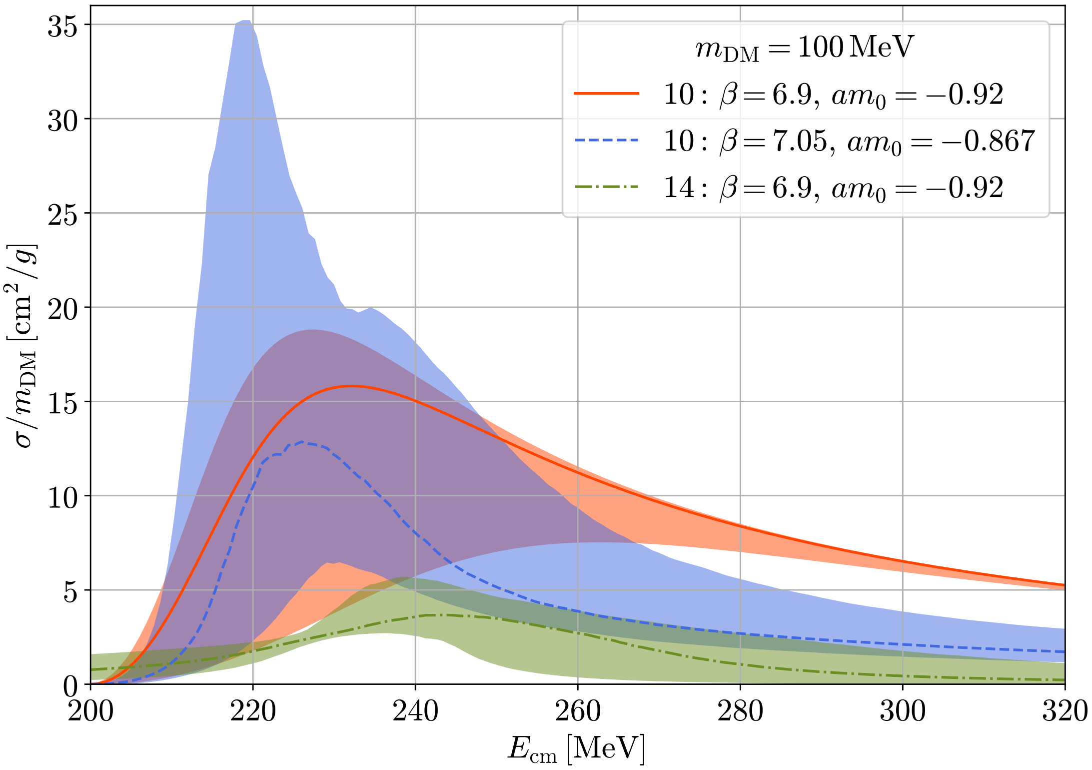

Figure 15: The cross section obtained from different fits to the phase shift plotted against the center-of-mass energy. Lines and bands indicate median and error. The green curve is obtained from a leading order s-wave ERE fit to the $\beta = 6.9$ and $am_0 = -0.92$ data in the 14-dimensional channel. The orange curve is obtained from a constant fit to p-wave ERE to the data of the non-resonant ensemble corresponding to the same values of β and am_0. The blue curve is obtained from a fit to Breit-Wigner to the data of the resonant ensemble with $\beta = 7.05$ and $am_0 = -0.867$. Note, that the different curves indicate different partial waves and lines of constant physics. Further, the fit to the phase shift is extrapolated to values of $E_{\rm cm}$ where we do not have lattice data. The pion mass is fixed to $m_{\rm DM} = 100\,\text{MeV}$ in order to provide units on the axes.

candidate to $m_{\rm DM} = 100\,\text{MeV}$ which gives rise to the units attached to the axes. As expected, we see that the cross section at very low energies is dominated by s-wave. Although this looks like only a small part of the full cross section, it basically describes all non-relativistic scattering. When we go to larger center-of-mass energies, which correspond to larger relative velocities of the scattering particles, the p-wave cross section starts to dominate. We see that the resonance yields the largest values for the cross section.

The dominance of the s-wave channel for the phenomenology of dark matter

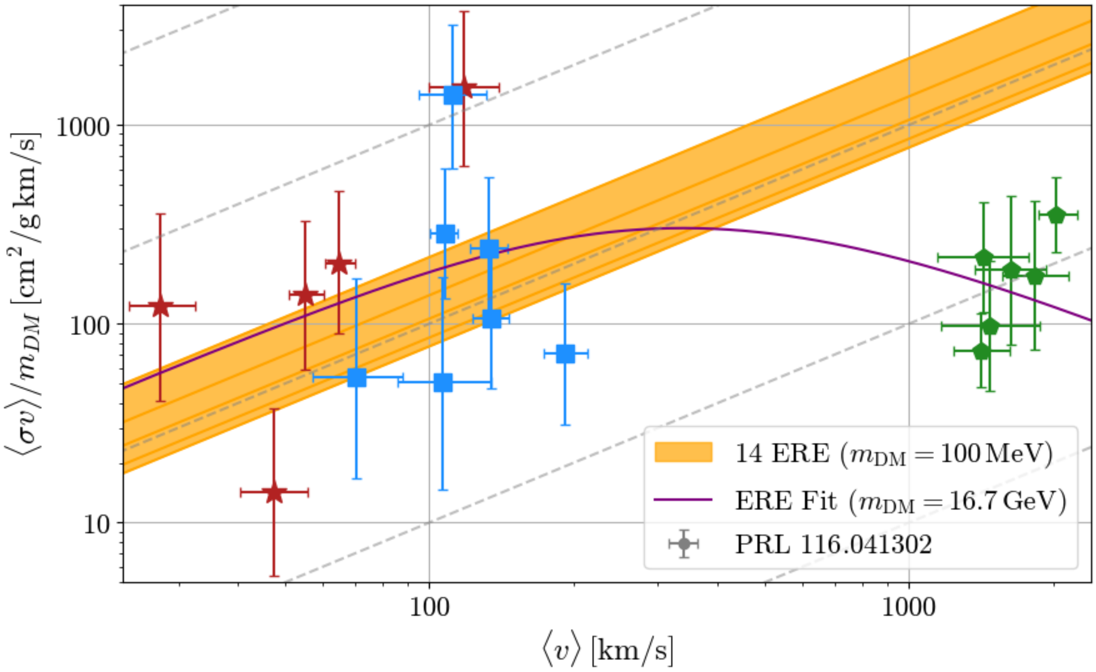

Figure 16: The velocity-weighted cross section $\langle \sigma v \rangle / m_{\mathrm{DM}}$ plotted against the data points from [46]. Different symbols and colors that relate to different astronomical objects (red stars - dwarf galaxies, blue squares - low surface brightness, green pentagons - galaxy clusters). The y-axis is calculated with Equation (3.21) and scales like $1/m_{\mathrm{DM}}^3$. Lines of constant cross section are shown in grey, dashed lines. The yellow band is an error estimate containing all of our ensembles as an individual line. The purple line shows a fit to the data from [103].

becomes particularly clear when we calculate the velocity-weighted cross section that was introduced in Equation (3.21). This quantity received a lot of attention in the context of self-interacting dark matter. The data points in Figure 16, are obtained by fitting the results of halo simulations to astronomical data [46]. Different colors and markers indicate data from astronomical objects of different sizes. Stars are dwarf galaxies, squares are low surface brightness galaxies, and pentagons are galaxy clusters. With increasing size of the objects, the mean relative velocity increases. In this way, they can be used to probe different mean relative velocities. The data raised the question whether a hypothetical dark matter self-interaction could be velocity dependent in the non-relativistic regime.[10] [103] extracted the first-order ERE parameters in s-wave that best describe the data. The results are $a_0 = 22.2\,\mathrm{fm}$, $r_0 = -2.59 \times 10^{-3}\,\mathrm{fm}$, and $m_{\mathrm{DM}} = 16.7\,\mathrm{GeV}$. This results in a value of $a_0 m_{\mathrm{DM}} = 1879$, which is roughly three orders of magnitude larger than

---

[10] A constant cross section in the plot results in a line parallel to the gray dashed lines.

our result on the s-wave scattering-length. As a result, our data cannot describe the bending of the purple curve. The results in the 14-dimensional channel for the s-wave cross section from ERE are shown for a dark matter mass of 100 MeV as the yellow band, where each line corresponds to one combination of β and am_0. This band can be shifted up and down by considering a different dark matter mass as the y-axis scales like $1/m_{\mathrm{DM}}^3$. For the non-relativistic velocities considered here, the s-wave cross section described by our results in the 14-dimensional is basically constant. As a result, the velocity-weighted cross section $\langle \sigma v \rangle / m_{\mathrm{DM}}$ takes an analytical form proportional to $\langle v \rangle$. The same holds for the p-wave cross sections, which are proportional to $p^4 \propto v^4$ close to threshold and the resulting velocity-weighted cross section is proportional to $\langle v \rangle^5$ which does not describe the data at all. We conclude that the p-wave cross section has no relevant contribution at these non-relativistic velocities. We do not see effects that can be traced back to the presence of the three-to-two process in the channel.

3.5 Three-to-Two Scattering

The main motivation for $Sp(4)_c$ with $N_f = 2$ fundamental fermions as a dark matter candidate is its minimal realization of SIMP dark matter, in which the 5-point vertex involving all five dark pions introduced in Equation (1.41) takes on the task of the cannibalization process. The non-perturbative determination of the amplitude of such a process would be a novelty and, therefore, an important cross-check for effective theories working with the WZW term. Furthermore, such a calculation would also be a major step in solidifying the three-particle quantization condition. Our dark matter theory showcases the perfect testing ground for this endeavor, as the scattering channels involved in the WZW term are less complex compared to QCD. Although no lattice results are available yet, we will summarize the steps necessary to obtain them and provide an overview of the special features of this theory. On the lattice, three-particle scattering can be investigated with the three-particle quantization condition, which reads

$$\det_{\vec{k}',l',m';\vec{k},l,m} \left[\mathcal{K}_{df,3}(E^*) + F_3(E, \vec{P}, L)^{-1} \right] = 0. \tag{3.122}$$

We refer to the literature for details [195–198, 226]. Like in the two-particle case, it is possible to relate finite-volume energy levels to infinite-volume scattering parameters using this formula. The central object is the three-particle $\mathcal{K}$-matrix, which contains all possible subprocesses. The great advantage of this theory is that the ten-dimensional channel is the only channel shared by the two-pion and three-pion states. Furthermore, there is only one two-pion subprocess involved, as can be seen from the tensor product in Equation (3.28). This is in contrast to $N_f = 2$ flavor QCD, where only the maximal and singlet three-pion channel can be built exclusively from a single two-pion subchannel [227]. The subprocess is described by the results presented in Section 3.4.2. The $\mathcal{K}$-matrix can be written as

$$\mathcal{K}_{df,3} = \begin{pmatrix} \mathcal{K}_{22} & \mathcal{K}_{23} \\ \mathcal{K}_{32} & \mathcal{K}_{33} \end{pmatrix}, \tag{3.123}$$

where the off-diagonal entries encode three-to-two scattering processes. For the investigation of three-to-two scattering in this theory, one could proceed as follows. $\mathcal{K}_{23} = \mathcal{K}_{32}$ can be identified with the WZW amplitude which can be obtained from Equation (1.41) as

$$\begin{aligned} K_{\text{WZW}} = \frac{2N_c}{10\sqrt{2}\pi^2 f_\pi^5} \epsilon^{\mu\nu\rho\sigma} \big(& p_{1\mu}p_{2\nu}p_{3\rho}p_{4\sigma} - p_{1\mu}p_{2\nu}p_{3\rho}p_{5\sigma} + p_{1\mu}p_{2\nu}p_{4\rho}p_{5\sigma} \\ & - p_{1\mu}p_{3\nu}p_{4\rho}p_{5\sigma} + p_{2\mu}p_{3\nu}p_{4\rho}p_{5\sigma} \big) \end{aligned} \tag{3.124}$$

The WZW amplitude to leading order does not contain any LECs but instead is fixed by the value of N_c. In order to falsify this prediction, one might treat the coefficient as a free parameter instead and check whether the fit to the scattering analysis will yield the coefficient given by ChPT. $\mathcal{K}_{22}$ describes the possible processes in the two-particle channel. Depending on the ensemble, this could either be described by ERE or Breit-Wigner. For simplicity, $\mathcal{K}_{33}$ could be set to zero or a constant. This would result in three to five parameters that need to be fitted from the lattice data, which in turn requires a large number of energy levels. In order to be sensitive to three-particle scattering, at least some of the energy level should be greater than $3m_\pi$. This not only requires a good understanding of the spectrum, but also the inclusion of large operator basis. The larger energy levels are also more affected by discretization artifacts which require the use of fine lattices. Furthermore, like in the two-particle case, the quantization condition requires exponential terms $\propto e^{-m_\pi L}$ to be negligible, and the temporal extent to be infinite. Lastly, the formalism also requires the use of a cutoff function H whose parametrization might introduce systematic effects.

3.5.1 Particle Kinematics and Partial-wave Decomposition

In order to deal with the WZW amplitude in the three-particle quantization condition, we have to understand the kinematics of a three-to-two process with three incoming particles and two outgoing particles that, in our case, all have the same mass m_π. A five-point function is described by five vectors $p_i = (\omega_i, \vec{p}_i)$ with 20 parameters. The particles are on-shell and the energy is given by the same mass m_π for all five momenta,

$$\omega_i = \sqrt{m_\pi^2 + \vec{p}_i^{\,2}}, \tag{3.125}$$

which fixes the five energy components leaving only the spatial momentum vectors independent. The generators of the Poincaré group further eliminate ten dependencies, which corresponds to ensuring translation and Lorentz invariance. As a result, the kinematics of a five-point function can be described in terms of five Lorentz invariants. In this special case, a convenient choice for the five Lorentz invariants is s_{12}, s_{23}, s_{34}, s_{45}, s_{51}, where $s_{ij} = (p_i - p_j)^2$. The center-of-mass energy squared is given by $s = (p_1 + p_2 + p_3)^2 = (p_4 + p_5)^2$. In order to work with the three-particle quantization condition, we have to work in the frame given by the total momentum $\vec{P}_{\text{tot}}$. The three-particle state is then split into a *spectator* particle and a *dimer* containing the remaining two particles. Because we work with degenerate pions, all possible dimers are equivalent. The index $\vec{k}$ in Equation (3.122) refers to the spectator momentum, which is also discretized on the lattice. It is convenient to label the momenta of the incoming state in terms of a *spectator* $\vec{k}$ and *dimer* $\vec{a}$ and $\vec{b}$ and the momenta of the outgoing state $\vec{c}$ and $\vec{d}$. This results in the total momentum being

$$\vec{P}_{\text{tot}} = \vec{k} + \vec{a} + \vec{b} = \vec{c} + \vec{d}. \tag{3.126}$$

The incoming and outgoing states have to be expanded in partial waves. For the outgoing state, we can expand the momenta $\vec{c}$ and $\vec{d}$ in the center-of-mass frame given by $\vec{P}_{\text{tot}}$. The incoming state is expanded in the center-of-mass frame of the dimer, which depends on the total momentum $\vec{P}_{\text{tot}}$ and the spectator momentum $\vec{k}$. The WZW amplitude from Equation (3.124) depends on the five momenta p_i

for which

$$\vec{d} = \vec{P}_{\text{tot}} - \vec{c}, \tag{3.127}$$

$$\omega_c = \sqrt{\vec{c}^2 + m_\pi^2}, \tag{3.128}$$

$$\omega_d = \sqrt{\left(\vec{P} - \vec{c}\right)^2 + m_\pi^2}, \tag{3.129}$$

$$E = \omega_c + \omega_d, \tag{3.130}$$

in the outgoing state, and

$$\vec{b} = \vec{P}_{\text{tot}} - \vec{k} - \vec{a}, \tag{3.131}$$

$$\omega_k = \sqrt{\vec{k}^2 + m_\pi^2}, \tag{3.132}$$

$$\omega_a = \sqrt{\vec{a}^2 + m_\pi^2}, \tag{3.133}$$

$$\omega_b = \sqrt{\left(\vec{P} - \vec{k} - \vec{a}\right)^2 + m_\pi^2}, \tag{3.134}$$

$$E = \omega_k + \omega_a + \omega_b, \tag{3.135}$$

in the incoming state. Now, we can define the four-vector and center-of-mass energy of the dimer as

$$P_{\text{dimer}} = (E - \omega_k,\, \vec{P}_{\text{tot}} - \vec{k}), \tag{3.136}$$

$$E^{*2}_{\text{dimer}} = (P_{\text{dimer}})^2 = (E - \omega_k)^2 - (\vec{P}_{\text{tot}} - \vec{k})^2. \tag{3.137}$$

We denote quantities in the center-of-mass frame of the dimer by *. The boost to the center-of-mass frame of the dimer is obtained by a Lorentz transformation with

$$\Lambda^\mu{}_\nu(\vec{\beta}) = \begin{pmatrix} \gamma & -\gamma\beta_j \\ -\gamma\beta_i & \delta_{ij} + (\gamma - 1)\frac{\beta_i\beta_j}{\beta^2} \end{pmatrix}, \tag{3.138}$$

where

$$\vec{\beta} = \frac{\vec{P}_{\text{tot}} - \vec{k}}{E - \omega_k}, \tag{3.139}$$

$$\gamma = \frac{1}{\sqrt{1 - \vec{\beta}^2}}. \tag{3.140}$$

This yields

$$a^*_\mu = \Lambda^\nu_\mu(\vec{\beta})a_\nu = (\omega^*_a, \vec{a}^*) = |\vec{a}^*|(\tilde{\omega}^*_a, \hat{a}^*), \tag{3.141}$$

$$b^*_\mu = |\vec{a}^*|(\tilde{\omega}^*_a, -\hat{a}^*), \tag{3.142}$$

$$\omega^*_a = \tilde{\omega}^*_a\,|\vec{a}^*|, \tag{3.143}$$

$$|\vec{a}^*| = \sqrt{\frac{(E-\omega_k)^2 - (\vec{P}_{\text{tot}} - \vec{k})^2}{4} - m_\pi^2}, \tag{3.144}$$

where we have defined $\hat{a}^* = (\sin\theta\cos\phi,\, \sin\theta\sin\phi,\, \cos\theta)$ as the unit vector of $\vec{a}^*$ in terms of the angles θ and ϕ. Note that neither $\tilde{\omega}^*_a$ nor $|\vec{a}^*|$ depend on these angles. Equivalently, the momenta $\vec{c}$ and $\vec{d}$ are expressed in terms of θ' and ϕ'. The partial-wave expansion of the WZW amplitude is then given by

$$K^{\vec{P}_{\text{tot}}}_{\vec{k};l',m';l,m} = \frac{1}{4\pi}\int\int d\Omega' d\Omega\, Y^*_{l',m'}(\theta',\phi') K_{\text{WZW}}(\vec{P}_{\text{tot}}, \vec{k}, \theta, \phi, \theta', \phi') Y_{l,m}(\theta,\phi). \tag{3.145}$$

$Y_{l,m}(\theta,\phi)$ are the spherical harmonics. This expansion can be used to build the quantization condition, including the WZW term. Given finite-volume energy levels from lattice calculation, we can test the ChPT prediction non-perturbatively.

Chapter 4

Summary

In this thesis, we have investigated non-perturbative signatures of SIMP dark matter models using lattice field theory. They describe an alternative relic density mechanism and address the small-scale structure problems. In Chapter 2, we investigated the effect of dark matter described by G_2 QCD on a neutron star. The sign problem is absent in this theory, allowing for a non-perturbative calculation of the equation of state at finite densities using lattice field theory. We supplement the dark matter equation of state with model-agnostic equations of state for ordinary matter and find that G_2 dark matter can be accommodated in neutron stars, altering the macroscopic parameters like the mass, radius, and tidal deformability significantly. Although we do not find any signatures that can directly be traced back to the non-perturbative nature of the equation of state, this verifies that SIMP dark matter can be considered in the investigation of mixed or exotic stars.

In Chapter 2, we have introduced $Sp(4)_c$ gauge theory with $N_f = 2$ fundamental fermions as the minimal realization of the SIMP mechanism. We supplement existing lattice spectroscopy data with two-particle scattering analyses using the Lüscher formalism. In the maximal channel, we find a good description of the low-energy s-wave cross section by first-order ERE across multiple ensembles. We confirm the validity of ChPT at relatively large pion masses. The other channel contains a vector meson as well as the three-to-two process that motivates the model as a SIMP candidate. We have employed three ensembles which showcase the emergence of a resonance in this channel. In the non-resonant ensemble, we find a good description of the data using zeroth-order p-wave ERE. Going to the resonant ensemble, we find a bound state below the two-pion threshold that can be identified as a stable vector particle. Additionally, we find a decent description of the resonance in one of the ensembles using a Breit-Wigner form that grants access to the position and the width of the resonance. Finally, we have investigated the cross section in both channels and find that the non-relativistic cross section is dominated by s-wave scattering in the maximal channel. At larger energies, the p-wave cross section in the ten-dimensional channel becomes relevant, and we find the maximal value at the resonance position. The straightforward extension of this work is the investigation of the cannibalization process described by the WZW term in ChPT using the three-particle scattering formalism. We have discussed the kinematics of the amplitude and how it can be accommodated in the three-particle quantization condition.

In summary, SIMP dark matter is an interesting dark matter candidate, addressing the small-scale structure problems and inheriting an alternative relic density mechanism. We have investigated SIMP theories in the settings described above for the first time using non-perturbative methods, which is necessary due to their UV motivation using non-Abelian gauge theories. The two models considered are compatible with the constraints and therefore pass this test. This confirms SIMPs as valid candidates for dark matter.

Appendix A

Conventions

In this work, we use hermitian, involutory, and Euclidean gamma matrices as defined in [119].

$$\{\gamma_\mu, \gamma_\nu\} = 2\delta_{\mu\nu}\mathbb{1} \tag{A.1}$$

$$\gamma_5 = \gamma_1\gamma_2\gamma_3\gamma_4 \tag{A.2}$$

$$\gamma_\mu = \gamma_\mu^\dagger = \gamma_\mu^{-1} \tag{A.3}$$

$\gamma_5^2 = \mathbb{1}$ and γ_5 commutes with all other gamma matrices. The Dirac operator and its inverse are γ_5-hermitian $\gamma_5 D \gamma_5 = D^\dagger$. We use the chiral representation in which the gamma matrices can be expressed in terms of the Hermitian and traceless Pauli matrices.

$$\sigma_1 = \begin{pmatrix} 0 & 1 \\ 1 & 0 \end{pmatrix} \quad \sigma_2 = \begin{pmatrix} 0 & -i \\ i & 0 \end{pmatrix} \quad \sigma_3 = \begin{pmatrix} 1 & 0 \\ 0 & -1 \end{pmatrix} \tag{A.4}$$

In Section 1.2.3, we introduce $\tau_\nu = (-i\sigma_j, \mathbb{1}_2)$ and $\bar{\tau}_\nu = (i\sigma_j, \mathbb{1}_2)$ for which $\bar{\tau} = \sigma_2\tau_\nu^T\sigma_2$ and $\tau = \sigma_2\bar{\tau}_\nu^T\sigma_2$. We further define $\sigma_4 = \mathbb{1}_2$. The γ matrices are then defined as

$$\gamma_\mu = \begin{pmatrix} 0 & \tau_\mu \\ \bar{\tau}_\mu & 0 \end{pmatrix}, \quad \gamma_5 = \begin{pmatrix} \mathbb{1}_2 & 0 \\ 0 & -\mathbb{1}_2 \end{pmatrix}, \tag{A.5}$$

or

$$\gamma_1 = \begin{pmatrix} 0 & 0 & 0 & -i \\ 0 & 0 & -i & 0 \\ 0 & i & 0 & 0 \\ i & 0 & 0 & 0 \end{pmatrix}, \quad \gamma_2 = \begin{pmatrix} 0 & 0 & 0 & -1 \\ 0 & 0 & 1 & 0 \\ 0 & 1 & 0 & 0 \\ -1 & 0 & 0 & 0 \end{pmatrix}, \quad \gamma_3 = \begin{pmatrix} 0 & 0 & -i & 0 \\ 0 & 0 & 0 & i \\ i & 0 & 0 & 0 \\ 0 & -i & 0 & 0 \end{pmatrix},$$
$$\gamma_4 = \begin{pmatrix} 0 & 0 & 1 & 0 \\ 0 & 0 & 0 & 1 \\ 1 & 0 & 0 & 0 \\ 0 & 1 & 0 & 0 \end{pmatrix}, \quad \gamma_5 = \begin{pmatrix} 1 & 0 & 0 & 0 \\ 0 & 1 & 0 & 0 \\ 0 & 0 & -1 & 0 \\ 0 & 0 & 0 & -1 \end{pmatrix}, \tag{A.6}$$

written explicitly in four-index notation. We define the charge conjugation matrix through the relation

$$C\gamma_\mu C^{-1} = -\gamma_\mu^T. \tag{A.7}$$

In the chiral representation the charge conjugation matrix can be identified as

$$C = i\gamma_2\gamma_4, \tag{A.8}$$

and obeys

$$C = C^\dagger = C^{-1} = -C^T = -C^*. \tag{A.9}$$

The charge conjugation matrix acting on two-index Weyl spinors is the second Pauli matrix σ_2. Finally, we define the projection operators as

$$P_L = \frac{1}{2}(1-\gamma_5) = \begin{pmatrix} 0 & 0 \\ 0 & \mathbb{1}_2 \end{pmatrix}, \qquad P_R = \frac{1}{2}(1+\gamma_5) = \begin{pmatrix} \mathbb{1}_2 & 0 \\ 0 & 0 \end{pmatrix}. \tag{A.10}$$

They obey

$$P_L\gamma_5 = \gamma_5 P_L = -P_L \tag{A.11}$$
$$P_R\gamma_5 = \gamma_5 P_R = P_R \tag{A.12}$$
$$P_{L/R}\gamma_\mu = \gamma_\mu P_{R/L}, \tag{A.13}$$

and project out the left- and right-handed components of Dirac spinors.

$$(0, \psi_L) = P_L \psi \tag{A.14}$$

$$(\psi_R, 0) = P_R \psi \tag{A.15}$$

$$(0, \psi_R^\dagger) = \bar{\psi} P_L \tag{A.16}$$

$$(\psi_L^\dagger, 0) = \bar{\psi} P_R \tag{A.17}$$

We clarify that $\psi_{L/R}$ and $\psi_{L/R}^\dagger$ are two-index Weyl spinors that carry two indices. Next, we would like to introduce the conventions regarding $Sp(4)$. In this work, we deal with two $Sp(4)$ symmetries which are related to the local gauge symmetry and the resulting global flavor symmetry. The defining property of the group elements of $Sp(4)$ is that they leave the antisymmetric matrix invariant

$$\Sigma = E = \begin{pmatrix} 0 & \mathbb{1}_2 \\ -\mathbb{1}_2 & 0 \end{pmatrix}, \tag{A.18}$$

where we refer to the same matrix as Σ if it acts in color space and F or E for $N_f = 2$ if it acts in flavor space. It obeys the following properties.

$$E = -E^\dagger = -E^{-1} = -E^T = E^* \tag{A.19}$$

Most of the time, the color matrix Σ occurs together with the charge conjugation matrix. As they act in different spaces, they always commute. Together, they obey

$$(C\Sigma) = -(C\Sigma)^\dagger = -(C\Sigma)^{-1} = (C\Sigma)^T = -(C\Sigma)^*. \tag{A.20}$$

The same holds for σ_2. They can also be used to transpose the quark propagator with the following identity [118].

$$(C\Sigma)^{-1} S_q^T(y|x)(C\Sigma) = S_q(x|y) \tag{A.21}$$

$Sp(4)$ is a subgroup of $SU(4)$ its fundamental generators can be written as a subset of the fundamental generators of $SU(4)$. We can obtain a basis of Hermitian matrices by the following definitions [85, 115, 228]

$$\begin{aligned} &B_1 = \sigma_4,\ B_2 = i\sigma_4,\ B_3 = \sigma_3,\ B_4 = i\sigma_3, \\ &B_5 = \sigma_1,\ B_6 = i\sigma_1,\ D_4 = \sigma_2,\ D_5 = i\sigma_2. \end{aligned} \tag{A.22}$$

Using the normalization $\mathrm{Tr}[T^aT^b] = \frac{1}{2}\delta^{ab}$, the $SU(4)$ generators are then given by

$$X^a = \frac{1}{2\sqrt{2}}\begin{pmatrix}\sigma_a & 0\\ 0 & \sigma_a^T\end{pmatrix},\ \ a = 1, ..., 3 \tag{A.23}$$

$$X^a = \frac{1}{2\sqrt{2}}\begin{pmatrix}0 & D_a\\ D_a^\dagger & 0\end{pmatrix},\ \ a = 4, 5 \tag{A.24}$$

$$S^a = \frac{1}{2\sqrt{2}}\begin{pmatrix}\sigma_a & 0\\ 0 & -\sigma_a^T\end{pmatrix},\ \ a = 1, ..., 4 \tag{A.25}$$

$$S^a = \frac{1}{2\sqrt{2}}\begin{pmatrix}0 & B_{a-4}\\ B_{a-4}^\dagger & 0\end{pmatrix},\ \ a = 5, ..., 10, \tag{A.26}$$

or explicitly

$$\begin{aligned}
X^1 &= \tfrac{1}{2\sqrt{2}}\begin{pmatrix}0&1&0&0\\1&0&0&0\\0&0&0&1\\0&0&1&0\end{pmatrix} &
X^2 &= \tfrac{1}{2\sqrt{2}}\begin{pmatrix}0&-i&0&0\\i&0&0&0\\0&0&0&i\\0&0&-i&0\end{pmatrix} &
X^3 &= \tfrac{1}{2\sqrt{2}}\begin{pmatrix}1&0&0&0\\0&-1&0&0\\0&0&1&0\\0&0&0&-1\end{pmatrix}\\
X^4 &= \tfrac{1}{2\sqrt{2}}\begin{pmatrix}0&0&0&-i\\0&0&i&0\\0&-i&0&0\\i&0&0&0\end{pmatrix} &
X^5 &= \tfrac{1}{2\sqrt{2}}\begin{pmatrix}0&0&0&1\\0&0&-1&0\\0&-1&0&0\\1&0&0&0\end{pmatrix} &
S^1 &= \tfrac{1}{2\sqrt{2}}\begin{pmatrix}0&0&-i&0\\0&0&0&-i\\i&0&0&0\\0&i&0&0\end{pmatrix}\\
S^2 &= \tfrac{1}{2\sqrt{2}}\begin{pmatrix}0&0&0&-i\\0&0&-i&0\\0&i&0&0\\i&0&0&0\end{pmatrix} &
S^3 &= \tfrac{1}{2\sqrt{2}}\begin{pmatrix}0&-i&0&0\\i&0&0&0\\0&0&0&-i\\0&0&i&0\end{pmatrix} &
S^4 &= \tfrac{1}{2\sqrt{2}}\begin{pmatrix}0&0&-i&0\\0&0&0&i\\i&0&0&0\\0&-i&0&0\end{pmatrix}\\
S^5 &= \tfrac{1}{2}\begin{pmatrix}0&0&1&0\\0&0&0&0\\1&0&0&0\\0&0&0&0\end{pmatrix} &
S^6 &= \tfrac{1}{2\sqrt{2}}\begin{pmatrix}0&0&0&1\\0&0&1&0\\0&1&0&0\\1&0&0&0\end{pmatrix} &
S^7 &= \tfrac{1}{2}\begin{pmatrix}0&0&0&0\\0&0&0&1\\0&0&0&0\\0&1&0&0\end{pmatrix}\\
S^8 &= \tfrac{1}{2\sqrt{2}}\begin{pmatrix}0&1&0&0\\1&0&0&0\\0&0&0&-1\\0&0&-1&0\end{pmatrix} &
S^9 &= \tfrac{1}{2\sqrt{2}}\begin{pmatrix}1&0&0&0\\0&-1&0&0\\0&0&-1&0\\0&0&0&1\end{pmatrix} &
S^{10} &= \tfrac{1}{2\sqrt{2}}\begin{pmatrix}1&0&0&0\\0&1&0&0\\0&0&-1&0\\0&0&0&-1\end{pmatrix},
\end{aligned} \tag{A.27}$$

where X^i are exclusive $SU(4)$ generators and define the coset $SU(4)/Sp(4)$. They obey

$$X^i = E(X^i)^T E. \tag{A.28}$$

S^i are the 10 generators of the fundamental representation of $Sp(4)$ for which the following applies.

$$S^i = -E(S^i)^T E. \tag{A.29}$$

The totally antisymmetric structure constants of $SU(4)$ are defined by $[T^a, T^b] = i f^{abc} T^c$. All nonzero structure constants are

$$f^{1,2,14} = f^{2,3,13} = f^{2,4,6} = f^{1,3,7} = \frac{1}{\sqrt{2}} \tag{A.30}$$

$$f^{1,3,8} = f^{1,5,9} = f^{3,4,11} = f^{4,5,15} = -\frac{1}{\sqrt{2}} \tag{A.31}$$

$$f^{1,4,10} = f^{2,5,10} = f^{2,5,12} = -f^{1,4,12} = \frac{1}{2}. \tag{A.32}$$

The generators $\{X^1, X^2, X^3, X^4, S^7, S^8\}$ meet the criteria for $SO(4)$

$$-G_j G_j^T = \delta_{ij}, \tag{A.33}$$

and may be used as a basis. Occasionally, it is convenient to use other bases. The basis in Equation (A.27) is Hermitian and using Equation (3.38) results in the following pion quintuplet [115]

$$\Pi_i = \frac{1}{2\sqrt{2}} \begin{pmatrix} \pi^A - \pi^B \\ i(\pi^A + \pi^B) \\ \sqrt{2}\pi^C \\ i(\pi^D + \pi^E) \\ \pi^D - \pi^E \end{pmatrix}, \tag{A.34}$$

The basis we introduce in the following is equivalent to the basis that results in the charge eigenstates of the pions $\pi^\pm$ and π^0 in $SU(2)$. We obtain this basis by the following definitions [85]

$$\begin{aligned}
&X^A = \frac{1}{\sqrt{2}}\left(X^1 - iX^2\right) && X^B = \frac{1}{\sqrt{2}}\left(X^1 + iX^2\right) \qquad X^C = X^3 \\
&X^D = \frac{1}{\sqrt{2}}\left(X^5 - iX^4\right) && X^E = \frac{1}{\sqrt{2}}\left(X^5 + iX^4\right) \\
&S^A = \frac{1}{\sqrt{2}}\left(\sqrt{2}S^{10} - i\left(S^6 + S^9\right)\right) && S^B = \frac{1}{\sqrt{2}}\left(S^{11} - iS^7\right) \\
&S^C = \frac{1}{\sqrt{2}}\left(S^{13} - iS^8\right) && S^D = \frac{1}{\sqrt{2}}\left(\sqrt{2}S^{12} - i\left(S^6 - S^9\right)\right) \\
&S^E = \frac{1}{\sqrt{2}}\left(-\sqrt{2}S^{10} - i\left(S^6 + S^9\right)\right) && S^F = \frac{-1}{\sqrt{2}}\left(S^{11} + iS^7\right) \\
&S^G = \frac{1}{\sqrt{2}}\left(-\sqrt{2}S^{12} - i\left(S^6 - S^9\right)\right) && S^H = \frac{1}{\sqrt{2}}\left(S^{13} + iS^8\right) \\
&S^I = S^{14} && S^J = S^{15}.
\end{aligned} \tag{A.35}$$

The generators in this basis are not Hermitian but are more sparse, resulting in smaller bilinears. Therefore, it is more convenient for operator building and Wick contraction, as it results in fewer terms. The resulting pion quintuplet was given in Equations (3.39)–(3.43).

Appendix B

Additional Operators

In this appendix, we want to provide additional operators that were not employed in this work, but will be helpful for the analysis of three-to-two scattering. This will include a $\rho\pi$ operator and a $\pi\pi\pi$ operator. To this end, it is useful to explicitly write the vector decuplet. Using Equation (3.36) with the basis given in Equation (A.35) yields [85]

$$\begin{aligned}
\rho^A &= u^T C\Sigma\gamma_\mu P_L u & \rho^B &= u^T C\Sigma\gamma_\mu d \\
\rho^C &= \bar{d}\gamma_\mu u & \rho^D &= d^T C\Sigma\gamma_\mu P_L d \\
\rho^E &= \bar{u}\gamma_\mu C\Sigma P_L \bar{u}^T & \rho^F &= \bar{u}\gamma_\mu C\Sigma \bar{d}^T \\
\rho^G &= \bar{d}\gamma_\mu C\Sigma P_L \bar{d}^T & \rho^H &= \bar{u}\gamma_\mu d \\
\rho^I &= \frac{1}{\sqrt{2}}(\bar{u}\gamma_\mu u - \bar{d}\gamma_\mu d) & \rho^J &= \frac{1}{\sqrt{2}}(\bar{u}\gamma_\mu u + \bar{d}\gamma_\mu d).
\end{aligned} \tag{B.1}$$

Here, we can identify the operators ρ^H, ρ^C, and ρ^I as the subset that corresponds to the Standard Model bilinears. The projection of $\mathbf{5}\otimes\mathbf{5}\otimes\mathbf{5}$ into the ten-dimensional representation is given by the totally antisymmetric combination of all three indices of the pions [201]. This can be realized as

$$O^{\mathbf{10}}_{\pi\pi\pi} = \pi^A\pi^B\pi^C - \pi^A\pi^C\pi^B + \pi^C\pi^A\pi^B - \pi^C\pi^B\pi^A + \pi^B\pi^C\pi^A - \pi^B\pi^A\pi^C. \tag{B.2}$$

There is a trick to obtain a $\rho\pi$-operator from this, for which we just need to realize that the $\pi\pi\pi$-operator can be constructed from antisymmetric two-pion states in the ten-dimensional irrep.

$$O^{\mathbf{10}}_{\pi\pi\pi} = -(\pi^A\pi^C - \pi^C\pi^A)\pi^B + (\pi^B\pi^C - \pi^C\pi^B)\pi^A - (\pi^B\pi^A - \pi^A\pi^B)\pi^C. \tag{B.3}$$

This form encodes the flavor combinations that decompose the $\mathbf{5} \otimes \mathbf{10}$ tensor product into the $\mathbf{10}$. Now we just have to identify the two pion states with vector states from Equation (B.1). From this we obtain a $\rho\pi$ operator that transforms in the 10-dimensional representation.

$$O^{\mathbf{10}}_{\rho\pi} = -\rho^A \pi^B + \rho^B \pi^A - \rho^C \pi^C \tag{B.4}$$

Appendix C

Additional Results for Mixed Stars

We report here additional results on the mass-radius relation and the second Love number for combinations of equations of state that were not presented in the main text. In Figure 17, we show the additional mass-radius relations. We can see that whether the data are compatible with the observation depends mostly on the ordinary matter equation of state employed. EoS I produces smaller masses and radii than EoS II, and the additional dark matter reduces these even further, making them incompatible with the observation. EoS III, however, produces larger masses and radii, and the addition of dark matter shifts the data points closer to the observation. In general, we see that the effects are very similar to those described in the main text. We also see that whether the heavy or light dark matter ensemble is employed essentially makes no difference. In Figure 18, we show the second Love number versus the compactness. Once again, we see the same characteristics described in the main text, and the changes are mainly related to the choice of different equations of state for ordinary matter and different dark matter candidate masses.

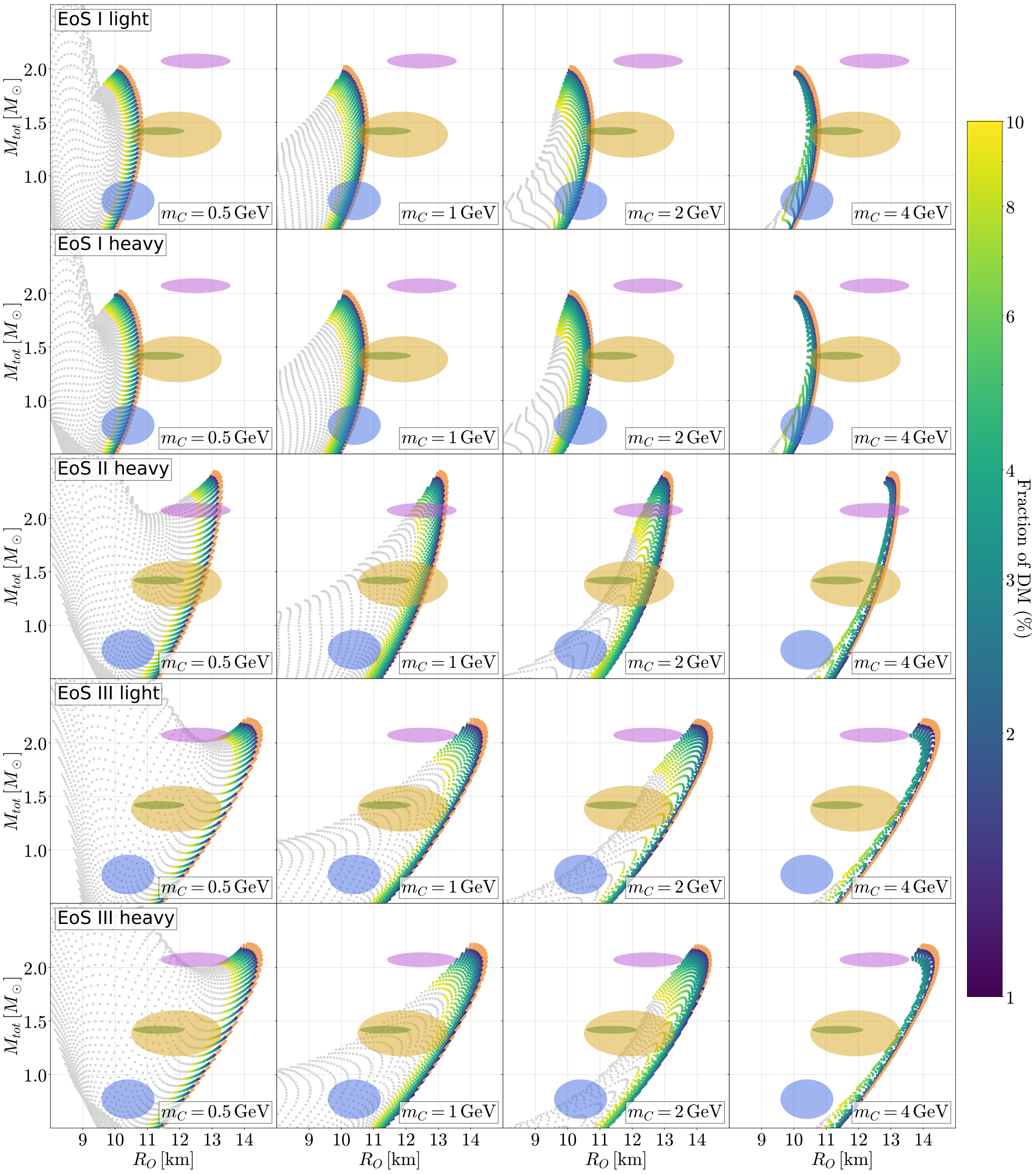

Figure 17: The mass-radius relations between and the total observable mass $M_O + M_D$ in $M_\odot$ and the observable ordinary matter radius R_O in km for the equations of state not shown in the main text.

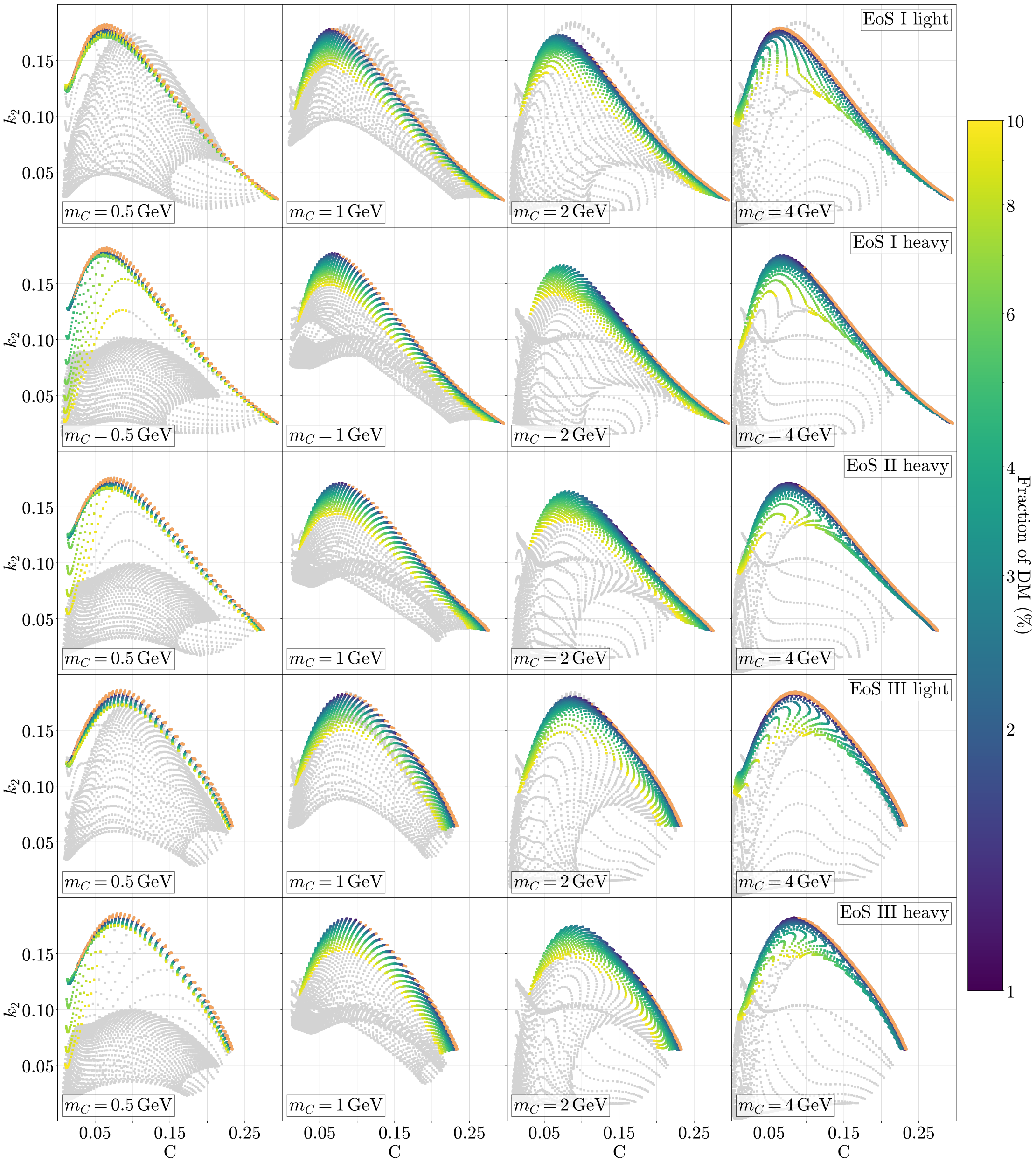

Figure 18: The second Love number k_2 plotted against the compactness obtained with the outermost radius $C = M_{\mathrm{tot}}/R_{\mathrm{max}}$ for the equations of state not shown in the main text.

Appendix D

Tabulated Lattice Results

We report here the energy levels extracted from the correlator fits and the phase shifts resulting from the Lüscher analysis. Table 12, shows the results in the 14-dimensional channel. We provide the number of gauge configurations, the number of stochastic sources, the one- and two-pion energy levels, and the resulting s-wave phase shift. For the ten-dimensional channel, we provide the energy levels from different irreps, as well as the center-of-mass energy and the p-wave phase shift, provided the energy levels are in the elastic window in Tables 13–15. The last column indicates whether we include the phase shift in the fit to ERE or Breit-Wigner. The number of gauge configurations and stochastic sources is given in the main text in Table 10.

Table 12: The ensembles used in this work to investigate the 14-dimensional channel. They are defined by the inverse gauge coupling β, the bare fermion masses of the degenerate fermions am_0 and the lattice volume ($N_L^3 \times N_T$). We give the number of configurations, the number of stochastic sources, the ratio of the pseudoscalar meson mass to the vector meson mass m_π/m_ρ, the ground state energy in lattice units for the one-pion and two-pion channel, and the perturbatively renormalized pion decay constant f_π for the comparison with the leading-order χPT prediction.

β	am_0	N_L	N_T	n_{config}	n_{src}	aE_π	$aE_{\pi\pi}$	δ_0
6.9	-0.92	12	24	63	4	0.416(19)	0.885(14)	144(5)
6.9	-0.92	14	24	550	4	0.3926(14)	0.7914(40)	172(3)
6.9	-0.92	16	32	176	4	0.3894(14)	0.7848(35)	173(4)
6.9	-0.92	24	32	467	16	0.38649(51)	0.7734(12)	174(8)
7.05	-0.835	12	24	313	16	0.4616(15)	0.9424(32)	156(1)
7.05	-0.835	14	24	619	4	0.4417(17)	0.9085(30)	164(2)
7.05	-0.835	20	36	100	16	0.4380(10)	0.8792(27)	175(4)
7.05	-0.85	12	24	84	1	0.3778(57)	0.786(22)	146(6)
7.05	-0.85	14	24	167	4	0.3496(25)	0.7236(67)	158(3)
7.05	-0.85	16	32	101	4	0.3375(17)	0.6892(41)	168(3)
7.05	-0.85	24	36	100	16	0.33076(97)	0.6638(23)	176(3)
7.2	-0.78	12	24	150	16	0.4382(34)	0.9024(84)	129(3)
7.2	-0.78	14	24	425	16	0.3857(14)	0.7951(35)	157(2)
7.2	-0.78	16	32	265	16	0.3809(11)	0.7703(31)	163(2)
7.2	-0.78	24	36	508	16	0.36963(39)	0.74360(79)	172(2)
7.2	-0.794	14	24	234	4	0.3234(26)	0.6888(66)	142(2)
7.2	-0.794	16	32	101	4	0.3097(17)	0.6463(50)	150(2)
7.2	-0.794	28	36	504	16	0.28524(35)	0.57582(97)	175(1)

Table 13: The results of the Lüscher analysis in the 10-dimensional channel in the non-resonant ensembles. We obtain one energy level in the irreps T_1, E, and B_1 coming from a single ρ-operator and two energy levels in the A_1 irrep from the variational analysis including ρ-operators with the structures $\Gamma = \gamma_\mu$ and $\Gamma = \gamma_4\gamma_\mu$, labeled by n. We give the energy in the lattice frame and the center-of-mass energy as well as the p-wave phase-shift, given that the center-of-mass energy was in the elastic window. In this case, we only include data points from the A_1 irrep in the fit.

N_L	$\vec{P}$	Λ	n	$aE_n^{\Lambda,\vec{P}}$	$a\sqrt{s_n^{\Lambda,\vec{P}}}$	δ_1	Incl.
14	0	T_1	1	0.558(3)	0.558(3)	–	No
14	1	A_1	1	0.693(7)	0.528(10)	–	No
14	1	A_1	2	0.97(2)	0.85(2)	0(9)	No
14	1	E	1	0.712(5)	0.553(6)	–	No
14	2	A_1	1	0.825(5)	0.527(8)	–	No
14	2	A_1	2	1.06(2)	0.85(2)	18(2)	Yes
14	2	B_1	1	0.84(2)	0.55(3)	–	No
16	0	T_1	1	0.552(4)	0.552(4)	–	No
16	1	A_1	1	0.660(3)	0.530(4)	–	No
16	1	A_1	2	0.94(2)	0.85(2)	0(9)	No
16	1	E	1	0.683(4)	0.558(5)	–	No
16	2	A_1	1	0.758(3)	0.516(4)	–	No
16	2	B_1	1	0.774(9)	0.54(1)	–	No
20	0	T_1	1	0.547(2)	0.547(2)	–	No
20	1	A_1	1	0.648(4)	0.567(5)	–	No
20	1	A_1	2	0.835(4)	0.773(4)	0.0(5)	No
20	1	E	1	0.626(4)	0.541(4)	–	No
20	2	A_1	1	0.705(7)	0.548(9)	–	No
20	2	A_1	2	0.945(8)	0.834(9)	18(4)	Yes
20	2	B_1	1	0.695(7)	0.535(9)	–	No
20	3	A_1	1	0.776(5)	0.553(7)	–	No
20	3	A_1	2	1.01(1)	0.86(1)	31(8)	Yes
20	3	E	1	0.78(1)	0.56(2)	–	No
24	0	T_1	1	0.545(1)	0.545(1)	–	No
24	1	A_1	1	0.601(2)	0.541(3)	–	No
24	1	A_1	2	0.842(5)	0.801(6)	5(2)	Yes
24	1	E	1	0.602(2)	0.542(3)	–	No
24	2	A_1	1	0.642(2)	0.524(2)	–	No
24	2	A_1	2	0.90(1)	0.82(1)	17(7)	Yes
24	2	B_1	1	0.658(2)	0.543(3)	–	No
24	3	A_1	1	0.688(2)	0.517(3)	–	No
24	3	A_1	2	0.94(2)	0.82(3)	40(2)	Yes
24	3	E	1	0.700(9)	0.53(1)	–	No

Table 14: Same as Table 13 for the close-to-resonant ensembles. Since the data was scattered in the elastic window with large error, we do not perform a fit in this case.

N_L	$\vec{P}$	Λ	n	$aE_n^{\Lambda,\vec{P}}$	$a\sqrt{s_n^{\Lambda,\vec{P}}}$	δ_1	Incl.
16	0	T_1	1	0.420(8)	0.420(8)	179(3)	No
16	1	A_1	1	0.488(8)	0.29(1)	–	No
16	1	A_1	2	0.78(5)	0.67(5)	140(2)	No
16	1	E	1	0.58(2)	0.42(3)	0(9)	No
20	0	T_1	1	0.387(5)	0.387(5)	–	No
20	1	A_1	1	0.423(7)	0.284(10)	–	No
20	1	A_1	2	0.68(3)	0.60(4)	140(1)	No
20	1	E	1	0.50(1)	0.39(1)	–	No
20	2	A_1	1	0.533(7)	0.29(1)	–	No
20	2	A_1	2	0.77(6)	0.63(8)	140(4)	No
20	2	B_1	1	0.61(2)	0.42(3)	0(9)	No
20	3	A_1	1	0.64(1)	0.34(2)	–	No
20	3	A_1	2	0.91(4)	0.74(6)	130(2)	No
20	3	E	1	0.75(3)	0.52(4)	90(3)	No
24	0	T_1	1	0.387(5)	0.387(5)	–	No
24	1	A_1	1	0.394(3)	0.294(5)	–	No
24	1	A_1	2	0.70(2)	0.65(2)	80(2)	No
24	1	E	1	0.47(1)	0.39(2)	–	No
24	2	A_1	1	0.471(6)	0.292(10)	–	No
24	2	A_1	2	0.80(2)	0.71(2)	60(3)	No
24	2	B_1	1	0.53(2)	0.38(2)	–	No
24	3	A_1	1	0.552(6)	0.32(1)	–	No
24	3	A_1	2	0.83(3)	0.70(3)	110(2)	No
24	3	E	1	0.59(3)	0.38(5)	–	No
36	0	T_1	1	0.378(6)	0.378(6)	–	No
36	1	A_1	1	0.349(5)	0.302(5)	–	No
36	1	A_1	2	0.61(2)	0.59(2)	120(5)	No
36	1	E	1	0.426(8)	0.389(9)	–	No
36	2	A_1	1	0.383(4)	0.293(6)	–	No
36	2	A_1	2	0.68(2)	0.63(2)	50(4)	No
36	2	B_1	1	0.46(1)	0.39(1)	–	No
36	3	A_1	1	0.421(6)	0.294(8)	–	No
36	3	A_1	2	0.68(3)	0.60(3)	70(3)	No
36	3	E	1	0.51(2)	0.41(2)	–	No

Table 15: Same as Table 13 for the resonant ensembles. In this case, we only include data points from single ρ-operators in the irreps E and B_2.

N_L	$\vec{P}$	Λ	n	$aE_n^{\Lambda,\vec{P}}$	$a\sqrt{s_n^{\Lambda,\vec{P}}}$	δ_1	Incl.
16	0	T_1	1	0.43(1)	0.43(1)	149(4)	Yes
16	1	A_1	1	0.47(1)	0.27(3)	–	No
16	1	A_1	2	0.84(6)	0.75(7)	–	No
16	1	E	1	0.60(3)	0.46(4)	143(10)	Yes
24	0	T_1	1	0.36(2)	0.36(2)	147(8)	Yes
24	1	A_1	1	0.33(2)	0.20(3)	–	No
24	1	A_1	2	0.72(5)	0.67(5)	–	No
24	1	E	1	0.46(2)	0.38(3)	140(1)	Yes
24	2	A_1	1	0.41(2)	0.18(5)	–	No
24	2	A_1	2	0.69(8)	0.59(9)	100(7)	No
24	2	B_1	1	0.46(5)	0.28(9)	–	No
24	3	A_1	1	0.51(2)	0.23(5)	–	No
24	3	A_1	2	0.9(1)	0.8(1)	–	No
24	3	E	1	0.72(5)	0.55(7)	170(8)	No
36	0	T_1	1	0.351(7)	0.351(7)	122(8)	Yes
36	1	A_1	1	0.272(9)	0.21(1)	–	No
36	1	A_1	2	0.56(2)	0.53(2)	90(4)	No
36	1	E	1	0.385(9)	0.343(10)	134(10)	Yes
36	2	A_1	1	0.32(1)	0.20(2)	–	No
36	2	A_1	2	0.63(4)	0.58(4)	30(4)	No
36	2	B_1	1	0.44(1)	0.37(1)	120(1)	Yes
36	3	A_1	1	0.384(9)	0.24(1)	–	No
36	3	A_1	2	0.71(2)	0.65(2)	–	No
36	3	E	1	0.48(3)	0.37(3)	60(5)	Yes

Bibliography

[1] F. Zwicky. "Die Rotverschiebung von extragalaktischen Nebeln". In: *Helv. Phys. Acta* 6 (1933), pp. 110–127. DOI: `10.1007/s10714-008-0707-4`.

[2] V. C. Rubin and W. K. Ford Jr. "Rotation of the Andromeda Nebula from a Spectroscopic Survey of Emission Regions". In: *Astrophys. J.* 159 (1970), pp. 379–403. DOI: `10.1086/150317`.

[3] V. C. Rubin, W. K. Ford Jr., and N. Thonnard. "Extended rotation curves of high-luminosity spiral galaxies. IV. Systematic dynamical properties, Sa through Sc". In: *Astrophys. J. Lett.* 225 (1978), pp. L107–L111. DOI: `10.1086/182804`.

[4] S. Navas et al. (Particle Data Group). "Review of particle physics". In: *Phys. Rev. D* 110.3 (2024), p. 030001. DOI: `10.1103/PhysRevD.110.030001`.

[5] S. D. M. White, G. Efstathiou, and C. S. Frenk. "The Amplitude of mass fluctuations in the universe". In: *Mon. Not. Roy. Astron. Soc.* 262 (1993), pp. 1023–1028.

[6] A. Arbey and F. Mahmoudi. "Dark matter and the early Universe: a review". In: *Prog. Part. Nucl. Phys.* 119 (2021), p. 103865. DOI: `10.1016/j.ppnp.2021.103865`. arXiv: `2104.11488 [hep-ph]`.

[7] A. M. Green. "Dark matter in astrophysics/cosmology". In: *SciPost Phys. Lect. Notes* 37 (2022), p. 1. DOI: `10.21468/SciPostPhysLectNotes.37`. arXiv: `2109.05854 [hep-ph]`.

[8] M. Cirelli, A. Strumia, and J. Zupan. "Dark Matter" (June 2024). arXiv: `2406.01705 [hep-ph]`.

[9] N. Aghanim et al. (Planck). "Planck 2018 results. I. Overview and the cosmological legacy of Planck". In: *Astron. Astrophys.* 641 (2020), A1. DOI: `10.1051/0004-6361/201833880`. arXiv: `1807.06205 [astro-ph.CO]`.

[10] N. Aghanim et al. (Planck). “Planck 2018 results. VI. Cosmological parameters”. In: *Astron. Astrophys.* 641 (2020). [Erratum: Astron.Astrophys. 652, C4 (2021)], A6. DOI: `10.1051/0004-6361/201833910`. arXiv: `1807.06209 [astro-ph.CO]`.

[11] M. Tristram et al. “Cosmological parameters derived from the final Planck data release (PR4)”. In: *Astron. Astrophys.* 682 (2024), A37. DOI: `10.1051/0004-6361/202348015`. arXiv: `2309.10034 [astro-ph.CO]`.

[12] A. G. Adame et al. (DESI). “Validation of the Scientific Program for the Dark Energy Spectroscopic Instrument”. In: *Astron. J.* 167.2 (2024), p. 62. DOI: `10.3847/1538-3881/ad0b08`. arXiv: `2306.06307 [astro-ph.CO]`.

[13] M. Abdul Karim et al. (DESI). “DESI DR2 results. II. Measurements of baryon acoustic oscillations and cosmological constraints”. In: *Phys. Rev. D* 112.8 (2025), p. 083515. DOI: `10.1103/tr6y-kpc6`. arXiv: `2503.14738 [astro-ph.CO]`.

[14] M. Abdul Karim et al. (DESI). “Data Release 1 of the Dark Energy Spectroscopic Instrument” (Mar. 2025). arXiv: `2503.14745 [astro-ph.CO]`.

[15] I. Banik and H. Zhao. “From Galactic Bars to the Hubble Tension: Weighing Up the Astrophysical Evidence for Milgromian Gravity”. In: *Symmetry* 14.7 (2022), p. 1331. DOI: `10.3390/sym14071331`. arXiv: `2110.06936 [astro-ph.CO]`.

[16] S. Nojiri and S. D. Odintsov. “Unified cosmic history in modified gravity: from F(R) theory to Lorentz non-invariant models”. In: *Phys. Rept.* 505 (2011), pp. 59–144. DOI: `10.1016/j.physrep.2011.04.001`. arXiv: `1011.0544 [gr-qc]`.

[17] S. W. Randall et al. “Constraints on the Self-Interaction Cross-Section of Dark Matter from Numerical Simulations of the Merging Galaxy Cluster 1E 0657-56”. In: *Astrophys. J.* 679 (2008), pp. 1173–1180. DOI: `10.1086/587859`. arXiv: `0704.0261 [astro-ph]`.

[18] K. E. Andrade et al. “A stringent upper limit on dark matter self-interaction cross-section from cluster strong lensing”. In: *Mon. Not. Roy. Astron. Soc.* 510.1 (2021), pp. 54–81. DOI: `10.1093/mnras/stab3241`. arXiv: `2012.06611 [astro-ph.CO]`.

[19] B. Audren et al. “Strongest model-independent bound on the lifetime of Dark Matter”. In: *JCAP* 12 (2014), p. 028. DOI: `10.1088/1475-7516/2014/12/028`. arXiv: `1407.2418 [astro-ph.CO]`.

[20] B. Carr et al. “Constraints on primordial black holes”. In: *Rept. Prog. Phys.* 84.11 (2021), p. 116902. DOI: `10.1088/1361-6633/ac1e31`. arXiv: `2002.12778 [astro-ph.CO]`.

[21] J. Billard et al. “Direct detection of dark matterAPPEC committee report*”. In: *Rept. Prog. Phys.* 85.5 (2022), p. 056201. DOI: `10.1088/1361-6633/ac5754`. arXiv: `2104.07634 [hep-ex]`.

[22] T. Lin. “Dark matter models and direct detection”. In: *PoS* 333 (2019), p. 009. DOI: `10.22323/1.333.0009`. arXiv: `1904.07915 [hep-ph]`.

[23] R. Essig et al. “Snowmass2021 Cosmic Frontier: The landscape of low-threshold dark matter direct detection in the next decade”. In: *Snowmass 2021.* Mar. 2022. arXiv: `2203.08297 [hep-ph]`.

[24] G. Angloher et al. (CRESST). “Constraints on self-interaction cross-sections of dark matter in universal bound states from direct detection”. In: *Eur. Phys. J. C* 84.11 (2024), p. 1170. DOI: `10.1140/epjc/s10052-024-13472-4`. arXiv: `2407.04004 [astro-ph.CO]`.

[25] G. Angloher et al. (CRESST). “First observation of single photons in a CRESST detector and new dark matter exclusion limits”. In: *Phys. Rev. D* 110.8 (2024), p. 083038. DOI: `10.1103/PhysRevD.110.083038`. arXiv: `2405.06527 [astro-ph.CO]`.

[26] J. Aalbers et al. (LZ). “First Dark Matter Search Results from the LUX-ZEPLIN (LZ) Experiment”. In: *Phys. Rev. Lett.* 131.4 (2023), p. 041002. DOI: `10.1103/PhysRevLett.131.041002`. arXiv: `2207.03764 [hep-ex]`.

[27] Y. Meng et al. (PandaX-4T). “Dark Matter Search Results from the PandaX-4T Commissioning Run”. In: *Phys. Rev. Lett.* 127.26 (2021), p. 261802. DOI: `10.1103/PhysRevLett.127.261802`. arXiv: `2107.13438 [hep-ex]`.

[28] E. Aprile et al. (XENON). “First Dark Matter Search with Nuclear Recoils from the XENONnT Experiment”. In: *Phys. Rev. Lett.* 131.4 (2023), p. 041003. DOI: `10.1103/PhysRevLett.131.041003`. arXiv: `2303.14729 [hep-ex]`.

[29] N. Trevisani (ATLAS, CMS). “Collider Searches for Dark Matter (ATLAS + CMS)”. In: *Universe* 4.11 (2018), p. 131. DOI: `10.3390/universe4110131`.

[30] E. Tolley (ATLAS). “Dark Matter searches with the ATLAS Detector”. In: *PoS* ICHEP2018 (2019), p. 171. DOI: `10.22323/1.340.0171`.

[31] W. C. Kalderon (ATLAS). “Dark Matter searches with the ATLAS Detector”. In: *PoS* DIS2018 (2018), p. 085. DOI: `10.22323/1.316.0085`.

[32] D. Vannerom (CMS). “Dark Matter searches with CMS”. In: *PoS* DIS2019 (2019), p. 111. DOI: `10.22323/1.352.0111`.

[33] G. Gómez-Ceballos (CMS). “Dark Matter Searches with the CMS Experiment”. In: *PoS* EDSU2018 (2018), p. 014. DOI: `10.22323/1.335.0014`.

[34] M. Ackermann et al. (Fermi-LAT). “Observations of M31 and M33 with the Fermi Large Area Telescope: A Galactic Center Excess in Andromeda?” In: *Astrophys. J.* 836.2 (2017), p. 208. DOI: `10.3847/1538-4357/aa5c3d`. arXiv: `1702.08602 [astro-ph.HE]`.

[35] R. M. Bandyopadhyay et al. “On the Origin of the 511 keV Emission in the Galactic Centre”. In: *Mon. Not. Roy. Astron. Soc.* 392 (2009), p. 1115. DOI: `10.1111/j.1365-2966.2008.14113.x`. arXiv: `0810.3674 [astro-ph]`.

[36] D. P. Finkbeiner and N. Weiner. “Exciting Dark Matter and the INTEGRAL/SPI 511 keV signal”. In: *Phys. Rev. D* 76 (2007), p. 083519. DOI: `10.1103/PhysRevD.76.083519`. arXiv: `astro-ph/0702587`.

[37] S. Adhikari et al. “Astrophysical Tests of Dark Matter Self-Interactions” (July 2022). arXiv: `2207.10638 [astro-ph.CO]`.

[38] S. Tulin and H.-B. Yu. “Dark Matter Self-interactions and Small Scale Structure”. In: *Phys. Rept.* 730 (2018), pp. 1–57. DOI: `10.1016/j.physrep.2017.11.004`. arXiv: `1705.02358 [hep-ph]`.

[39] J. S. Bullock and M. Boylan-Kolchin. “Small-Scale Challenges to the ΛCDM Paradigm”. In: *Ann. Rev. Astron. Astrophys.* 55 (2017), pp. 343–387. DOI: `10.1146/annurev-astro-091916-055313`. arXiv: `1707.04256 [astro-ph.CO]`.

[40] L. V. Sales, A. Wetzel, and A. Fattahi. “Baryonic solutions and challenges for cosmological models of dwarf galaxies”. In: *Nature Astron.* 6.8 (2022), pp. 897–910. DOI: `10.1038/s41550-022-01689-w`. arXiv: `2206.05295 [astro-ph.GA]`.

[41] I. M. E. Santos-Santos et al. “Baryonic clues to the puzzling diversity of dwarf galaxy rotation curves”. In: *Mon. Not. Roy. Astron. Soc.* 495.1 (2020), pp. 58–77. DOI: `10.1093/mnras/staa1072`. arXiv: `1911.09116 [astro-ph.GA]`.

[42] M. Dutta and S. Mahapatra. “Mini-review on self-interacting dark matter” (Feb. 2024). DOI: `10.1140/epjs/s11734-024-01121-6`.

[43] D. Eckert et al. "Constraints on dark matter self-interaction from the internal density profiles of X-COP galaxy clusters". In: *Astron. Astrophys.* 666 (2022), A41. DOI: `10.1051/0004-6361/202243205`. arXiv: `2205.01123 [astro-ph.CO]`.

[44] V. M. Sabarish et al. "Simulations of galaxy cluster mergers with velocity-dependent, rare, and frequent self-interactions". In: *Mon. Not. Roy. Astron. Soc.* 529.3 (2024), pp. 2032–2046. DOI: `10.1093/mnras/stae664`. arXiv: `2310.07769 [astro-ph.CO]`.

[45] N. J. Outmezguine et al. "Universal gravothermal evolution of isolated self-interacting dark matter halos for velocity-dependent cross-sections". In: *Mon. Not. Roy. Astron. Soc.* 523.3 (2023), pp. 4786–4800. DOI: `10.1093/mnras/stad1705`. arXiv: `2204.06568 [astro-ph.GA]`.

[46] M. Kaplinghat, S. Tulin, and H.-B. Yu. "Dark Matter Halos as Particle Colliders: Unified Solution to Small-Scale Structure Puzzles from Dwarfs to Clusters". In: *Phys. Rev. Lett.* 116.4 (2016), p. 041302. DOI: `10.1103/PhysRevLett.116.041302`. arXiv: `1508.03339 [astro-ph.CO]`.

[47] L. Sagunski et al. "Velocity-dependent Self-interacting Dark Matter from Groups and Clusters of Galaxies". In: *JCAP* 01 (2021), p. 024. DOI: `10.1088/1475-7516/2021/01/024`. arXiv: `2006.12515 [astro-ph.CO]`.

[48] S. Gad-Nasr et al. "On the late-time evolution of velocity-dependent self-interacting dark matter halos". In: *JCAP* 05 (2024), p. 131. DOI: `10.1088/1475-7516/2024/05/131`. arXiv: `2312.09296 [astro-ph.GA]`.

[49] S. Profumo. *An Introduction to Particle Dark Matter*. World Scientific, 2017. ISBN: 978-1-78634-000-9, 978-1-78634-001-6, 978-1-78634-001-6. DOI: `10.1142/q0001`.

[50] Y. Hochberg et al. "Mechanism for Thermal Relic Dark Matter of Strongly Interacting Massive Particles". In: *Phys. Rev. Lett.* 113 (2014), p. 171301. DOI: `10.1103/PhysRevLett.113.171301`. arXiv: `1402.5143 [hep-ph]`.

[51] Y. Hochberg et al. "Model for Thermal Relic Dark Matter of Strongly Interacting Massive Particles". In: *Phys. Rev. Lett.* 115.2 (2015), p. 021301. DOI: `10.1103/PhysRevLett.115.021301`. arXiv: `1411.3727 [hep-ph]`.

[52] Y. Hochberg, E. Kuflik, and H. Murayama. "SIMP Spectroscopy". In: *JHEP* 05 (2016), p. 090. DOI: `10.1007/JHEP05(2016)090`. arXiv: `1512.07917 [hep-ph]`.

[53] E. D. Carlson, M. E. Machacek, and L. J. Hall. “Self-interacting dark matter”. In: *Astrophys. J.* 398 (1992), pp. 43–52. DOI: `10.1086/171833`.

[54] A. Kamada et al. “Self-Heating Dark Matter via Semiannihilation”. In: *Phys. Rev. Lett.* 120.13 (2018), p. 131802. DOI: `10.1103/PhysRevLett.120.131802`. arXiv: `1707.09238 [hep-ph]`.

[55] A. Kamada, M. Yamada, and T. T. Yanagida. “Strongly-interacting massive particle and dark photon in the era of the intensity frontier”. In: *Phys. Rev. D* 102.7 (2020), p. 075001. DOI: `10.1103/PhysRevD.102.075001`. arXiv: `2004.13966 [hep-ph]`.

[56] A. Kamada, H. J. Kim, and H. Kim. “Self-heating of Strongly Interacting Massive Particles”. In: *Phys. Rev. D* 98.2 (2018), p. 023509. DOI: `10.1103/PhysRevD.98.023509`. arXiv: `1805.05648 [hep-ph]`.

[57] E. Bernreuther et al. “Dark matter relic density in strongly interacting dark sectors with light vector mesons”. In: *Phys. Rev. D* 110.3 (2024), p. 035009. DOI: `10.1103/PhysRevD.110.035009`. arXiv: `2311.17157 [hep-ph]`.

[58] M. E. Peskin and D. V. Schroeder. *An Introduction to quantum field theory.* Reading, USA: Addison-Wesley, 1995. ISBN: 978-0-201-50397-5, 978-0-429-50355-9, 978-0-429-49417-8. DOI: `10.1201/9780429503559`.

[59] D. J. Gross and F. Wilczek. “Ultraviolet Behavior of Nonabelian Gauge Theories”. In: *Phys. Rev. Lett.* 30 (1973). Ed. by J. C. Taylor, pp. 1343–1346. DOI: `10.1103/PhysRevLett.30.1343`.

[60] H. D. Politzer. “Reliable Perturbative Results for Strong Interactions?” In: *Phys. Rev. Lett.* 30 (1973). Ed. by J. C. Taylor, pp. 1346–1349. DOI: `10.1103/PhysRevLett.30.1346`.

[61] G. S. Bali et al. (SESAM). “Observation of string breaking in QCD”. In: *Phys. Rev. D* 71 (2005), p. 114513. DOI: `10.1103/PhysRevD.71.114513`. arXiv: `hep-lat/0505012`.

[62] M. Q. Huber, C. S. Fischer, and H. Sanchis-Alepuz. “Higher spin glueballs from functional methods”. In: *Eur. Phys. J. C* 81.12 (2021). [Erratum: Eur.Phys.J.C 82, 38 (2022)], p. 1083. DOI: `10.1140/epjc/s10052-021-09864-5`. arXiv: `2110.09180 [hep-ph]`.

[63] C. J. Morningstar and M. J. Peardon. “The Glueball spectrum from an anisotropic lattice study”. In: *Phys. Rev. D* 60 (1999), p. 034509. DOI: `10.1103/PhysRevD.60.034509`. arXiv: `hep-lat/9901004`.

[64] A. Athenodorou and M. Teper. “The glueball spectrum of SU(3) gauge theory in 3 + 1 dimensions”. In: *JHEP* 11 (2020), p. 172. DOI: `10.1007/JHEP11(2020)172`. arXiv: `2007.06422 [hep-lat]`.

[65] E. Noether. “Invariant Variation Problems”. In: *Gott. Nachr.* 1918 (1918), pp. 235–257. DOI: `10.1080/00411457108231446`. arXiv: `physics/0503066`.

[66] E. Bennett et al. “Mixing between flavor singlets in lattice gauge theories coupled to matter fields in multiple representations”. In: *Phys. Rev. D* 110.7 (2024), p. 074504. DOI: `10.1103/PhysRevD.110.074504`. arXiv: `2405.05765 [hep-lat]`.

[67] V. Ayyar et al. “Spectroscopy of SU(4) composite Higgs theory with two distinct fermion representations”. In: *Phys. Rev. D* 97.7 (2018), p. 074505. DOI: `10.1103/PhysRevD.97.074505`. arXiv: `1710.00806 [hep-lat]`.

[68] V. Ayyar et al. “Baryon spectrum of SU(4) composite Higgs theory with two distinct fermion representations”. In: *Phys. Rev. D* 97.11 (2018), p. 114505. DOI: `10.1103/PhysRevD.97.114505`. arXiv: `1801.05809 [hep-ph]`.

[69] V. Ayyar et al. “Finite-temperature phase structure of SU(4) gauge theory with multiple fermion representations”. In: *Phys. Rev. D* 97.11 (2018), p. 114502. DOI: `10.1103/PhysRevD.97.114502`. arXiv: `1802.09644 [hep-lat]`.

[70] V. Ayyar et al. “Partial compositeness and baryon matrix elements on the lattice”. In: *Phys. Rev. D* 99.9 (2019), p. 094502. DOI: `10.1103/PhysRevD.99.094502`. arXiv: `1812.02727 [hep-ph]`.

[71] G. Cossu et al. “Strong dynamics with matter in multiple representations: SU(4) gauge theory with fundamental and sextet fermions”. In: *Eur. Phys. J. C* 79.8 (2019), p. 638. DOI: `10.1140/epjc/s10052-019-7137-1`. arXiv: `1904.08885 [hep-lat]`.

[72] Y. Shamir et al. “*S* parameter from a prototype composite-Higgs model”. In: *PoS* LATTICE2021 (2022), p. 611. DOI: `10.22323/1.396.0611`. arXiv: `2110.05198 [hep-lat]`.

[73] A. Lupo et al. “Spectral reconstruction in SU(4) gauge theory with fermions in multiple representations”. In: *PoS* LATTICE2021 (2022), p. 092. DOI: `10.22323/1.396.0092`. arXiv: `2112.01158 [hep-lat]`.

[74] L. Del Debbio et al. “Multi-representation dynamics of SU(4) composite Higgs models: chiral limit and spectral reconstructions”. In: *Eur. Phys. J. C* 83.3 (2023), p. 220. DOI: `10.1140/epjc/s10052-023-11363-8`. arXiv: `2211.09581 [hep-lat]`.

[75] A. Hasenfratz et al. “Infrared fixed point and anomalous dimensions in a composite Higgs model”. In: *Phys. Rev. D* 107.11 (2023), p. 114504. DOI: `10.1103/PhysRevD.107.114504`. arXiv: `2304.11729 [hep-lat]`.

[76] E. Bennett et al. “Lattice investigations of the chimera baryon spectrum in the Sp(4) gauge theory”. In: *Phys. Rev. D* 109.9 (2024), p. 094512. DOI: `10.1103/PhysRevD.109.094512`. arXiv: `2311.14663 [hep-lat]`.

[77] H. Hsiao et al. “Chimera baryon spectrum in the Sp(4) completion of composite Higgs models”. In: *PoS* LATTICE2023 (2024), p. 089. DOI: `10.22323/1.453.0089`. arXiv: `2401.05637 [hep-lat]`.

[78] H. Hsiao et al. “Spectroscopy of chimera baryons in a $Sp(4)$ lattice gauge theory” (Nov. 2022). DOI: `10.22323/1.430.0211`. arXiv: `2211.03955 [hep-lat]`.

[79] G. Bergner and S. Piemonte. “Lattice simulations of a gauge theory with mixed adjoint-fundamental matter”. In: *Phys. Rev. D* 103.1 (2021). [Erratum: Phys.Rev.D 107, 019902 (2023)], p. 014503. DOI: `10.1103/PhysRevD.103.014503`. arXiv: `2008.02855 [hep-lat]`.

[80] G. Bergner and S. Piemonte. “Mixed adjoint-fundamental matter and applications towards SQCD and beyond”. In: *PoS* LATTICE2021 (2022), p. 242. DOI: `10.22323/1.396.0242`. arXiv: `2111.15335 [hep-lat]`.

[81] E. Bennett et al. “Lattice studies of the Sp(4) gauge theory with two fundamental and three antisymmetric Dirac fermions”. In: *Phys. Rev. D* 106.1 (2022), p. 014501. DOI: `10.1103/PhysRevD.106.014501`. arXiv: `2202.05516 [hep-lat]`.

[82] S. L. Adler. “Axial vector vertex in spinor electrodynamics”. In: *Phys. Rev.* 177 (1969), pp. 2426–2438. DOI: `10.1103/PhysRev.177.2426`.

[83] J. B. Kogut et al. “QCD - like theories at finite baryon density”. In: *Nucl. Phys. B* 582 (2000), pp. 477–513. DOI: `10.1016/S0550-3213(00)00242-X`. arXiv: `hep-ph/0001171`.

[84] U.-G. MeiSSner and A. Rusetsky. *Effective Field Theories*. Cambridge University Press, Aug. 2022. ISBN: 978-1-108-68903-8. DOI: `10.1017/9781108689038`.

[85] S. Kulkarni et al. “Low-energy effective description of dark $Sp(4)$ theories”. In: *SciPost Phys.* 14.3 (2023), p. 044. DOI: `10.21468/SciPostPhys.14.3.044`. arXiv: `2202.05191 [hep-ph]`.

[86] J. Wess and B. Zumino. “Consequences of anomalous Ward identities”. In: *Phys. Lett. B* 37 (1971), pp. 95–97. DOI: `10.1016/0370-2693(71)90582-X`.

[87] E. Witten. “Global Aspects of Current Algebra”. In: *Nucl. Phys. B* 223 (1983), pp. 422–432. DOI: `10.1016/0550-3213(83)90063-9`.

[88] F. J. Yndurain. *The Theory of Quark and Gluon Interactions.* Theoretical and Mathematical Physics. Berlin, Germany: Springer, 2006. ISBN: 978-3-540-33209-1, 978-3-540-33210-7. DOI: `10.1007/3-540-33210-3`.

[89] U. G. Meissner. “Low-Energy Hadron Physics from Effective Chiral Lagrangians with Vector Mesons”. In: *Phys. Rept.* 161 (1988), p. 213. DOI: `10.1016/0370-1573(88)90090-7`.

[90] K. Kawarabayashi and M. Suzuki. “Partially conserved axial vector current and the decays of vector mesons”. In: *Phys. Rev. Lett.* 16 (1966), p. 255. DOI: `10.1103/PhysRevLett.16.255`.

[91] Riazuddin and Fayyazuddin. “Algebra of current components and decay widths of rho and K* mesons”. In: *Phys. Rev.* 147 (1966), pp. 1071–1073. DOI: `10.1103/PhysRev.147.1071`.

[92] E. Bennett et al. “Sp(4) gauge theory on the lattice: towards SU(4)/Sp(4) composite Higgs (and beyond)”. In: *JHEP* 03 (2018), p. 185. DOI: `10.1007/JHEP03(2018)185`. arXiv: `1712.04220 [hep-lat]`.

[93] J. Barnard, T. Gherghetta, and T. S. Ray. “UV descriptions of composite Higgs models without elementary scalars”. In: *JHEP* 02 (2014), p. 002. DOI: `10.1007/JHEP02(2014)002`. arXiv: `1311.6562 [hep-ph]`.

[94] G. Cacciapaglia, C. Pica, and F. Sannino. “Fundamental Composite Dynamics: A Review”. In: *Phys. Rept.* 877 (2020), pp. 1–70. DOI: `10.1016/j.physrep.2020.07.002`. arXiv: `2002.04914 [hep-ph]`.

[95] E. Bennett et al. “Sp(4) gauge theories on the lattice: $N_f = 2$ dynamical fundamental fermions”. In: *JHEP* 12 (2019), p. 053. DOI: `10.1007/JHEP12(2019)053`. arXiv: `1909.12662 [hep-lat]`.

[96] E. Bennett et al. “Sp(2N) Lattice Gauge Theories and Extensions of the Standard Model of Particle Physics”. In: *Universe* 9.5 (2023), p. 236. DOI: `10.3390/universe9050236`. arXiv: `2304.01070 [hep-lat]`.

[97] G. Ferretti and D. Karateev. "Fermionic UV completions of Composite Higgs models". In: *JHEP* 03 (2014), p. 077. DOI: `10.1007/JHEP03(2014)077`. arXiv: `1312.5330 [hep-ph]`.

[98] T. A. Ryttov and F. Sannino. "Ultra Minimal Technicolor and its Dark Matter TIMP". In: *Phys. Rev. D* 78 (2008), p. 115010. DOI: `10.1103/PhysRevD.78.115010`. arXiv: `0809.0713 [hep-ph]`.

[99] J. M. Cline et al. "Composite strongly interacting dark matter". In: *Phys. Rev. D* 90.1 (2014), p. 015023. DOI: `10.1103/PhysRevD.90.015023`. arXiv: `1312.3325 [hep-ph]`.

[100] S. Bhattacharya, B. Meli, and J. Wudka. "Pionic Dark Matter". In: *JHEP* 02 (2014), p. 115. DOI: `10.1007/JHEP02(2014)115`. arXiv: `1307.2647 [hep-ph]`.

[101] N. Yamanaka et al. "Dark matter in the hidden gauge theory" (Nov. 2014). arXiv: `1411.2172 [hep-ph]`.

[102] V. Drach et al. "Template Composite Dark Matter: $SU(2)$ gauge theory with 2 fundamental flavours". In: *PoS* LATTICE2015 (2016), p. 234. DOI: `10.22323/1.251.0234`. arXiv: `1511.04370 [hep-lat]`.

[103] D. Kondo et al. "Linear sigma dark matter". In: *JHEP* 09 (2022), p. 041. DOI: `10.1007/JHEP09(2022)041`. arXiv: `2205.08088 [hep-ph]`.

[104] Y.-D. Tsai, R. McGehee, and H. Murayama. "Resonant Self-Interacting Dark Matter from Dark QCD". In: *Phys. Rev. Lett.* 128.17 (2022), p. 172001. DOI: `10.1103/PhysRevLett.128.172001`. arXiv: `2008.08608 [hep-ph]`.

[105] A. Maas et al. "The phase diagram of a gauge theory with fermionic baryons". In: *Phys.Rev.* D86 (2012), p. 111901. DOI: `10.1103/PhysRevD.86.111901`. arXiv: `1203.5653 [hep-lat]`.

[106] B. H. Wellegehausen et al. "Hadron masses and baryonic scales in G_2-QCD at finite density". In: *Phys. Rev. D* 89.5 (2014), p. 056007. DOI: `10.1103/PhysRevD.89.056007`. arXiv: `1312.5579 [hep-lat]`.

[107] R. Arthur et al. "Scattering lengths in SU(2) gauge theory with two fundamental fermions". In: *PoS* LATTICE2014 (2014), p. 271. DOI: `10.22323/1.214.0271`. arXiv: `1412.4771 [hep-lat]`.

[108] R. Arthur et al. “SU(2) gauge theory with two fundamental flavors: A minimal template for model building”. In: *Phys. Rev. D* 94.9 (2016), p. 094507. DOI: `10.1103/PhysRevD.94.094507`. arXiv: `1602.06559 [hep-lat]`.

[109] R. Arthur et al. “$SU(2)$ Gauge Theory with Two Fundamental Flavours: Scalar and Pseudoscalar Spectrum” (July 2016). arXiv: `1607.06654 [hep-lat]`.

[110] L. Del Debbio, A. Patella, and C. Pica. “Higher representations on the lattice: Numerical simulations. SU(2) with adjoint fermions”. In: *Phys. Rev. D* 81 (2010), p. 094503. DOI: `10.1103/PhysRevD.81.094503`. arXiv: `0805.2058 [hep-lat]`.

[111] G. Catumba et al. “Lattice study of SU(2) gauge theory coupled to four adjoint Higgs fields”. In: *Phys. Rev. Res.* 6.4 (2024), p. 043172. DOI: `10.1103/PhysRevResearch.6.043172`. arXiv: `2407.15422 [hep-lat]`.

[112] V. Drach, T. Janowski, and C. Pica. “Update on SU(2) gauge theory with NF = 2 fundamental flavours”. In: *EPJ Web Conf.* 175 (2018). Ed. by M. Della Morte et al., p. 08020. DOI: `10.1051/epjconf/201817508020`. arXiv: `1710.07218 [hep-lat]`.

[113] V. Drach et al. “The scalar sector of $SU(2)$ gauge theory with $N_F = 2$ fundamental flavours”. In: *PoS* LATTICE2016 (2017), p. 229. DOI: `10.22323/1.256.0229`.

[114] V. Drach et al. “Scattering of Goldstone Bosons and resonance production in a Composite Higgs model on the lattice”. In: *JHEP* 04 (2021), p. 117. DOI: `10.1007/JHEP04(2021)117`. arXiv: `2012.09761 [hep-lat]`.

[115] V. Drach et al. “Singlet channel scattering in a composite Higgs model on the lattice”. In: *Eur. Phys. J. C* 82.1 (2022), p. 47. DOI: `10.1140/epjc/s10052-021-09914-y`. arXiv: `2107.09974 [hep-lat]`.

[116] T. Janowski, V. Drach, and C. Pica. “Rho meson decay width in SU(2) gauge theories with 2 fundamental flavours”. In: *PoS* LATTICE2016 (2016), p. 214. DOI: `10.22323/1.256.0214`. arXiv: `1611.09195 [hep-lat]`.

[117] T. Janowski, V. Drach, and S. Prelovsek. “Resonance Study of SU(2) Model with 2 Fundamental Flavours of Fermions”. In: *PoS* LATTICE2019 (2019), p. 123. DOI: `10.22323/1.363.0123`. arXiv: `1910.13847 [hep-lat]`.

[118] R. Lewis, C. Pica, and F. Sannino. "Light Asymmetric Dark Matter on the Lattice: SU(2) Technicolor with Two Fundamental Flavors". In: *Phys. Rev. D* 85 (2012), p. 014504. DOI: `10.1103/PhysRevD.85.014504`. arXiv: `1109.3513 [hep-ph]`.

[119] C. Gattringer and C. B. Lang. *Quantum chromodynamics on the lattice.* Lect. Notes Phys., 2010, p. 211. DOI: `10.1007/978-3-642-01850-3`.

[120] T. DeGrand and C. DeTar. *Lattice Methods for Quantum Chromodynamics.* WORLD SCIENTIFIC, 2006. DOI: `10.1142/6065`. eprint: `https://www.worldscientific.com/doi/pdf/10.1142/6065`. URL: `https://www.worldscientific.com/doi/abs/10.1142/6065`.

[121] I. Montvay and G. Munster. *Quantum fields on a lattice.* Cambridge Monographs on Mathematical Physics. Cambridge University Press, Mar. 1997. ISBN: 978-0-521-59917-7, 978-0-511-87919-7. DOI: `10.1017/CBO9780511470783`.

[122] N. Metropolis et al. "Equation of state calculations by fast computing machines". In: *J. Chem. Phys.* 21 (1953), pp. 1087–1092. DOI: `10.1063/1.1699114`.

[123] J. Gasser and H. Leutwyler. "Light Quarks at Low Temperatures". In: *Phys. Lett. B* 184 (1987), pp. 83–88. DOI: `10.1016/0370-2693(87)90492-8`.

[124] K. G. Wilson. "Confinement of Quarks". In: *Phys. Rev. D* 10 (1974). Ed. by J. C. Taylor, pp. 2445–2459. DOI: `10.1103/PhysRevD.10.2445`.

[125] S. Duane et al. "Hybrid Monte Carlo". In: *Phys. Lett. B* 195 (1987), pp. 216–222. DOI: `10.1016/0370-2693(87)91197-X`.

[126] *GitHub - sa2c/HiRep: HiRep repository — github.com.* `https://github.com/sa2c/HiRep`. [Online; accessed 30-January-2024.

[127] T. Güver et al. "On the capture of dark matter by neutron stars". In: *JCAP* 05 (2014), p. 013. DOI: `10.1088/1475-7516/2014/05/013`. arXiv: `1201.2400 [hep-ph]`.

[128] E. Giangrandi et al. "The Effects of Self-interacting Bosonic Dark Matter on Neutron Star Properties". In: *Astrophys. J.* 953.1 (2023), p. 115. DOI: `10.3847/1538-4357/ace104`. arXiv: `2209.10905 [astro-ph.HE]`.

[129] E. Giangrandi et al. "Numerical Relativity Simulations of Dark Matter Admixed Binary Neutron Stars" (Apr. 2025). arXiv: `2504.20825 [astro-ph.HE]`.

[130] C. Biesdorf, J. Schaffner-Bielich, and L. Tolos. “Masquerading hybrid stars with dark matter”. In: *Phys. Rev. D* 111.8 (2025), p. 083038. DOI: `10.1103/PhysRevD.111.083038`. arXiv: `2412.05207 [hep-ph]`.

[131] F. Hajkarim, J. Schaffner-Bielich, and L. Tolos. “Thermodynamic consistent description of compact stars of two interacting fluids: the case of neutron stars with Higgs portal dark matter”. In: *JCAP* 08 (2025), p. 070. DOI: `10.1088/1475-7516/2025/08/070`. arXiv: `2412.04585 [hep-ph]`.

[132] S. Kunkel, S. Wystub, and J. Schaffner-Bielich. “Determining the minimal mass of a proto-neutron star with chirally constrained nuclear equations of state”. In: *Phys. Rev. C* 111.3 (2025), p. 035807. DOI: `10.1103/PhysRevC.111.035807`. arXiv: `2411.14930 [nucl-th]`.

[133] S. Wystub et al. “Constraining exotic compact stars composed of bosonic and fermionic dark matter with gravitational wave events”. In: *Mon. Not. Roy. Astron. Soc.* 521.1 (2023), pp. 1393–1398. DOI: `10.1093/mnras/stad633`. arXiv: `2110.12972 [astro-ph.HE]`.

[134] S. L. Pitz and J. Schaffner-Bielich. “Generating ultracompact neutron stars with bosonic dark matter”. In: *Phys. Rev. D* 111.4 (2025), p. 043050. DOI: `10.1103/PhysRevD.111.043050`. arXiv: `2408.13157 [astro-ph.HE]`.

[135] R. F. Diedrichs et al. “Tidal deformability of fermion-boson stars: Neutron stars admixed with ultralight dark matter”. In: *Phys. Rev. D* 108.6 (2023), p. 064009. DOI: `10.1103/PhysRevD.108.064009`. arXiv: `2303.04089 [gr-qc]`.

[136] Y. Dengler, A. Maas, and F. Zierler. “Scattering of dark pions in an Sp(4)-gauge theory”. In: *PoS* LATTICE2023 (2024), p. 103. DOI: `10.22323/1.453.0103`. arXiv: `2311.18549 [hep-lat]`.

[137] L. Tolos, J. Schaffner-Bielich, and Y. Dengler. “Dark Compact Planets”. In: *Phys. Rev. D* 92 (2015). [Erratum: Phys.Rev.D 103, 109901 (2021)], p. 123002. DOI: `10.1103/PhysRevD.92.123002`. arXiv: `1507.08197 [astro-ph.HE]`.

[138] P. Mukhopadhyay and J. Schaffner-Bielich. “Quark stars admixed with dark matter”. In: *Phys. Rev. D* 93.8 (2016), p. 083009. DOI: `10.1103/PhysRevD.93.083009`. arXiv: `1511.00238 [astro-ph.HE]`.

[139] Z. Rezaei. “Study of Dark-Matter Admixed Neutron Stars using the Equation of State from the Rotational Curves of Galaxies”. In: *Astrophys. J.* 835.1 (2017), p. 33. DOI: `10.1088/1361-6528/aa5273`. arXiv: `1612.02804 [astro-ph.HE]`.

[140] G. Panotopoulos and I. Lopes. "Dark matter effect on realistic equation of state in neutron stars". In: *Phys. Rev. D* 96.8 (2017), p. 083004. DOI: `10.1103/PhysRevD.96.083004`. arXiv: `1709.06312 [hep-ph]`.

[141] A. Nelson, S. Reddy, and D. Zhou. "Dark halos around neutron stars and gravitational waves". In: *JCAP* 07 (2019), p. 012. DOI: `10.1088/1475-7516/2019/07/012`. arXiv: `1803.03266 [hep-ph]`.

[142] J. Ellis et al. "Search for Dark Matter Effects on Gravitational Signals from Neutron Star Mergers". In: *Phys. Lett. B* 781 (2018), pp. 607–610. DOI: `10.1016/j.physletb.2018.04.048`. arXiv: `1710.05540 [astro-ph.CO]`.

[143] J. Ellis et al. "Dark Matter Effects On Neutron Star Properties". In: *Phys. Rev. D* 97.12 (2018), p. 123007. DOI: `10.1103/PhysRevD.97.123007`. arXiv: `1804.01418 [astro-ph.CO]`.

[144] M. I. Gresham and K. M. Zurek. "Asymmetric Dark Stars and Neutron Star Stability". In: *Phys. Rev. D* 99.8 (2019), p. 083008. DOI: `10.1103/PhysRevD.99.083008`. arXiv: `1809.08254 [astro-ph.CO]`.

[145] O. Ivanytskyi, V. Sagun, and I. Lopes. "Neutron stars: New constraints on asymmetric dark matter". In: *Phys. Rev. D* 102.6 (2020), p. 063028. DOI: `10.1103/PhysRevD.102.063028`. arXiv: `1910.09925 [astro-ph.HE]`.

[146] D. R. Karkevandi et al. "Bosonic dark matter in neutron stars and its effect on gravitational wave signal". In: *Phys. Rev. D* 105.2 (2022), p. 023001. DOI: `10.1103/PhysRevD.105.023001`. arXiv: `2109.03801 [astro-ph.HE]`.

[147] D. R. Karkevandi et al. "Exploring the Distribution and Impact of Bosonic Dark Matter in Neutron Stars". In: *Particles* 7.1 (2024), pp. 201–213. DOI: `10.3390/particles7010011`. arXiv: `2402.18696 [astro-ph.HE]`.

[148] D. Sen and A. Guha. "Implications of feebly interacting dark sector on neutron star properties and constraints from GW170817". In: *Mon. Not. Roy. Astron. Soc.* 504.3 (2021), pp. 3354–3363. DOI: `10.1093/mnras/stab1056`. arXiv: `2104.06141 [hep-ph]`.

[149] A. Guha and D. Sen. "Feeble DM-SM interaction via new scalar and vector mediators in rotating neutron stars". In: *JCAP* 09 (2021), p. 027. DOI: `10.1088/1475-7516/2021/09/027`. arXiv: `2106.10353 [hep-ph]`.

[150] I. Goldman et al. "Possible Implications of Asymmetric Fermionic Dark Matter for Neutron Stars". In: *Phys. Lett. B* 725 (2013), pp. 200–207. DOI: `10.1016/j.physletb.2013.07.017`. arXiv: `1305.6908 [astro-ph.CO]`.

[151] Q.-F. Xiang et al. "Effects of fermionic dark matter on properties of neutron stars". In: *Phys. Rev. C* 89.2 (2014), p. 025803. DOI: `10.1103/PhysRevC.89.025803`. arXiv: `1305.7354 [astro-ph.SR]`.

[152] A. Li, F. Huang, and R.-X. Xu. "Too massive neutron stars: The role of dark matter?" In: *Astropart. Phys.* 37 (2012), pp. 70–74. DOI: `10.1016/j.astropartphys.2012.07.006`. arXiv: `1208.3722 [astro-ph.SR]`.

[153] F. Sandin and P. Ciarcelluti. "Effects of mirror dark matter on neutron stars". In: *Astropart. Phys.* 32 (2009), pp. 278–284. DOI: `10.1016/j.astropartphys.2009.09.005`. arXiv: `0809.2942 [astro-ph]`.

[154] S. C. Leung, M. C. Chu, and L. M. Lin. "Dark-matter admixed neutron stars". In: *Phys. Rev. D* 84 (2011), p. 107301. DOI: `10.1103/PhysRevD.84.107301`. arXiv: `1111.1787 [astro-ph.CO]`.

[155] S. C. Leung, M. C. Chu, and L. M. Lin. "Equilibrium Structure and Radial Oscillations of Dark Matter Admixed Neutron Stars". In: *Phys. Rev. D* 85 (2012), p. 103528. DOI: `10.1103/PhysRevD.85.103528`. arXiv: `1205.1909 [astro-ph.CO]`.

[156] M. F. Barbat, J. Schaffner-Bielich, and L. Tolos. "Comprehensive study of compact stars with dark matter". In: *Phys. Rev. D* 110.2 (2024), p. 023013. DOI: `10.1103/PhysRevD.110.023013`. arXiv: `2404.12875 [astro-ph.HE]`.

[157] M. Hippert et al. "Mirror neutron stars". In: *Phys. Rev. D* 106.3 (2022), p. 035025. DOI: `10.1103/PhysRevD.106.035025`. arXiv: `2103.01965 [astro-ph.HE]`.

[158] M. Hippert et al. "Dark matter or regular matter in neutron stars? How to tell the difference from the coalescence of compact objects". In: *Phys. Rev. D* 107.11 (2023), p. 115028. DOI: `10.1103/PhysRevD.107.115028`. arXiv: `2211.08590 [astro-ph.HE]`.

[159] A. Issifu et al. "Supernova remnants with mirror dark matter and hyperons". In: *Phys. Rev. D* 111.8 (2025), p. 083026. DOI: `10.1103/PhysRevD.111.083026`. arXiv: `2412.17946 [hep-ph]`.

[160] S. Shakeri and D. R. Karkevandi. "Bosonic dark matter in light of the NICER precise mass-radius measurements". In: *Phys. Rev. D* 109.4 (2024), p. 043029. DOI: `10.1103/PhysRevD.109.043029`. arXiv: `2210.17308 [astro-ph.HE]`.

[161] Y. Ema et al. “Dark matter catalyzed baryon destruction”. In: *Phys. Rev. D* 111.2 (2025), p. 023005. DOI: `10.1103/PhysRevD.111.023005`. arXiv: `2405.18472 [hep-ph]`.

[162] K. Gendreau et al. “NICER: The Neutron Star Interior Composition Explorer”. In: *Handbook of X-ray and Gamma-ray Astrophysics*. Ed. by C. Bambi and A. Santangelo. Singapore: Springer Nature Singapore, 2024, pp. 1321–1341. ISBN: 978-981-19-6960-7. DOI: `10.1007/978-981-19-6960-7\_152`. URL: `https://doi.org/10.1007/978-981-19-6960-7%5C_152`.

[163] S. Shirke et al. “Effects of dark matter on f-mode oscillations of neutron stars”. In: *Phys. Rev. D* 110.6 (2024), p. 063025. DOI: `10.1103/PhysRevD.110.063025`. arXiv: `2403.18740 [gr-qc]`.

[164] Y. Dengler et al. “Strongly Interacting Dark Matter admixed Neutron Stars” (Mar. 2025). arXiv: `2503.19691 [hep-ph]`.

[165] B. P. Abbott et al. (LIGO Scientific, Virgo). “GW170817: Observation of Gravitational Waves from a Binary Neutron Star Inspiral”. In: *Phys. Rev. Lett.* 119.16 (2017), p. 161101. DOI: `10.1103/PhysRevLett.119.161101`. arXiv: `1710.05832 [gr-qc]`.

[166] B. P. Abbott et al. (LIGO Scientific, Virgo). “GW190425: Observation of a Compact Binary Coalescence with Total Mass $\sim 3.4 M_\odot$”. In: *Astrophys. J. Lett.* 892.1 (2020), p. L3. DOI: `10.3847/2041-8213/ab75f5`. arXiv: `2001.01761 [astro-ph.HE]`.

[167] R. Abbott et al. (LIGO Scientific, KAGRA, VIRGO). “Observation of Gravitational Waves from Two Neutron StarBlack Hole Coalescences”. In: *Astrophys. J. Lett.* 915.1 (2021), p. L5. DOI: `10.3847/2041-8213/ac082e`. arXiv: `2106.15163 [astro-ph.HE]`.

[168] M. Colpi et al. (LISA). “LISA Definition Study Report” (Feb. 2024). arXiv: `2402.07571 [astro-ph.CO]`.

[169] A. Abac et al. “The Science of the Einstein Telescope” (Mar. 2025). arXiv: `2503.12263 [gr-qc]`.

[170] K. Holland et al. “Exceptional confinement in G(2) gauge theory”. In: *Nucl. Phys.* B668 (2003), pp. 207–236. DOI: `10.1016/S0550-3213(03)00571-6`. arXiv: `hep-lat/0302023`.

[171] M. Pepe and U. .-. Wiese. “Exceptional Deconfinement in G(2) Gauge Theory”. In: *Nucl. Phys. B* 768 (2007), pp. 21–37. DOI: `10.1016/j.nuclphysb.2006.12.024`. arXiv: `hep-lat/0610076`.

[172] O. Hajizadeh and A. Maas. "Constructing a neutron star from the lattice in G_2-QCD". In: *Eur. Phys. J. A* 53.10 (2017), p. 207. DOI: `10.1140/epja/i2017-12398-x`. arXiv: `1702.08724 [astro-ph.HE]`.

[173] A. Kurkela et al. "Constraining neutron star matter with Quantum Chromodynamics". In: *Astrophys. J.* 789 (2014), p. 127. DOI: `10.1088/0004-637X/789/2/127`. arXiv: `1402.6618 [astro-ph.HE]`.

[174] K. Hebeler et al. "EQUATION OF STATE AND NEUTRON STAR PROPERTIES CONSTRAINED BY NUCLEAR PHYSICS AND OBSERVATION". In: *The Astrophysical Journal* 773.1 (July 2013), p. 11. DOI: `10.1088/0004-637X/773/1/11`. URL: `https://dx.doi.org/10.1088/0004-637X/773/1/11`.

[175] A. Kurkela, P. Romatschke, and A. Vuorinen. "Cold Quark Matter". In: *Phys. Rev. D* 81 (2010), p. 105021. DOI: `10.1103/PhysRevD.81.105021`. arXiv: `0912.1856 [hep-ph]`.

[176] B. Kain. "Dark matter admixed neutron stars". In: *Phys. Rev. D* 103.4 (2021), p. 043009. DOI: `10.1103/PhysRevD.103.043009`. arXiv: `2102.08257 [gr-qc]`.

[177] S. Valdez-Alvarado et al. "Dynamical evolution of fermion-boson stars". In: *Phys. Rev. D* 87.8 (2013), p. 084040. DOI: `10.1103/PhysRevD.87.084040`. arXiv: `1210.2299 [gr-qc]`.

[178] J. S. Read et al. "Constraints on a phenomenologically parameterized neutron-star equation of state". In: *Phys. Rev. D* 79 (2009), p. 124032. DOI: `10.1103/PhysRevD.79.124032`. arXiv: `0812.2163 [astro-ph]`.

[179] G. Narain, J. Schaffner-Bielich, and I. N. Mishustin. "Compact stars made of fermionic dark matter". In: *Phys. Rev. D* 74 (2006), p. 063003. DOI: `10.1103/PhysRevD.74.063003`. arXiv: `astro-ph/0605724`.

[180] I. Sagert et al. "Compact stars for undergraduates". In: *Eur. J. Phys.* 27 (2006), pp. 577–610. DOI: `10.1088/0143-0807/27/3/012`. arXiv: `astro-ph/0506417`.

[181] T. Hinderer et al. "Tidal deformability of neutron stars with realistic equations of state and their gravitational wave signatures in binary inspiral". In: *Phys. Rev. D* 81 (2010), p. 123016. DOI: `10.1103/PhysRevD.81.123016`. arXiv: `0911.3535 [astro-ph.HE]`.

[182] T. Hinderer. “Tidal Love numbers of neutron stars”. In: *Astrophys. J.* 677 (2008). [Erratum: Astrophys.J. 697, 964 (2009)], pp. 1216–1220. DOI: `10.1086/533487`. arXiv: `0711.2420 [astro-ph]`.

[183] S. Postnikov, M. Prakash, and J. M. Lattimer. “Tidal Love Numbers of Neutron and Self-Bound Quark Stars”. In: *Phys. Rev. D* 82 (2010), p. 024016. DOI: `10.1103/PhysRevD.82.024016`. arXiv: `1004.5098 [astro-ph.SR]`.

[184] B. P. Abbott et al. (LIGO Scientific Collaboration and Virgo Collaboration). “GW170817: Observation of Gravitational Waves from a Binary Neutron Star Inspiral”. In: *Phys. Rev. Lett.* 119 (16 Oct. 2017), p. 161101. DOI: `10.1103/PhysRevLett.119.161101`. URL: `https://link.aps.org/doi/10.1103/PhysRevLett.119.161101`.

[185] V. Cardoso, E. Franzin, and P. Pani. “Is the gravitational-wave ringdown a probe of the event horizon?” In: *Phys. Rev. Lett.* 116.17 (2016). [Erratum: Phys.Rev.Lett. 117, 089902 (2016)], p. 171101. DOI: `10.1103/PhysRevLett.116.171101`. arXiv: `1602.07309 [gr-qc]`.

[186] V. Cardoso and P. Pani. “Tests for the existence of black holes through gravitational wave echoes”. In: *Nature Astron.* 1.9 (2017), pp. 586–591. DOI: `10.1038/s41550-017-0225-y`. arXiv: `1709.01525 [gr-qc]`.

[187] F. Di Giovanni et al. “Impact of ultralight bosonic dark matter on the dynamical bar-mode instability of rotating neutron stars”. In: *Phys. Rev. D* 106.4 (2022), p. 044008. DOI: `10.1103/PhysRevD.106.044008`. arXiv: `2206.00977 [gr-qc]`.

[188] A. Bauswein et al. “Compact dark objects in neutron star mergers”. In: *Phys. Rev. D* 107.8 (2023), p. 083002. DOI: `10.1103/PhysRevD.107.083002`. arXiv: `2012.11908 [astro-ph.HE]`.

[189] V. Doroshenko et al. “A strangely light neutron star within a supernova remnant”. In: *Nature Astron.* 6.12 (2022), pp. 1444–1451. DOI: `10.1038/s41550-022-01800-1`.

[190] T. Salmi et al. “The Radius of the High-mass Pulsar PSR J0740+6620 with 3.6 yr of NICER Data”. In: *Astrophys. J.* 974.2 (2024), p. 294. DOI: `10.3847/1538-4357/ad5f1f`. arXiv: `2406.14466 [astro-ph.HE]`.

[191] D. Choudhury et al. “A NICER View of the Nearest and Brightest Millisecond Pulsar: PSR J04374715”. In: *Astrophys. J. Lett.* 971.1 (2024), p. L20. DOI: `10.3847/2041-8213/ad5a6f`. arXiv: `2407.06789 [astro-ph.HE]`.

[192] G. F. Burgio et al. "Neutron stars and the nuclear equation of state". In: *Prog. Part. Nucl. Phys.* 120 (2021), p. 103879. DOI: `10.1016/j.ppnp.2021.103879`. arXiv: `2105.03747 [nucl-th]`.

[193] J. Bijnens and J. Lu. "Meson-meson Scattering in QCD-like Theories". In: *JHEP* 03 (2011), p. 028. DOI: `10.1007/JHEP03(2011)028`. arXiv: `1102.0172 [hep-ph]`.

[194] C. Alexandrou et al. "P-wave $\pi\pi$ scattering and the ρ resonance from lattice QCD". In: *Phys. Rev. D* 96.3 (2017), p. 034525. DOI: `10.1103/PhysRevD.96.034525`. arXiv: `1704.05439 [hep-lat]`.

[195] M. T. Hansen and S. R. Sharpe. "Relativistic, model-independent, three-particle quantization condition". In: *Phys. Rev. D* 90.11 (2014), p. 116003. DOI: `10.1103/PhysRevD.90.116003`. arXiv: `1408.5933 [hep-lat]`.

[196] M. T. Hansen and S. R. Sharpe. "Lattice QCD and Three-particle Decays of Resonances". In: *Ann. Rev. Nucl. Part. Sci.* 69 (2019), pp. 65–107. DOI: `10.1146/annurev-nucl-101918-023723`. arXiv: `1901.00483 [hep-lat]`.

[197] R. A. Briceno, J. J. Dudek, and R. D. Young. "Scattering processes and resonances from lattice QCD". In: *Rev. Mod. Phys.* 90.2 (2018), p. 025001. DOI: `10.1103/RevModPhys.90.025001`. arXiv: `1706.06223 [hep-lat]`.

[198] S. M. Dawid et al. "Two- and three-meson scattering amplitudes with physical quark masses from lattice QCD". In: *Phys. Rev. D* 112.1 (2025), p. 014505. DOI: `10.1103/bx16-lp3r`. arXiv: `2502.17976 [hep-lat]`.

[199] L. von Smekal. "Universal Aspects of QCD-like Theories". In: *Nucl. Phys. B Proc. Suppl.* 228 (2012). Ed. by B. .-. Schaefer, R. Alkofer, and C. S. Fischer, pp. 179–220. DOI: `10.1016/j.nuclphysbps.2012.06.006`. arXiv: `1205.4205 [hep-ph]`.

[200] A. Francis et al. "Dark Matter from Strong Dynamics: The Minimal Theory of Dark Baryons". In: *JHEP* 12 (2018), p. 118. DOI: `10.1007/JHEP12(2018)118`. arXiv: `1809.09117 [hep-ph]`.

[201] P. Cvitanovic. *Group Theory: Birdtracks, Lie's, and Exceptional Groups.* Princeton University Press, May 2020. ISBN: 978-0-691-20298-3.

[202] R. Feger, T. W. Kephart, and R. J. Saskowski. "LieART 2.0 A Mathematica application for Lie Algebras and Representation Theory". In: *Comput. Phys. Commun.* 257 (2020), p. 107490. DOI: `10.1016/j.cpc.2020.107490`. arXiv: `1912.10969 [hep-th]`.

[203] T. Blum et al. (RBC, UKQCD). “Isospin 0 and 2 two-pion scattering at physical pion mass using all-to-all propagators with periodic boundary conditions in lattice QCD”. In: *Phys. Rev. D* 107.9 (2023). [Erratum: Phys.Rev.D 108, 039902 (2023)], p. 094512. DOI: `10.1103/PhysRevD.107.094512`. arXiv: `2301.09286 [hep-lat]`.

[204] P. Lepage. *gplepage/corrfitter: corrfitter version 8.2*. Version v8.2. Nov. 2021. DOI: `10.5281/zenodo.5733391`. URL: `https://doi.org/10.5281/zenodo.5733391`.

[205] S. Prelovsek and D. Mohler. “A Lattice study of light scalar tetraquarks”. In: *Phys. Rev. D* 79 (2009), p. 014503. DOI: `10.1103/PhysRevD.79.014503`. arXiv: `0810.1759 [hep-lat]`.

[206] G. Martinelli and Y.-C. Zhang. “The Connection Between Local Operators on the Lattice and in the Continuum and Its Relation to Meson Decay Constants”. In: *Phys. Lett. B* 123 (1983), p. 433. DOI: `10.1016/0370-2693(83)90987-5`.

[207] J. Foley et al. “Practical all-to-all propagators for lattice QCD”. In: *Comput. Phys. Commun.* 172 (2005), pp. 145–162. DOI: `10.1016/j.cpc.2005.06.008`. arXiv: `hep-lat/0505023`.

[208] S. Aoki et al. (CS). “ρ Meson Decay in 2+1 Flavor Lattice QCD”. In: *Phys. Rev. D* 84 (2011), p. 094505. DOI: `10.1103/PhysRevD.84.094505`. arXiv: `1106.5365 [hep-lat]`.

[209] M. Gockeler et al. “Scattering phases for meson and baryon resonances on general moving-frame lattices”. In: *Phys. Rev. D* 86 (2012), p. 094513. DOI: `10.1103/PhysRevD.86.094513`. arXiv: `1206.4141 [hep-lat]`.

[210] K. Rummukainen and S. A. Gottlieb. “Resonance scattering phase shifts on a nonrest frame lattice”. In: *Nucl. Phys. B* 450 (1995), pp. 397–436. DOI: `10.1016/0550-3213(95)00313-H`. arXiv: `hep-lat/9503028`.

[211] J. J. Dudek, R. G. Edwards, and C. E. Thomas (Hadron Spectrum). “Energy dependence of the ρ resonance in $\pi\pi$ elastic scattering from lattice QCD”. In: *Phys. Rev. D* 87.3 (2013). [Erratum: Phys.Rev.D 90, 099902 (2014)], p. 034505. DOI: `10.1103/PhysRevD.87.034505`. arXiv: `1212.0830 [hep-ph]`.

[212] P. Estabrooks and A. D. Martin. “pi pi Partial Waves from 0.6-GeV to 1.8-GeV”. In: *Nucl. Phys. B* 95 (1975), pp. 322–346. DOI: `10.1016/0550-3213(75)90048-6`.

[213] M. S. Dresselhaus, G. Dresselhaus, and A. Jorio. *Group Theory: Application to the Physics of Condensed Matter*. Springer, 2008. ISBN: 978-3-540-32897-1. DOI: `10.1007/978-3-540-32899-5`.

[214] M. Luscher. “Volume Dependence of the Energy Spectrum in Massive Quantum Field Theories. 1. Stable Particle States”. In: *Commun. Math. Phys.* 104 (1986), p. 177. DOI: `10.1007/BF01211589`.

[215] M. Luscher. “Volume Dependence of the Energy Spectrum in Massive Quantum Field Theories. 2. Scattering States”. In: *Commun. Math. Phys.* 105 (1986), pp. 153–188. DOI: `10.1007/BF01211097`.

[216] M. Luscher. “Two particle states on a torus and their relation to the scattering matrix”. In: *Nucl. Phys. B* 354 (1991), pp. 531–578. DOI: `10.1016/0550-3213(91)90366-6`.

[217] L. Leskovec and S. Prelovsek. “Scattering phase shifts for two particles of different mass and non-zero total momentum in lattice QCD”. In: *Phys. Rev. D* 85 (2012), p. 114507. DOI: `10.1103/PhysRevD.85.114507`. arXiv: `1202.2145 [hep-lat]`.

[218] X. Feng, K. Jansen, and D. B. Renner (ETM). “A new moving frame to extract scattering phases in lattice QCD”. In: *PoS* LATTICE2010 (2010). Ed. by G. Rossi, p. 104. arXiv: `1104.0058 [hep-lat]`.

[219] P. Jenny, A. Maas, and B. Riederer. “Vector boson scattering from the lattice”. In: *Phys. Rev. D* 105.11 (2022), p. 114513. DOI: `10.1103/PhysRevD.105.114513`. arXiv: `2204.02756 [hep-lat]`.

[220] L. Leskovec. “Hadronic resonances from lattice QCD”. PhD thesis. Ljubljana U., 2017.

[221] Y. Dengler, A. Maas, and F. Zierler. “Scattering of dark pions in Sp(4) gauge theory”. In: *Phys. Rev. D* 110.5 (2024), p. 054513. DOI: `10.1103/PhysRevD.110.054513`. arXiv: `2405.06506 [hep-lat]`.

[222] Y. Dengler, A. Maas, and F. Zierler. “Scattering of SIMPlectic Dark Pions”. In: *PoS* LATTICE2024 (2025), p. 087. DOI: `10.22323/1.466.0087`. arXiv: `2501.18368 [hep-lat]`.

[223] E. Bennett et al. “Spectrum of mesons in quenched Sp(2N) gauge theories”. In: *Phys. Rev. D* 109.9 (2024), p. 094517. DOI: `10.1103/PhysRevD.109.094517`. arXiv: `2312.08465 [hep-lat]`.

[224] H. Koleová, D. Krichevskiy, and S. Kulkarni. “NLO observables for QCD-like theories and application to pion dark matter” (Sept. 2025). arXiv: `2509.07102 [hep-ph]`.

[225] E. Bennett et al. “Meson spectroscopy in the Sp(4) gauge theory with three antisymmetric fermions”. In: *Phys. Rev. D* 111.7 (2025), p. 074511. DOI: `10.1103/PhysRevD.111.074511`. arXiv: `2412.01170 [hep-lat]`.

[226] A. Alotaibi, M. T. Hansen, and R. A. Briceño. “Implementing the finite-volume three-pion scattering formalism across all non-maximal isospins” (Aug. 2025). arXiv: `2508.11627 [hep-lat]`.

[227] J. Baeza-Ballesteros et al. “The three-pion K-matrix at NLO in ChPT”. In: *JHEP* 03 (2024), p. 048. DOI: `10.1007/JHEP03(2024)048`. arXiv: `2401.14293 [hep-ph]`.

[228] J.-W. Lee, B. Lucini, and M. Piai. “Symmetry restoration at high-temperature in two-color and two-flavor lattice gauge theories”. In: *JHEP* 04 (2017), p. 036. DOI: `10.1007/JHEP04(2017)036`. arXiv: `1701.03228 [hep-lat]`.